Object-based image analysis of ultra-fine spatial resolution imagery acquired over a saltmarsh environment by an Unmanned Aircraft System (UAS)

by

Joshua Michael Kelcey

BSc (Hons)

School of Land and Food

Submitted in fulfilment of the requirements for the Degree of Doctor of Philosophy

University of Tasmania

May, 2014

This thesis contains no material which has been accepted for a degree or diploma by the University or any other institution, except by way of background information and duly acknowledged in the thesis, and to the best of my knowledge and belief no material previously published or written by another person except where due acknowledgement is made in the text of the thesis, nor does the thesis contain any material that infringes copyright.

Joshua Kelcey

15 May 2014

Statement of Co-Authorship

The following people and institutions contributed to the publication of the work undertaken as part of this thesis:

Joshua Kelcey, School of Land and Food, University of Tasmania

Arko Lucieer, School of Land and Food, University of Tasmania

Author details and their roles:

Chapter 2: Kelcey (95%), Lucieer (5%)

All authors contributed to the idea and its development; Kelcey performed all data processing, analysis, and writing; Lucieer contributed editorial advice.

Chapter 3: Kelcey (95%), Lucieer (5%)

All authors contributed to the idea and its development; Kelcey performed all data processing, analysis, and writing; Lucieer contributed editorial advice.

Chapter 4: Kelcey (95%), Lucieer (5%)

All authors contributed to the idea and its development; Kelcey performed all data processing, analysis, and writing; Lucieer contributed editorial advice.

Chapter 5: Kelcey (95%), Lucieer (5%)

All authors contributed to the idea and its development; Kelcey performed all data processing, analysis, and writing; Lucieer contributed editorial advice.

We the undersigned agree with the above stated "proportion of work undertake" for each of the above manuscripts contributing to this thesis:

Candidate: **Joshua Kelcey** (15 May 2014)

Arko Lucieer (15 May 2014)

Abstract

Unmanned Aircraft Systems (UAS) are an emerging technology in the field of remote sensing. Two fundamental differences of UAS when compared with traditional aerial remote sensing platforms are the operational altitude and payload capacity. The lower operational altitude of UAS generates ultra-fine spatial resolution data (¡ 10 cm). The small size of most UAS platforms allows scientific research groups to transport and operate the platform within small focused study areas. However, a small size also places physical limitations on UAS sensor payload carrying capacity. This requires a compromise between sensor functionality, cost, and weight. Sensor feature reduction or miniaturisation achieves this compromise but at the cost of data quality. This thesis advances UAS remote sensing through an exploration of the development, scale analysis and application of ultra-fine spatial resolution UAS data.

Two sites of remnant cold temperate saltmarsh vegetation in Tasmania were selected to assess UAS remote sensing. Frequent salt water spray and tidal inundation within saltmarsh create a saline gradient that limits the establishment of larger canopy species. This has resulted in the dominance of salt and water-logging tolerant herbaceous and small woody shrub species. Despite the harsh environmental conditions, the combination of land wash-off and tidal inundation both readily supply and redistribute nutrients, creating one of the most environmentally productive environments. Measuring the fine-scale vegetation distribution and productivity of cold temperate saltmarsh vegetation requires the ultra-fine spatial resolution data of UAS.

In this study, a sensor correction methodology was designed and implemented to reduce the effects of noise and distortion in the 6-band multispectral miniature multiple camera array (mini-MCA) produced by Tetracam. This methodology includes techniques for sensor noise reduction using dark offset subtraction, vignetting correction through flat field look-up tables, and lens distortion correction by implementing the Brown-Conrady

model. The sensor correction framework is demonstrated through a real-world application on UAS-derived saltmarsh data. Chapter 2 demonstrates that sensor noise and distortions can be satisfactorily corrected in 6-band Tetracam mini-MCA data acquired from a small multirotor UAS.

Once image data are constructed, the next challenge lies in deconstructing the complex ultra-fine spatial resolution UAS data to derive meaningful information. The increased resolving power of UAS data provides spatial measurements of image features at scales previously too small to distinguish. This results in increased spatial complexity as fine-scale structural variation becomes measurable. A key challenge is to disassemble and simplify this fine-scale variation for the extraction of information. This is achieved through two frameworks that provide a meaningful spatial generalisation using image texture models and geospatial object-based image analysis (GEOBIA).

Image texture is defined as the replications, symmetries and patterns in tonal structure. Image texture models are used to quantify the tonal structure in a local neighbourhood into a single, statistical measure. The large number of available texture models and parameters, as well as the dependence of texture on image scale and context, complicates the optimal selection of image texture measures. In Chapter 3, a texture selection methodology is introduced to provide a rapid, broad assessment of image texture.

The texture selection framework is illustrated using a 6-band multispectral dataset of a saltmarsh site. Four texture models are investigated: a simple first-order kernel, the grey-level co-occurrence matrix (GLCM), local binary pattern operator (LBP), and wavelets. Using image subsets, 693 texture measures are extracted from seven vegetation and non-vegetation groundcover classes. A random forest ensemble classifier was used to quantify the relative class-specific importance of individual texture measures. A correlation threshold was used to remove highly correlated, less important measures before forward inclusion was used to identify the minimum optimal number of texture measures. The number of required texture measures was linked with class spectral variation, with spectrally com-

plicated classes requiring more measures. The performance of the measures was tested across the entire image, with a recorded improvement of 17.2% in overall classification accuracy with the inclusion of selected texture measures.

GEOBIA extends traditional pixel-based analysis through the segmentation of imagery into meaningful objects. The results of the initial segmentation determine the units of analysis, and their accuracy is therefore paramount to the entire analysis. As with texture, image segmentation is dependent upon image structure and content. In Chapter 4, a methodology is presented utilising image subsets to identify class-specific relative scales of image segmentation through identifying under- and over-segmentation. Reference objects were used to compare image segmentation results against a meaningful real-world abstraction. Under-segmentation was tested using spatial area metrics, and was quantified on a class-by-class basis whenever a subset recorded 100% omission in labelling. Over-segmentation was identified by extracting the statistical properties of objects and then testing the separability using a random forest model. The insufficient spatial generalisation of over-segmentation resulted in reduced class separability. Furthermore, spatial accuracy was limited by classification accuracy, as the need of spatial generalisation to achieve class separability required suitably large objects. It was found that this dependence upon objects for spatial generalisation could be reduced through the incorporation of texture measures.

Chapter 5 explores the scale potential of ultra-fine spatial resolution data. Field-level biomass modelling relies upon the construction of allometric models for the rapid estimation of biomass based upon easily measurable plant characteristics. Allometric modelling is regarded as the most accurate approach for estimating plant biomass, but its extension to remotely sensed data has been limited by data resolution. Coarser data resolution may limit or exclude the ability to measure the parameters required of plant allometric biomass models. The potential of ultra-fine resolution UAS data to measure allometric parameters is presented in Chapter 5, which is focused on fine-scale shrub biomass. Field-

derived allometric relationships are used to deconstruct shrub structure through image segmentation. Allometric parameters derived from the shrub components are then used to estimate biomass.

This thesis demonstrates a methodology to develop and analyse UAS remotely sensed data, illustrating the scale potential of ultra-fine spatial resolution data. The increased complexity of fine-scale variability is a recognised problem associated with the improved resolving power of image data. This variability is a central challenge for UAS remote sensing and the analysis of the ultra-fine data scale it generates. By developing a clear methodology to construct and meaningfully disassemble ultra-fine resolution UAS data, this thesis provides a foundation which provides broader access to the novel scale niche that UAS measurements fill.

Acknowledgements

Firstly I would like to thank Arko Lucieer for his indispensable supervision of this study, guidance in all of its aspects, assistance in field work, and support both within and outside of my Ph.D. I would like to thank Chris Watson for his support. I would also like to acknowledge the Winifred Violet Scott Trust for funding support.

I would like to thank my mother Helena for the tireless support, encouragement and love over my lifetime, without which I'd have never been able to achieve the things I have. Thank you to Janeil for her guidance, support and good humour. Thank you to Penny and Pippin for sitting with me through the long hours. Thanks also to my other family members, friends and colleagues.

Above all, I'd like to thank my wife Kelli. Thank you for your support and love through the ups and downs of this Ph.D. I feel so privileged to have you as both a best-friend and a partner, and I look forwards to seeing where life takes us next! Honey I'm home!

TABLE OF CONTENTS

LIST OF TABLES

LIST OF FIGURES

Chapter 1

Introduction

1.1 Background

1.1.1 Saltmarsh

Saltmarshes have become threatened on a global scale as human activity continues to remove, degrade and fragment these vegetation communities (Laegdsgaard, 2006). Saltmarsh communities develop within sheltered stretches of riparian or coastal areas (Adam, 2002). Within these sheltered areas, the absence of high energy waves allows the accumulation of sediments and organic nutrients (Temmerman et al., 2004). Terrestrial runoff and a periodic tidal inundation create an environment with a regular influx and redistribution of nutrients (Levine et al., 1998; Emery et al., 2001). These dynamics, when combined with rich organic soil, generates an environment recognised as among the most productive ecosystems in the world.

Saltmarsh environments favour vegetation with water logging resistance or saline tolerance adaptations (Emery et al., 2001). Communities are dominated by herbaceous species, predominately rushes, sedges and grasses. The establishment of large woody canopy species is limited by the harsh environmental conditions, including frequent tidal disturbance. Tidal inundation, salt spray, local topography and drainage result in strong water and

saline gradients (Pennings and Callaway, 1992). These gradients strongly drive species distribution, with niches commonly exhibiting strong species-level zonation (Emery et al., 2001; Bertness, 1991; Bertness and Shumway, 1993).

Saltmarshes have historically been viewed as a risk to public health, with the stagnant, rotting organic conditions incorrectly assessed as a potential source of disease. Given the richly developed soils, the destruction of saltmarsh ecosystems was encouraged through "reclamation" efforts that transformed the environment into agricultural, industrial or residential land (Adam, 2002). A growing awareness of environmental and ecological values, however, have shifted this historical perception of saltmarsh communities. Saltmarsh provides a buffer between terrestrial and aquatic environments. It protects vulnerable upshore environments from scouring storm surges and erosion, while simultaneously protecting aquatic environments by filtering terrestrial runoff (Goetz, 2006). Furthermore, saltmarsh is an important refuge for migratory and endangered species (Laegdsgaard, 2006).

In light of its historical destruction and growing ecological understanding, efforts are being made to conserve and rehabilitate saltmarsh communities (Adam, 2002; Laegdsgaard, 2006). Mapping provides information on the spatial distribution of vegetation, detection of on-going changes within communities, and monitoring the effects of implemented management programs (Goetz, 2006). Field-based mapping programs represent a significant, on-going investment of time and resources. Remote sensing has significant potential as an alternative method to field-based monitoring.

1.1.2 Remote Sensing

Remote sensing is a science of observation and is used to measure spatio-temporal relationships between objects without physical contact. Sensors fitted to satellite or aircraft platforms can generate consistent measurements across large spatial extents. Measurements can be adapted for vegetation monitoring purposes to estimate species composition,

plant health and spatial distributions (Sims and Gamon, 2002; Asner, 1998). Generating spatial information using a remote sensing platform requires a compromise between four characteristics of data resolution: spatial, extent, spectral and temporal. Spatial resolution is the minimum size of an observation and is defined as the spatial coverage of a single pixel. Data extent is defined by the collective span of all pixels. The spectral resolution is the capacity of a sensor to measure discrete wavelength ranges of the electromagnetic spectrum. Temporal resolution is the rate a platform can revisit a site. The application of remote sensing for saltmarsh monitoring has been limited by the scale of remote sensing data.

1.1.3 Scale

Dungan et al. (2002) identifies three categories of scale relevant to remote sensing studies: phenomena, sampling and analysis scales. Phenomena scale relates to the spatial structure or processes under observation (Dungan et al., 2002). Saltmarsh communities exhibit a phenomena scale defined by spatial fragmentation and driven by small changes in local topography (Laegdsgaard, 2006). Conversely, the sampling scale of spatial data are defined by image extent and grain (Marceau and Hay, 1999). The grain defines the spatial extents of a single observation. Within imagery, grain is defined by the spatial resolution of the pixel. Extent defines the span of all observations, and for a single image is defined by the sensor's instantaneous field of view. The operational altitude of a remote sensing platform has the largest influence on image grain and extent, with higher altitudes increasing extent in favour of grain. The sampling scale of traditional remote sensing platforms relative to the phenomena scale of saltmarsh vegetation is coarse. Coarse sampling scales may over-generalise individual observations, thereby unable to represent the structure of fine scale phenomena. This places limitations upon the third category of scale, analysis.

The scale of analysis is used to summarise or draw inferences about a phenomena using

sampling (Dungan et al., 2002). The fine phenomena-scale of saltmarsh structure and distribution is lost with the spatial generalisation of over-coarse sampling. This has forced remote sensing of saltmarsh to broader scales of analysis.

When utilising Landsat data to estimate saltmarsh biomass, Zhang and Ustin (1997) forgo the measuring of individual species in favour of correlating broader saltmarsh biomass estimates with spectral indices. Phinn et al. (1999) utilised fine resolution data (75 cm) to ensure the spatial discrimination of large saltmarsh canopy species. This canopy species was then used as an indicator to monitor restoration efforts for the community. Silvestri et al. (2003) estimates saltmarsh species composition by utilising a linear-mixture model to estimate sub-pixel species contributions. Within each of these three studies, the coarse scale of sampling relative to phenomena has limited spatial resolving of fine-scale saltmarsh community structure. This has resulted in a reliance upon indirect landscape metrics and environmental indicators for saltmarsh monitoring (Klemas, 2001). However, saltmarsh communities are often spatially fragmented and are dominated by small herbaceous species. In addition, frequent tidal disturbance can result in rapid fine-scale changes in plant distribution (Laegdsgaard, 2006). On-going saltmarsh monitoring requires a remote sensing platform capable of both generating ultra-fine resolution sample data to map the fine-scale spatial distribution of species, and high temporal resolution sample data to measure rapid fine-scale changes in the environment. Unmanned aerial systems (UAS) have the capacity to generate spatial data at a sample scale suitable for the direct monitoring of saltmarsh communities.

1.1.4 Unmanned Aerial Systems (UAS)

UAS are small remotely piloted fixed wing or rotary-powered aircraft that can be utilised as a remote sensing platform. The use of UAS within Australia falls under legislation on remotely piloted aircraft systems, which is governed by the Civil Aviation Safety Author-

ity (CASA)[1]. Without strict CASA approval, UAS flown in Australia are restricted to line-of-sight from the remote pilot and an altitude beneath 400 ft. The low flying altitude of UAS generates data observations at an ultra-fine spatial resolution (<10 cm) (Dunford et al., 2009). The small size of the UAS allows for easy portability and fast deployment. This creates a strong flight-on-demand capability and potentially high temporal rates of data collection. However, its small size also limits power and flight times (around 10 minutes for a typical multirotor UAS), which significantly reduces the overall spatial extent of data collection.

The UAS is highly suited for generating the fine scale measurements required by precision vegetation monitoring. Laliberte et al. (2007) demonstrated that a fixed-wing UAS can be successfully employed for the classification and terrain modelling of rangeland vegetation communities. A rotor-wing LiDAR UAS was used byWallace et al. (2012) for the generation of high density point clouds of forest inventory assessment. Lucieer et al. (2014) utilised a UAS for precision monitoring of Antarctic moss beds, linking fine-scale rock topography to plant health through its influence on water availability.

1.1.5 Ultra-Fine Resolution Data

The rise of UAS platforms brings new challenges in the analysis of information within ultra-fine resolution data. Strahler et al. (1986) distinguishes the relationship between phenomena and sample scale into two groups by : low resolution relationships (L-res) and fine resolution relationships (H-res). A coarse sample scale can over-generalise phenomena, thereby limiting small scale measurements (Woodcock and Strahler, 1987), resulting in a L-res relationship. Conversely, a fine sample scale may overcomplicate phenomena by introducing excessive small-scale variation (Maillard, 2003; Blaschke, 2010), resulting in a H-res relationship. The increase in spatial complexity of ultra-fine resolution data, and its subsequent analysis, are one of the fundamental problems associated with UAS

[1]http://www.casa.gov.au/

data. The analysis of UAS data requires spatial generalisation. Spatial generalisation shifts the sample scale through a meaningful reduction of this spatial complexity to an optimal analysis scale. The degree of spatial generalisation required is dependent upon the scale of both the image and the features under observation. Two approaches to spatial generalisation are the use of image texture models and geographic object-based image analysis (GEOBIA).

Texture models spatially generalise by calculating a statistical metric within a local neighbourhood. Texture metrics quantify the replications, symmetries and patterns within image tonal structure (Woodcock and Strahler, 1987). A texture model operates using the local neighbourhood centred around a pixel. The variation within this neighbourhood is reduced to a single texture metric, which is applied to the central pixel. Iteratively moving the neighbourhood across the image generates a separate texture layer. Modifying the size of the neighbourhood allows texture models to explore different scales of analysis (Puissant et al., 2005).

GEOBIA shifts observations from individual pixels to image objects (Blaschke, 2010; Powers et al., 2012). GEOBIA operates by segmenting imagery into smaller objects. An image object is constructed by grouping neighbouring pixels together based upon a statistical measure of similarity (Stuckens et al., 2000). Metrics are then derived from the contained pixels and the geometry of the object. A threshold determines the measure of similarity, and thereby controls image object size and the overall degree of spatial generalisation.

1.2 Problem Statement

Remote sensing provides an ideal tool for on-going vegetation monitoring programs. Platform characteristics determine the spatial scale of sampled data. Traditional aerial or satellite approaches have excluded fine-scale sampling (<10 cm), limiting remote sensing to broader monitoring scales. The monitoring of fine-scale phenomena changes within small, vulnerable communities requires a platform capable of acquiring data at a matching sample scale. The advent of low-cost UAS introduces a new paradigm in platform accessibility and data sampling scale.

Low-cost UAS (<\$10,000[2]) enable small research groups to develop a niche remote sensing platform. The accessibility of UAS is dependent upon robust frameworks for constructing and analysing UAS data. Relative to larger, more expensive platforms, the UAS is limited in its payload and power capacity, and therefore requires significant sensor miniaturisation. Sensor miniaturisation is achieved by the removal of space consuming circuitry for onboard data processing and decreasing the size of sensor elements. This decrease in size of sensor elements results in an increase sensitivity to sensor noise. This miniaturisation impacts on data quality, with collected data requiring robust preprocessing and corrections prior to analysis.

Analysis of ultra-fine spatial resolution UAS data may require meaningful spatial generalisation to achieve an appropriate scale for analysis. Texture models and GEOBIA techniques for spatial generalisation are well established. The sample scale may be shifted through the local neighbourhood of a texture model or the similarity threshold of a GEOBIA segmentation. While the scale of a single data source is fixed, variation between data collection regimes creates variation in scale between data sources. An optimal texture local neighbourhood or similarity threshold is relative to the fixed scale, and is therefore not transferable between different data sources. **The fundamental problem that this**

[2]http://www.mikrokopter.de/en/home

thesis aims to address is how to identify the optimal analysis scale and how to identify the optimal texture and segmentation parameters for individual vegetation communities.

1.3 Objectives

The overarching aim of this thesis is to develop and apply novel remote sensing techniques to UAS acquired data for the generation of spatial information suitable for fine-scale saltmarsh mapping and monitoring.

The thesis outlines three analysis frameworks:

1. Radiometric sensor correction framework for a lightweight 6-band multispectral UAS sensor;
2. Spatial generalisation framework to identify optimal class-specific scales of analysis utilising texture model and GEOBIA segmentation parameters; and
3. Biomass estimation framework based upon field-derived above-ground biomass (AGB) allometric models and UAS-derived vegetation structure.

The specific objectives of this research are:

1.3.1 Objective 1

Assess sensor artefacts of a 6-band multispectral UAS sensor and identify physical and electrical sources of data collection errors. Assess existing approaches to the correction of sensor error. Incorporate suitable correction methods into a rigorous framework that is transferable between sensor systems.

- Assess sources of sensor error within the TetraCam Miniature Multiple Camera Array (mini-MCA).

- Develop an automated framework to pre-process raw Mini-MCA data into radiometrically corrected, aligned multispectral images.
- Demonstrate the data quality improvement of the corrective framework using real-world saltmarsh data.

1.3.2 Objective 2

Assess the performance of the UAS ultra-fine resolution sample scale for image classification. Assess existing image texture modelling and GEOBIA segmentation methodologies for spatial generalisation. Develop image texture modelling and GEOBIA segmentation frameworks to spatially generalise ultra-fine UAS spatial resolution to an optimal class-specific analysis scale.

- Assess the effect of the fine-scale sampling of UAS data on the classification of saltmarsh data.
- Research and develop a texture framework using IDL that compares texture models and measures to identify relevant class-specific scales of analysis.
- Research and develop a GEOBIA framework using the OGR/GDAL libraries within the Python programming language to assess segmentation parameters and identify class-specific scales of analysis.
- Assess the performance of both the texture and GEOBIA frameworks for the classification of UAS saltmarsh data.
- Explore the potential complimentary nature of texture and GEOBIA approaches to spatial generalisation.

1.3.3 Objective 3

Explore the UAS capacity to generate AGB estimations of fine spatial scale vegetation. Develop methodology to extract structural and AGB allometric parameters from fine-scale UAS samples. Assess the direct substitution of field-based shrub allometric parameter measurements with UAS-derived measurements.

- Research and develop structural and AGB field-based shrub allometric models utilising destructive sampling.
- Identify and develop framework that utilises structure-from-motion and GEOBIA to extract suitable allometric parameters from fine-scale UAS data.
- Assess the transfer of parameter measurement from field to UAS observation.

1.4 Thesis Structure

This thesis is presented as a collection of related scientific articles. The structure of the thesis follows a UAS remote sensing workflow, starting from data pre-processing, through to image analysis techniques and finally the application of UAS remote sensing. Chapter 2 is focused upon Objective 1 and details the development of a sensor correction framework for the mini-MCA. Chapters 3 and 4 cover Objective 2. Chapter 3 is the development of a texture framework for the assessment and identification of class-specific texture metrics. Chapter 4 focuses upon a GEOBIA framework that identifies class-specific segmentation parameters. Chapter 4 builds upon Chapter 3 by incorporating the identified texture metrics into GEOBIA to assess the complementary nature of image texture and GEOBIA. Chapter 5 extends the value of UAS measurements for monitoring, by comparing field and UAS observations for the calculation of AGB biomass. Chapter 6 provides concluding remarks on the overall achievements of the thesis, limitations, and suggests future directions for UAS research.

Chapter 2

Sensor Correction of a 6-Band Multispectral Imaging Sensor for UAS Remote Sensing

The focus of Chapter 2 is upon the development of a radiometric sensor correction framework. The chapter provides an assessment of a 6-band multispectral sensor by identifying physical and electrical sources of data collection error, and the development of a framework to correct sensor error. The work comprising this chapter is published in the peer-reviewed *Journal of Remote Sensing* (Kelcey and Lucieer, 2012).

2.1 Abstract

Unmanned aircraft systems (UAS) represent a quickly evolving technology, broadening the availability of remote sensing tools to small-scale research groups across a variety of scientific fields. Development of UAS platforms requires broad technical skills covering platform development, data post-processing, and image analysis. UAS development is constrained by a need to balance technological accessibility, flexibility in application and quality in image data. In this study, the quality of UAS data acquired by a miniature

6-band multispectral imaging sensor was improved through the application of practical image-based sensor correction techniques. Three major components of sensor correction were focused upon: noise reduction, sensor-based modification of incoming radiance, and lens distortion. Sensor noise was reduced through the use of dark offset data. Sensor modifications due to the effects of filter transmission rates, the relative monochromatic efficiency of the sensor and the effects of vignetting were removed through a combination of spatially/spectrally dependent correction factors. Lens distortion was reduced through the implementation of the Brown–Conrady model. Data post-processing serves dual roles in data quality improvement, and the identification of platform limitations and sensor idiosyncrasies. The proposed corrections improve the quality of the raw multispectral data, facilitating subsequent quantitative image analysis.

2.2 Introduction

Unmanned aircraft systems (UAS) are gaining attention from the scientific community as novel tools for remote sensing applications (Zhou and Ambrosia, 2009). Compared with more traditional aircraft or satellite based platforms, the UAS fills a previously unoccupied niche due to the unique characteristics of data it is able to capture. Its low operating altitude allows for the generation of ultra-fine spatial resolution data over relatively small spatial extents (Dunford et al., 2009) (see Fig. 2.1). Furthermore, the greatly reduced preparation time of UAS relative to large scale platforms aids in the acquisition of multi-temporal datasets or in exploiting limited windows of opportunity (Laliberte et al., 2007). UAS may serve to bridge the gap in spatial scale between satellite data, full-scale aerial photography, and field samples.

The UAS offers an unprecedented level of accessibility to and control over a remote sensing platform. Progress within the fields of digital sensors, navigational equipment, and small-scale aircraft have all reduced the cost of the fundamental components of UAS (Pastor

(a) Aerial orthophoto (60 cm) (b) UAS orthophoto (5 cm) (c) Terrestrial oblique photo

Figure 2.1: Comparative imagery of saltmarsh captured at different spatial scales with : aircraft (60 cm), UAS (5 cm), terrestrial.

et al., 2007). With the growing availability of relatively low-cost commercial components, small-scale research groups are now presented with the alternative of developing their own UAS-based projects. A wide selection of digital sensors allows researchers to cater systems for their own specific research requirements. This flexibility is being demonstrated in a growing number of remote sensing UAS studies. Berni and Zarco-Tejada (2009), Lelong (2008), Dunford et al. (2009), Hunt, Jr. et al. (2010), Laliberte et al. (2011b), and Xiang and Tian (2011) looked at multispectral UAS data for both agricultural monitoring and natural vegetation classification. Zhao et al. (2006) and Lin et al. (2011) used UAS-based LiDAR for topographic modelling and feature identification. UAS were used for stereo-image 3D landscape modelling by Stefanik et al. (2011). Thermal UAS applications for emergency services, including bushfires and search and rescue, were presented by Rudol and Doherty (2008), Hinkley and Zajkowski (2011) and Pastor et al. (2011). Temporal mapping of landscape dynamics was reviewed by Walter et al. (2009).

The accessibility of UAS platforms requires an increase in skillsets for research groups. Technical skills are required that cover all aspects of platform development, data post-processing, and image analysis. In response to this requirement, workflow methodologies for developmental aspects of UAS construction are being formulated. For example, Laliberte et al. (2011a) demonstrates a UAS workflow that incorporates raw data conversion,

band alignment, radiometric calibration and orthorectification into a single framework.

The objective of this study is to provide a primarily image-based, linear workflow of the sensor correction of a low-cost consumer grade multispectral sensor. In addition to providing a practical context for the theoretical background of sensor correction, our study will highlight the advantages, limitations, and pitfalls associated with UAS-based multispectral remote sensing through:

- identification, assessment and quantification of the components of data modification within a consumer level multispectral sensor;
- implementation of image-based radiometric correction techniques; and
- assessment of post-radiometric correction data quality issues.

2.2.1 UAS Multispectral Sensors

Despite the opportunities provided by UAS, both hardware and software limitations result in some compromises. As a remote sensing platform, the UAS is relatively limited in both its payload capacity and flight duration (Pastor et al., 2007). It is necessary to balance platform accessibility with the technological limitations inherent of small-scale platforms and the data quality of low-cost sensors. Such cost and weight limitations necessitate a reduction in manufacturing quality of the sensor. Reductions are readily achieved through the use of cheaper construction materials and methods, limited data storage capacity, or the absence of on-board processing features.

Multispectral sensors offer powerful opportunities for environmental remote sensing with UAS platforms. A multispectral sensor collects spectral data from multiple discrete bands of the electromagnetic spectrum. The flexibility of multispectral sensors arises from the user's ability to preselect and/or interchange the spectral filter elements within individual channels. This allows the strategic targeting of specific bands of the spectrum (Clodius et al., 1998). A wealth of literature has established the value of spectral indices derived

from multispectral data for the extraction of physical or biophysical information from spectral data. Glenn et al. (2008) demonstrates the use of vegetation indices as indicators for other vegetative biophysical information. A comparative study by Lacava et al. (2010) between field measurements and remotely sensed data revealed the value of spectrally derived wetness indices for estimating soil moisture.

The miniature camera array (mini-MCA) is a relatively low-cost consumer level six-band multispectral sensor available from Tetracam inc[1]. The mini-MCA consists of an array of six individual channels, each consisting of a Complementary metaloxidesemiconductor (CMOS) sensor with a progressive shutter, an objective lens, and mountings for interchangeable band-pass filters. The mini-MCA Channels are labelled from "1" to "5", while the sixth "master" channel is used to define the global settings used by all channels (e.g. integration time). Image data are collected at a user-definable dynamic range of either 8 or 10 bits. Provided factory standards detail the relative monochromatic response of the CMOS across the visible and NIR wavelengths. In-house modifications made to the mini-MCA include UAS mountings and alterations to the bandpass filter holders to allow for easier interchange of the filters (see Fig. 2.2).

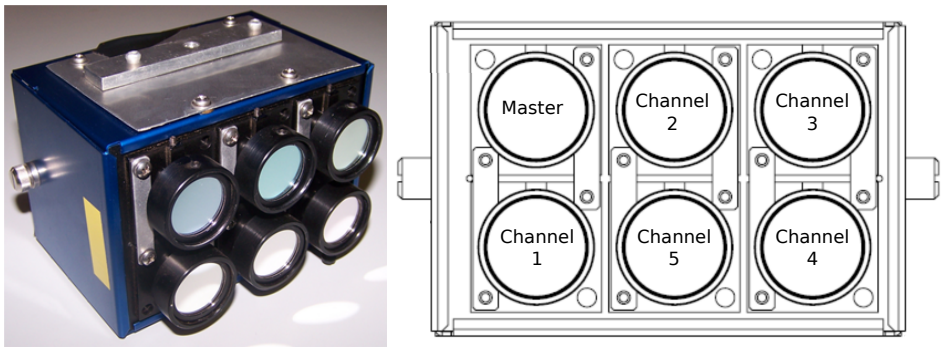

(a) The Mini-MCA (b) Layout of the six channels of the Mini-MCA.

Figure 2.2: A modified Tetracam Miniature Multiple Camera Array (Mini-MCA) and channel layout.

Each of the mini-MCA channels is equipped with mountings for the fitting of interchange-

[1]http://www.tetracam.com/

able 1″ band-pass filters. The mini-MCA is purchased with six filters preselected by the user. An additional six band-pass filters were obtained from the Andover corporation[2]. The twelve 10 nm bandwidth filters are presented in Table 2.1, and were selected from across the visible and NIR wavelengths with close regard to known biophysical indices developed for environmental monitoring purposes (Asner, 1998).

Table 2.1: Filter wavelength and potential role in vegation monitoring.

Wavelength (nm)	**Biophysical Measurement**
450	Vegetation Index (Modified Red Edge)
490	Dry or Senescent Carbon (Plant Senescence Reflectance Index)
530	Light Use Efficiency (Photochemical Reflectance Index)
550	Leaf Pigmentation (Anthocyanin Reflectance Index)
570	Light Use Efficiency (Photochemical Reflectance Index)
670	Dry or Senescent Carbon (Plant Senescence Reflectance Index)
700	Leaf Pigmentation (Anthocyanin Reflectance Index)
720	Vegetation Index (Vogelmann Red Edge)
750	Dry or Senescent Carbon (Plant Senescence Reflectance Index)
800	Leaf Pigmentation (Anthocyanin Reflectance Index)
900	Water Content (Water Band Index)
970	Water Content (Water Band Index)

Raw at-sensor data has been modified by a combination of effects that include surface conditions, atmospheric effects, topographic effects and sensor characteristics (Smith and Milton, 1999; Mahiny and Turner, 2007). These effects obscure the true surface reflectance properties and diminish the capacity to extract accurate quantitative information from remotely sensed data. Radiometric post-processing encompasses the suite of techniques to extract spatially consistent surface reflectance values from the raw data and is conducted across two main phases: sensor correction and radiometric calibration.

[2]http://www.andovercorp.com/

Sensor corrections and radiometric calibration are sequential steps in the task to extract high quality reflectance data (see Fig. 2.3). Sensor correction encompasses the methods used to extract geometrically consistent at-sensor measurements from raw data. The focus of this initial phase is therefore upon reducing sensor-based data modifications. Radiometric calibration further builds upon the correction results by deriving at-surface reflectance from these at-sensor measurements. This is achieved through the calibration of data with regard to the environmental conditions present during data collection (Cooley et al., 2002). The primary focus of this study is on the preliminary corrections for sensor correction. A single multispectral image provides a case study to illustrate the effects of sensor corrections.

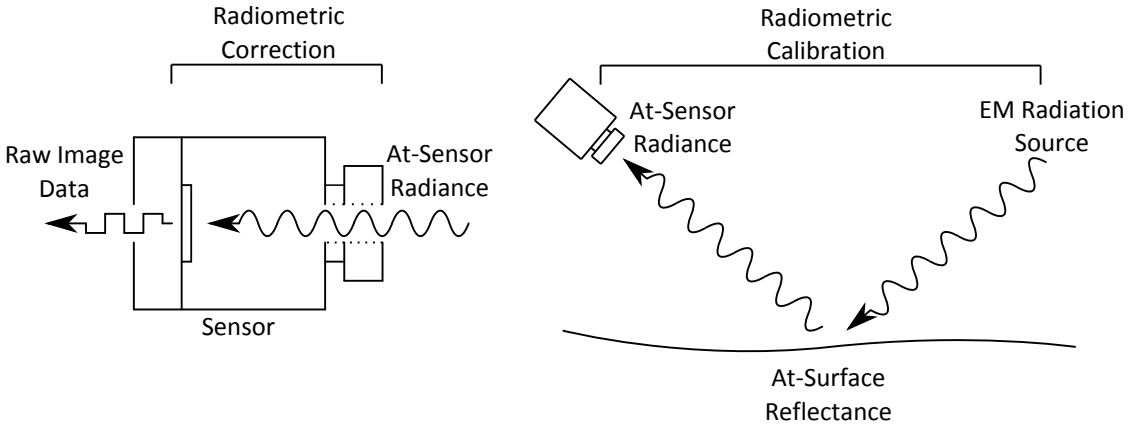

Figure 2.3: Image data pre-processing: Sensor correction and data radiometric calibration.

2.3 Methods

Raw at-sensor data values represent arbitrary units of highly modified at-sensor measurements (Smith and Milton, 1999). These modifications may occur during the collection, processing, and transmission of data by the sensor system (Al-amri, 2010), and include processes that either introduce unwanted additional measurements or directly alter the strength or spatial properties of the incoming radiance (Smith and Milton, 1999; Mansouri et al., 2005). Sensor correction encompasses the suite of techniques for correcting

these sensor based processes, allowing the extraction of arbitrary digital numbers (DN). Raw data conversion, processing and sensor correction application were conducted using IDL script within the ENVI software package (http://www.ittvis.com/). Raw mini-MCA data was converted into individual 10 bit image bands.

2.3.1 Noise Correction

Small, low-cost sensors are prone to the effects of noise. Sensor noise collectively refers to erroneous sensor measurements generated independently to collected radiance, and therefore represent an additive source of error to the data (Al-amri, 2010). Noise is characterised into two broad components: systematic and random. Systematic noise represents a source of bias consistent in both its value and spatial properties. Conversely, random noise refers to the introduction of non-correlated, non-reproducible noise that varies randomly over time (Mansouri et al., 2005). Noise reduction techniques include image-based approaches (Mansouri et al., 2005) and signal processing techniques that are used to isolate high frequency non-correlated data components (Al-amri, 2010; Changyanab, 2008).

The value of each pixel within the raw data represents the sum of a radiance component and a noise component (see Equation (2.1)). The larger the proportion of noise within the image data, the more obscured the true radiance component becomes (see Fig. 2.4). The separation of this radiance component requires quantification of the contribution of the noise components to the raw data.

$$DN_{raw} = DN_{rad} + DN_n \tag{2.1}$$

The complete removal of noise from data is undermined by the uncertainty surrounding the exact contribution of the random component of noise. Given its temporally random properties, the exact contribution of the random component to the value of a pixel at

any given moment is unknown and cannot be accurately separated from the radiance component (see Equation (2.2)). Noise correction techniques are therefore forced to focus upon reductive techniques rather than outright removal. Knowledge of the per-pixel noise distribution characteristics are key for approximating the contribution of random noise.

$$DN_{raw} = DN_{rad} + (DN_{sn} + DN_{rn}) \tag{2.2}$$

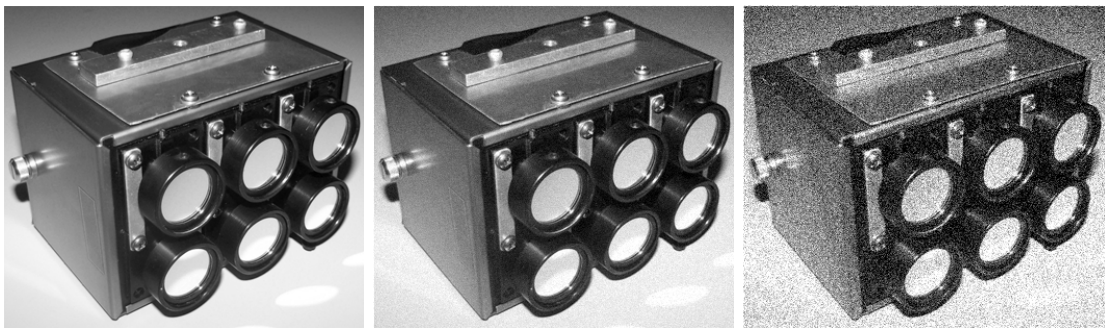

(a) Image of the Mini-MCA (b) Effect of 5 % noise (c) Effect of 25 % noise

Figure 2.4: Illustration of the effects of increased noise proportion: Original image, 5 % noise, 25 % noise

Dark Offset Subtraction

Characterisation of the noise component exploits its independent origin from the radiance component. Through the physical isolation of the sensor from incoming radiance, the radiance component can be globally reduced to zero. Dark offset data are raw image data generated such that it contains only the noise component (Mansouri et al., 2005; Mullikin et al., 1994). Each dark offset image represents a single sample of the per-pixel noise within the sensor. Through repetition, a sensor-specific database of dark offset data can be constructed and characteristics of the per-pixel distribution of noise extracted. Dark offset subtraction is the subtraction of the per-pixel mean value of these noise distributions from image data. The standard deviation of the distribution provides a new measure of noise that, on average, will remain following dark offset subtraction. It is important to

note that dark offset is only an estimate of the per-pixel noise, and may over- or under-estimate the actual noise contribution. Therefore the standard deviation as a measure of noise may represent either an additive or subtractive deviation to a pixel's true value.

Dark Offset Image Generation Methodology

Dark offset data was generated for the mini-MCA within a dark room. To ensure radiance was excluded from the mini-MCA, it was first covered with a protective cloth before envelopment with a tightly fitting Gore-Tex hood. This setup was found to be both practical and capable of blocking incoming radiance across the relevant visible and NIR wavelengths.

Dark offset sample images were generated for each of the six mini-MCA channels at multiple exposure levels ranging from 1,000 µs to 20,000 µs (at 1,000 µs increments). For each 1,000 µs exposure step, 125 dark offset sample images were generated for each of the six channels. The per-pixel mean and standard deviations were calculated for each combination of sensor and exposure and stored as separate images.

2.3.2 Radiance Strength Modification

Modifications to radiance strength within a sensor exhibit either a spectral or spatial dependency. Spectrally dependent processes include both filter transmittance and the monochromatic response of the sensor. Conversely, vignetting is a spatially dependent reduction of illumination strength dependent upon the angle of incoming radiance.

Monochromatic Response

Sensors exhibit additional non-uniformity to spectral response due to the effects of quantum efficiency. Sensors are dependent upon the photoelectric effect to generate charges from which to construct image data. Not every photon, however, generates a charge.

Quantum efficiency defines the proportion of incoming photons capable of liberating electrons through the photoelectric effect (Mullikin et al., 1994). The quantum efficiency of sensors varies both between materials and across wavelengths, therefore altering the amount of incoming radiance required to generate a proportionate charge between differing bandpass filters. Factory standards of the relative monochromatic response of the mini-MCA effectively describe the quantum efficiency across the visible and NIR spectrum (450 nm to 1,100 nm) (see Fig. 2.5).

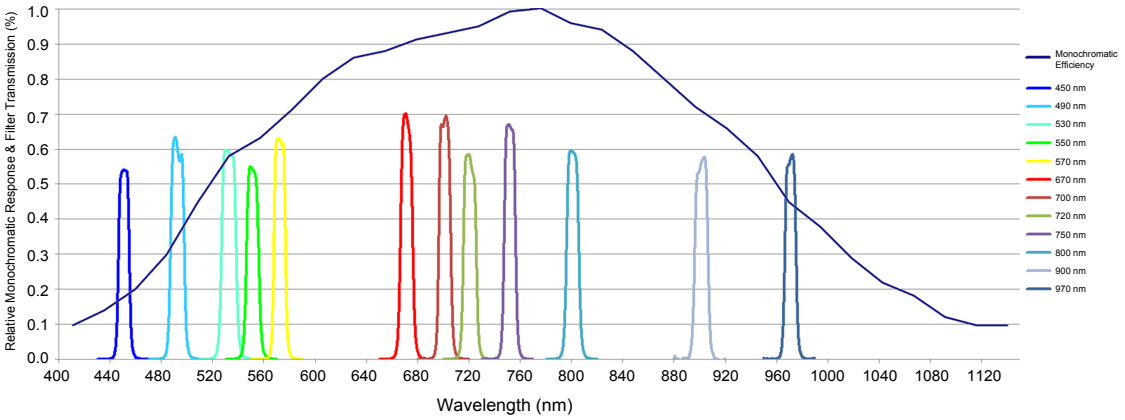

Figure 2.5: Relative Monochromatic Response and Absolute Filter Transmission.

Filter Transmittance

The mini-MCA provides multispectral functionality through mountings for spectral bandpass filters. These filters, however, neither exhibit 100 % transmittance across their functional wavelength nor define discrete limits of equal spectral sensitivity. Instead, they exhibit variation in both spectral sensitivity over their defined bandwidth and transmission level between filters at different wavelengths. Factory standards for the acquired 12 bandpass filters express the transmission rate of each individual filter, exhibiting a range of signal transmission rates as high as 70 % for the 670 nm filter to as low as 55 % for the 450 nm filter (see Fig. 2.5).

The combined effect of filter transmission rate and monochromatic efficiency results in a

wavelength dependent global reduction in radiance strength (see Equation (2.3)). This has effects both within and between bands in the mini-MCA. Reducing the radiance component increases the overall contribution of noise in the raw data. As such, filter selection strongly influences the signal-to-noise ratio (SNR) within the final data. Inter-band relationships are degraded through the wavelength dependent reductions in radiance, generating disproportionate relationships between bands of high/low radiance modification.

$$DN_{raw} = DN_{rad} * FT_{\lambda} * ME_{\lambda} + (DN_{sn} + DN_{rn}) \tag{2.3}$$

Little can be done to address the disproportionate noise. The correct future application of radiometric calibration techniques will compensate for disproportionate inter-band relationships. Studies that lack a suitable radiometric calibration approach, and are therefore limited to analysing either DN or at-sensor radiance measurements, require the separate calculation and application of corrective factors to restore at-sensor radiance measurements. Given that the two processes are both global reductions in radiance strength dependent on wavelength, the simplest approach is the calculation of a single correction value. This value is specific to both filter and sensor and is derived from multiplicative effects of both transmission and efficiency rates. Each image band is then globally multiplied by the corresponding correction factor.

2.3.3 Wavelength Dependent Correction Factor Methodology

Wavelength dependent correction factors were calculated from a combination of filter transmission and monochromatic efficiency. For simplicity, the detector was assumed to exhibit a linear response to radiance. The combined reduction in transmission rate was calculated over a 10 nm bandwidth from the factory standard values provided by Andover[3]. An estimation of the relative monochromatic response was estimated from the information provided by TetraCam.

[3]http://www.andovercorp.com/

Flat Field Correction Factors

Vignetting is defined as a spatially dependent light intensity falloff that results in a progressive radial reduction in radiance strength towards the periphery of an image (Goldman, 2010; Kim and Pollefeys, 2008; Zheng et al., 2009). The primary source of vignetting arises from differences in irradiance across the image plane due to the geometry of the sensor optics. Widening angles increase the occlusion of light, leading to a radial shadowing effect as illumination is reduced (see Fig. 2.6). For a thorough review of the additional sources that contribute to the vignetting effect see Goldman (2010).

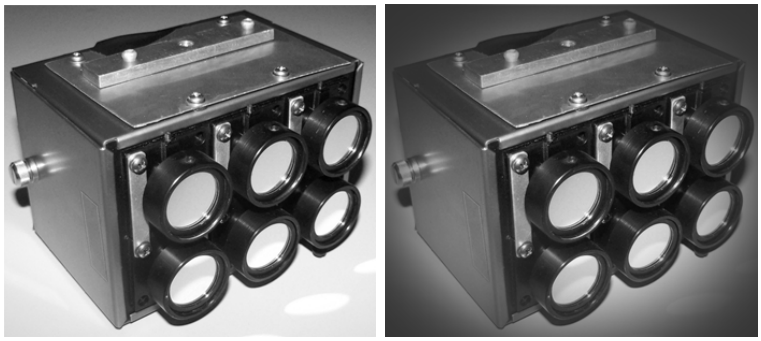

(a) Image of the Mini-MCA (b) Vignetting radial shadowing

Figure 2.6: Illustration of the radial shadowing effect of vignetting.

Two broad methods to vignetting correction involve either modelling the optical pathway or image-based techniques. Methods based upon modelling the optical pathway use characteristics of the sensor to derive a model to describe vignetting falloff. This model can then be applied to data to compensate for illumination reduction due to the effects of vignetting.

Image-based approaches to vignetting correction typically rely upon the generation of a per-pixel correction factor look-up-table (LUT). Relative to optical modelling approaches, image based LUTs are arguably both simpler to calculate and more accurate (Yu, 2004). LUTs require no knowledge of the optical pathway and represent the cumulative effects, including radial asymmetry, that contribute to the vignetting effect. Their overall de-

velopment and application is, however, more time consuming, as any alteration to the vignetting pattern requires the generation of a new LUT.

Correction factor LUTs are generated from a uniform, spectrally homogeneous, Lambertian surface known as a flat field. Within the generated flat field data, deviation away from the expected uniform surface is attributed to the radial falloff effect of vignetting. A quantitative assessment of the per-pixel illumination falloff within the flat field image may be calculated and corresponding correction factor data generated. Correction factor images are calculated on the assumption that the brightest pixel within the image represents the true radiance measurement free from the effects of vignetting. A multiplicative correction factor is then calculated for each pixel, based on its difference with this true radiance measurement (see Equation (2.4)) (Yu, 2004).

$$V_{LUT}(i,j) = \frac{V_{FF}(i,j)}{V_{FF}max} \tag{2.4}$$

A single flat field LUT corrects only for the vignetting characteristics present when the image was generated (Equation (2.5)). The quality of vignetting correction is degraded should variations in vignetting origin or rate of illumination falloff occur. Therefore the flat field LUT approach requires the identification of sources that generate variation within the vignetting effect. Although the aperture and focal lengths are known modifiers, both factors are fixed within the mini-MCA. Potential sources of vignetting variation include subtle variation between channels, exposure length and filters. The effect of individual channels were investigated by generating LUTs for each channel under equal conditions (i.e. filterless, equal exposure length). The effects of exposure length were investigated by generating LUTs from a single filterless channel across a range of exposure lengths. Finally, the effect of filters were investigated through a comparative investigation of filter and filterless LUTs upon a single channel.

$$DN_{raw} = DN_{rad} * FT_{\lambda} * ME_{\lambda} * V_{LUT}(i,j) + (DN_{sn} + DN_{rn}) \tag{2.5}$$

Vignetting Correction Methodology

A white artist's canvas was selected to serve as the flat field surface due to its clear white homogeneous near-Lambertian surface. Flat field images were generated within a dark room with the white canvas evenly illuminated. In order to maximise the noise reduction potential of the dark offset subtraction process, each final flat field image was generated from the mean of 125 flat field sample images. This process averages the random noise component within the data, thereby improving the correspondence of noise levels between the flat field image and the dark offset data. Correction factor images (i.e. LUTs) were then calculated from the noise-reduced mean flat field image.

2.3.4 Lens Distortion

Lens distortion is mainly generated through a combination of differences in magnification level across a lens surface and the misalignment between lens and the detector plane. These two factors result in a radially dependent geometric shift in a measurement position (Wang et al., 2009; Prescott and McLean, 1997; Hugemann, 2010). Lens distortion is commonly represented by two components: radial distortion and tangential distortion (Wang et al., 2009). Radial distortion represents the curving effect generated by subtle radial shift in magnification towards the centre of the lens, manifesting as a radial shift in value position (see Fig. 2.7). Negative displacement radially shifts points towards the origin point of lens distortion, resulting in pincushion distortion effect. Conversely positive displacement shifts points away from the lens distortion origin, resulting in a barrel distortion effect (Park et al., 2009; Jedlička and Potčková, 2007). Tangential distortion arises from the non-alignment of the lens with the CMOS resulting in a planar shift in the perspective of an image (Wang et al., 2009).

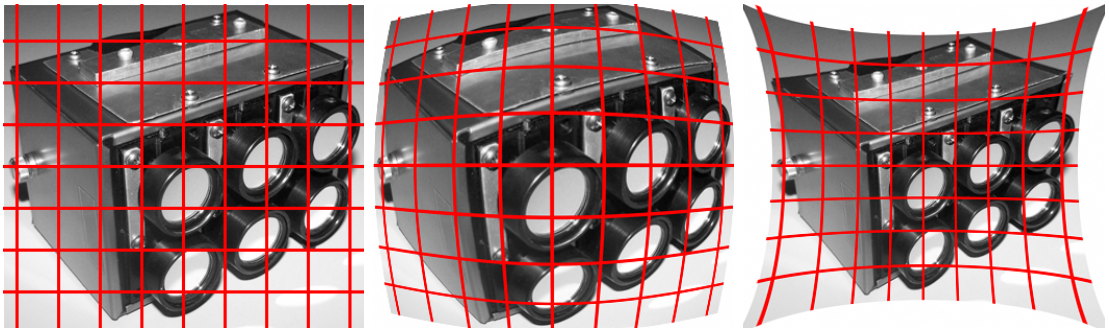

(a) Image of the Mini-MCA (b) Barrel distortion (c) Pincushion distortion

Figure 2.7: Illustration of the two forms of lens distortion: barrel lens distortion and pincushion lens distortion.

Brown–Conrady Model

A commonly adopted model for lens distortion is the Brown–Conrady distortion model (de Villiers et al., 2010; Wang et al., 2006; Hugemann, 2010). The Brown–Conrady model is capable of calculating both the radial and tangential components of lens distortion. The model utilises an even-order polynomial model to calculate the radial displacement of a given image point. It is commonly recommended this polynomial is limited to the first two terms of radial distortion as higher order terms are insignificant in most cases.

The Brown–Conrady model requires prior calculation of radial and tangential distortion coefficients. An accessible approach for the calculation of the coefficients is the utilisation of a planar calibration grid of known geometric properties. Multiple images are generated of the calibration grid from different orientations. An iterative process then estimates both the intrinsic and extrinsic camera parameters based upon point correspondence between the known geometric properties of the scene and the distorted points within the image.

Lens Distortion Correction Methodology

Agisoft Lens[4] is a freely available software package that utilises planar grids to calculate the Brown–Conrady coefficients. The calibration grid was displayed upon a 24″ flat panel

[4]http://www.agisoft.ru/

LCD screen. Data of the calibration grid was captured by a filter-free mini-MCA at multiple angles. For each angle, multiple images were collected and mean calculated in order to maximise noise reduction. Filter-free vignetting correction factors were applied to the corresponding channel. Agisoft Lens was then used to calculate the lens distortion coefficients for each channel based upon the Brown–Conrady model.

2.3.5 Saltmarsh Case Study

Saltmarsh is a coastal or riparian vegetation type characterised by herbaceous or low woody plants (Adam, 2002) that exhibit a tolerance towards water logging and/or saline conditions (Emery et al., 2001). Saltmarshes establish in regions where gentle topographic gradients that exist between the land and sea undergo periodic seawater inundation (Pennings and Callaway, 1992). Plant communities within saltmarshes often exhibit marked zonation in their distribution (Pennings and Callaway, 1992; Emery et al., 2001; Adam, 2002). It has been hypothesised that this is due to factors of drainage and salinity, and that increasing gradients of salt and water logging result in the successive elimination of species based upon tolerance (Emery et al., 2001). The limited vertical stratification and relative topographic flatness of saltmarsh communities represents an ideal, simplified environment within which to conduct preliminary UAS studies.

The UAS used in this study was the "Oktokopter" (see Fig.). The Oktokopter is an eight rotor micro-UAS supplied by HiSystems[5]. A navigation grade GPS reciever (U-blox LEA65) and an IMU allow the Oktokopter to fly autonomously through a pre-defined set of waypoints. The Oktokopter had a payload capacity of approximately 1 kg and a gimballed camera mount allows for automated self-leveling of fitted payloads. The Oktokopter had a flight duration of approximately 5-6 minutes. This allowed the coverage of approximately 4-5 ha, with larger areas requiring multiple flights. UAS imagery was generated at maximum rate allowable by the sensor, providing both high image overlap

[5]http://www.mikrokopter.com/

and redundancy for poor quality individual images (Turner et al., 2012; Lucieer et al., 2014; Turner et al., 2014).

Figure 2.8: The Oktokopter inflight with a mini-MCA payload.

UAS data of saltmarsh communities was acquired from the foreshore of Ralphs Bay, Australia (see Fig.2.9). Six band multispectral data was captured using the mini-MCA mounted upon an Oktokopter UAS frame (see Table 2.2). Six bandpass filters were selected: 490, 530, 570, 670, 700 and 750 nm. These were selected to measure plant senescence, anthocyanin (plant stress), and light use efficiency (see Table 2.1). A single multispectral image was selected to serve as a worked example of sensor corrections.

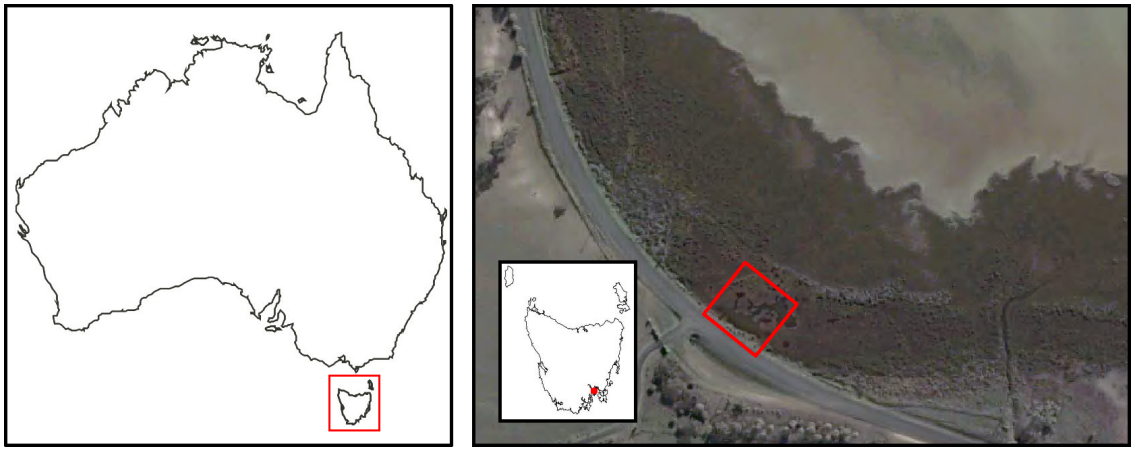

Figure 2.9: QuickBird image and location of Ralphs Bay study site in Tasmania, Australia.

Table 2.2: Ralphs Bay Saltmarsh UAS Data Acquisition Details.

Date	Site	Longitude	Latitude	Height (m)	Exposure (µs)
25/11/2012	Ralphs Bay	42°55.742'S	147°29.036'E	100 m	4,000

2.4 Results

2.4.1 Dark Offset Subtraction

Dark offset samples were generated for each channel of the mini-MCA. A preliminary visual assessment illustrates the similarities and differences in noise value, variation, and structure between the channels (see Fig. 2.10). Three prominent manifestations of noise are exhibited: global checkered gains, horizontal band noise, and strong periodic noise within channels 1 and M.

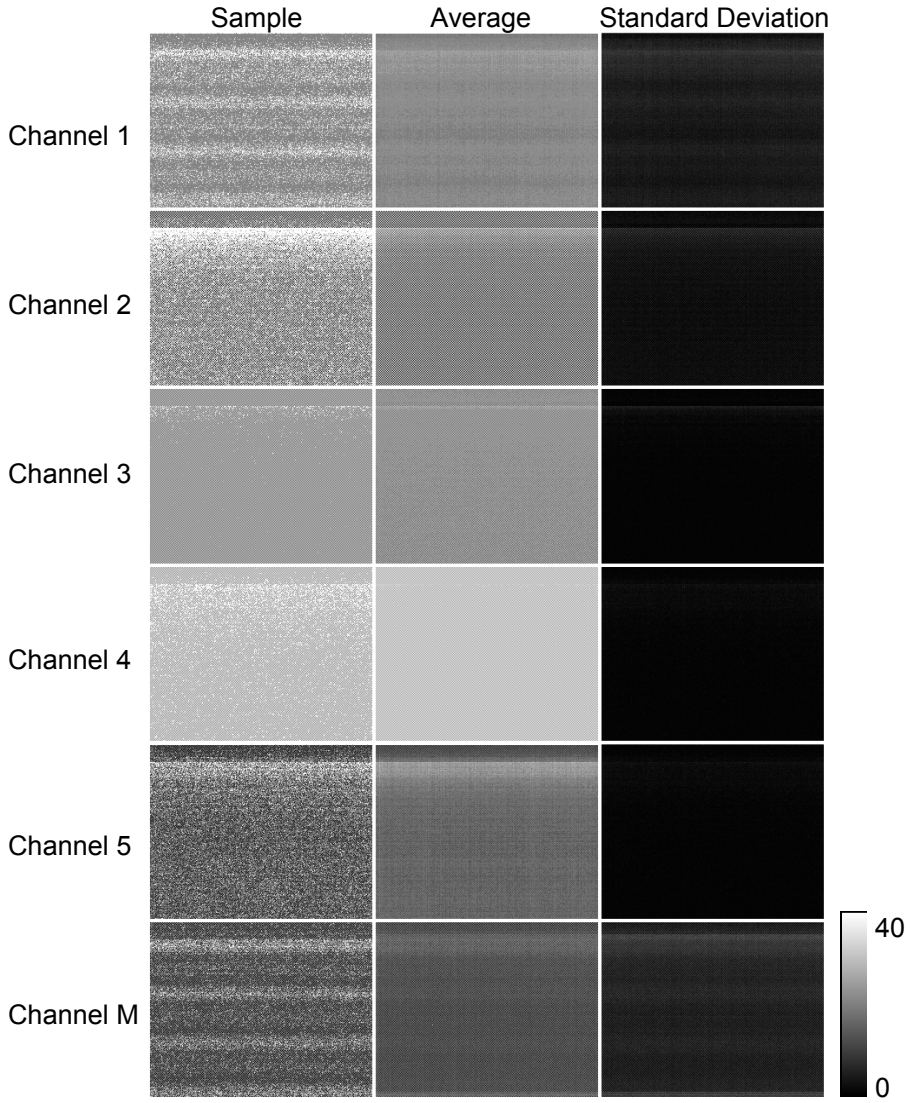

Figure 2.10: Dark offset data from the six channels of the mini-MCA: single sample, mean of 125 samples, standard deviation of 125 samples.

Global Checkered Gains

Examination of the mean per-pixel noise value and standard deviation reveals a bimodal distribution across the dark offset data (see Fig. 2.17). A close visual inspection of the data reveals an alternating per pixel gain in the structure of the noise. This bimodal distribution is most strongly evident within channel 2, while the overlapping distributions of channel 1 only become clear within an examination of the differing standard deviations.

Data was divided into two separate images based upon alternating pixels, with histograms of each of the alternating pixel gain states illustrating a clear separation of the bimodal distribution into two distinct distributions (see Fig. 2.12). As the bimodal condition between different channels is variable, the relationship between channels may either mask or reveal its effects with greater prominence (see Fig.2.13).

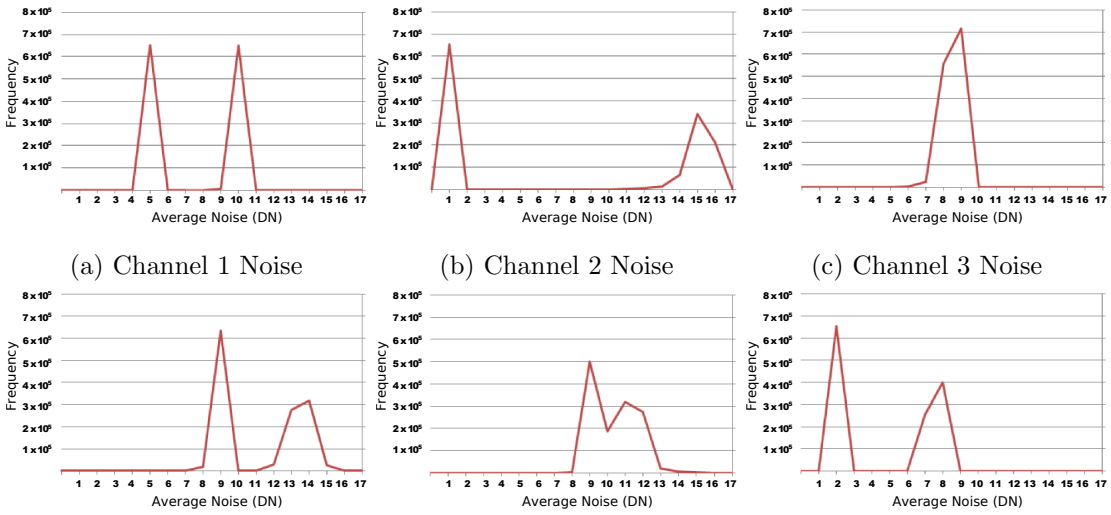

(a) Channel 1 Noise (b) Channel 2 Noise (c) Channel 3 Noise

(d) Channel 4 Noise (e) Channel 5 Noise (f) Channel M Noise

Figure 2.11: Distribution of noise within dark offset data for all six channels of the mini-MCA (Exposure 1,000 µs).

The dual gain states within the channels raises two considerations with regard to noise: the potential for noise reduction of individual gain states and the introduction of psuedo-texture. Lower standard deviations imply increased potential for noise removal. Inconsistent variation is however evident between gain states within individual channels across the mini-MCA (see Fig. 2.17). Distributions are generally Gaussian with a variable degree of negative skewing (see Table 2.3).

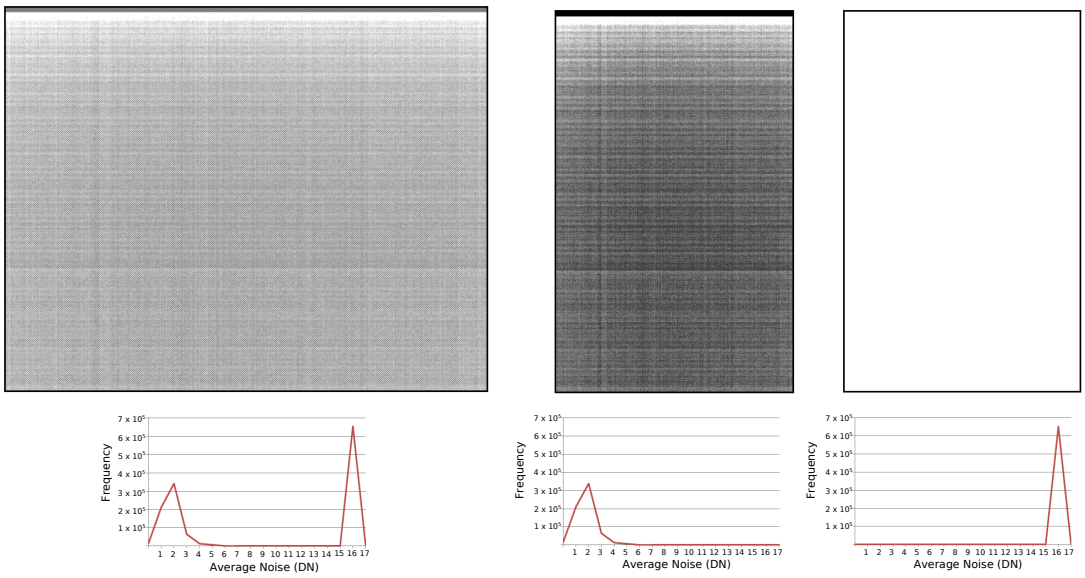

(a) Complete image exhibiting bimodal condition.

(b) State 1 of the bimodal condition

(c) State 2 of the bimodal condition

Figure 2.12: Separation of bimodal condition within Channel 2 of the mini-MCA (Exposure 1,000 µs).

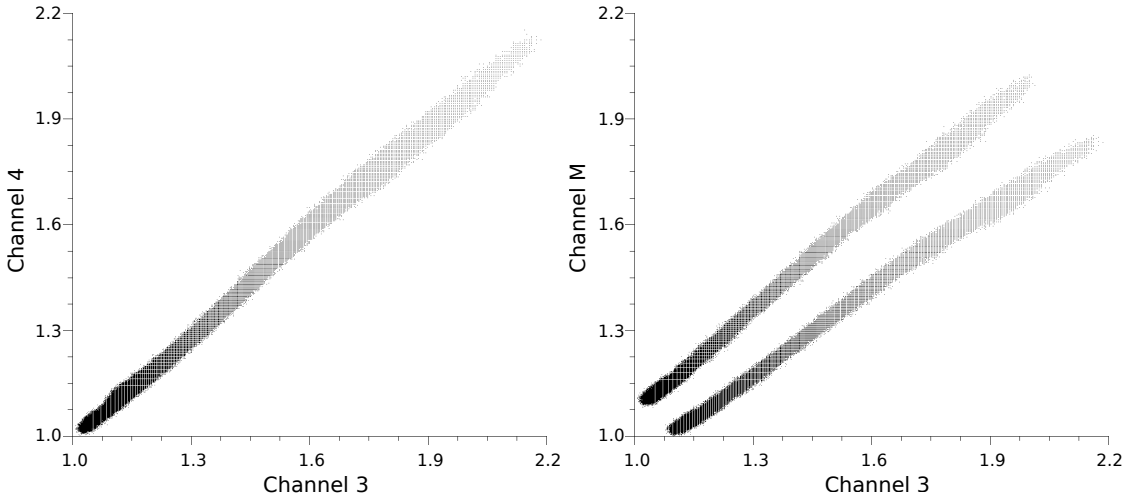

(a) Single distribution between Channel 3 & 4

(b) Double distribution between Channel 3 & M

Figure 2.13: Relationship between channels may either mask or reveal bimodal condition within the mini-MCA, potentially giving rise to multiple radiance distributions.

Table 2.3: Sensor Noise Characteristics.

Channel	State	Mean	StDev	Skew
1	1	8.445	0.650	-3.379
	2	8.452	0.6817	-2.987
2	1	1.828	0.884	1.559
	2	15.972	0.670	-23.798
3	1	6.999	0.317	-18.182

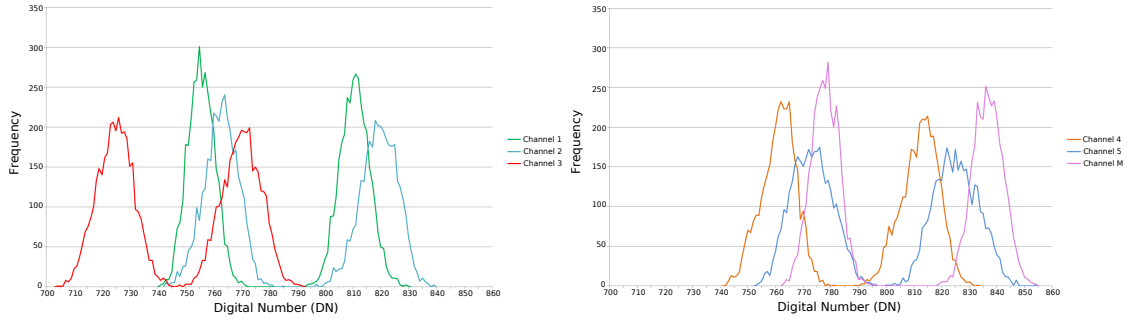

(a) Bimodal condition in channels: 1, 2 & 3 (b) Bimodal condition in channels: 4, 5 & M

Figure 2.14: Flat field subsample illustrating pronounced bimodal condition within each channel.

Pseudo-texture effects are generated through the differing bias of the individual gain states within a channel. This effect is most evident across homogeneous surfaces where the alternating gain imposes a checkerboard texture. The greater the difference of a channel's gains, the stronger the pseudo-texture effect. Dark offset subtraction, however, does not offer substantial removal of this checkered effect. The origins of this checkered effect, rather than being a direct noise contribution, appears to be a by-product of on-board processing within the mini-MCA. The introduction of a radiance component generates data occupying more of the available dynamic range, which in turn exhibits a substantial increase in the separation between states. The degree of variation between states within this data overwhelms the estimated noise contribution by two orders of magnitude, resulting in differences between states that exceed 5% of the dynamic range (see Fig. 2.14). As such, dark offset subtraction is severely limited in reducing this effect.

Periodic Noise

Individual dark offset samples illustrate the dominant and unpredictable nature of the periodic noise contaminating channels 1 and M (see Fig. 2.10). Averaging multiple samples results in a smoothing effect of this periodic noise, revealing an underlying noise structure similar to that within the remaining four channels (see Fig. 2.10). This effect of

smoothing suggests stationarity of a periodic wave across multiple samples, thus implying a consistent source for the noise.

Despite its restriction to channels 1 and M, the exact source of periodic noise remains unknown. Its dominant presence and unpredictability reduce the influence of dark offset subtraction upon the structure of the periodic wave (see Fig. 2.15). Given its stationarity, signal processing techniques may prove useful in identifying and eliminating the frequency of this periodic noise. Alternatively, the noise source within the mini-MCA may be identified, with the potential for internal modifications to reduce its effect.

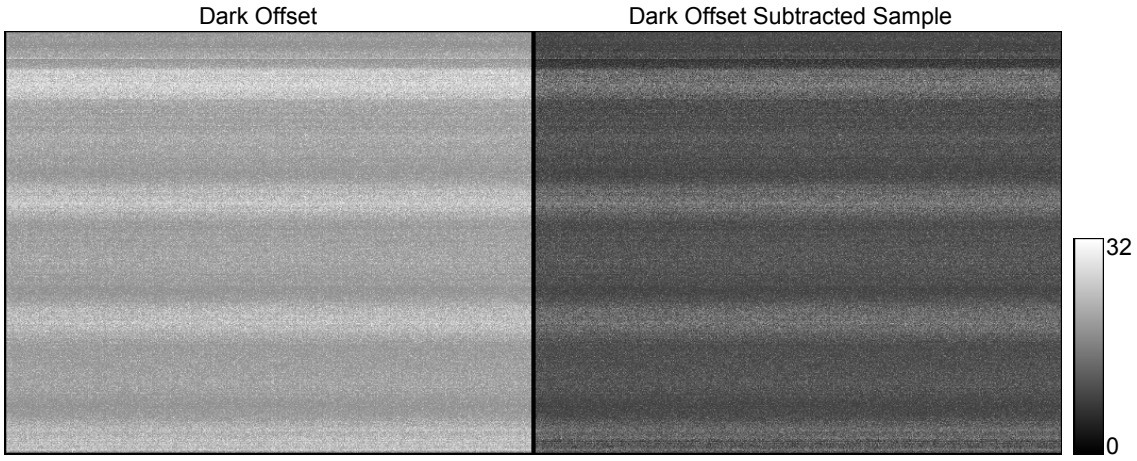

Figure 2.15: Illustration of the limited capacity for periodic structure removal with dark offset subtraction.

Progressive Shutter Band Noise

A strong horizontal band of noise occurs within all six channels of the mini-MCA, occupying approximately the same vertical position (see Fig. 2.10). The vertical positioning of this band, its value and standard deviation are all dependent upon the exposure length (see Fig. 2.16). Longer exposures progressively shift the band positions downwards, increasing both its value and standard deviation. Horizontal noise banding is a known artifact of CMOS sensors with progressive shutters. Despite its spatially predictable position, the increased standard deviation degrades the potential noise reduction of longer

exposures. Additionally, the sharp edge of this horizontal band often generates a noticeable delineation within the corrected data.

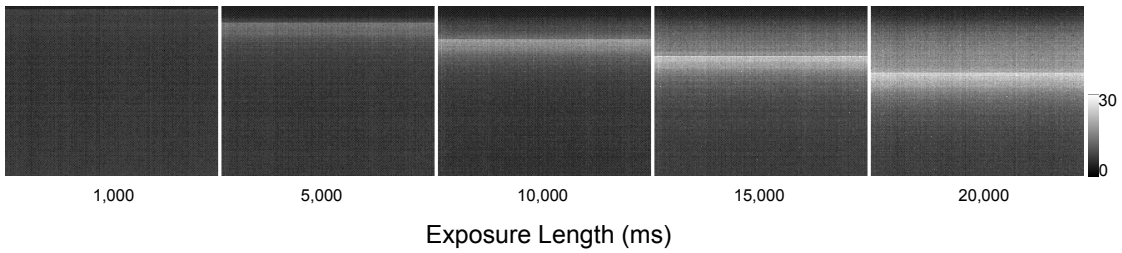

Figure 2.16: Illustration of the temporal progression of shutter band noise present within all channels of the mini-MCA.

2.4.2 Dark Offset Potential

Figure 2.17 illustrates a comparative effect of dark offset subtraction across a temporal scale for the mini-MCA. The two states of each channel are condensed into a single figure for both the mean and standard deviation at each exposure.

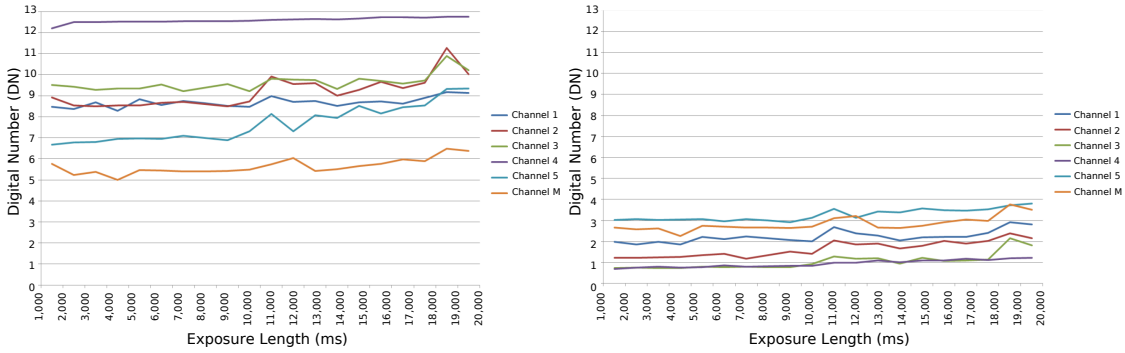

(a) Mean noise response.

(b) Standard deviation noise response.

Figure 2.17: Statistical response of noise to lengthening exposure.

2.4.3 Filter Transmission/Monochromatic Efficiency

Correction factors were calculated for both filter transmission rates and relative monochromatic efficiency (see Table 2.4). A single overall correction factor was generated to account for the cumulative effects of both processes. The importance of this correction step in the

restoration of interband relationships for DN data are demonstrated for a common vegetation spectral profile (see Fig. 2.18). The effect of both processes operates only upon the radiance component of the raw data, therefore as the noise component remains unaffected, reductions in radiance directly degrade the SNR. Since application of the correction factor inflates both the radiance and noise component equally, despite the restoration of the proportional representation of the radiance component between bands, the overall SNR between differing spectral bands remains unchanged.

Table 2.4: Filter Transmission/Monochromatic efficiency Correction Factors.

Filter (nm)	Filter Transmission (%)	Correction Factor	Monochromatic Efficiency (%)	Correction Factor	Multiplicative Correction Factor
450	0.44	2.28	0.16	6.25	14.27
490	0.47	2.13	0.34	2.97	6.32
530	0.47	2.12	0.56	1.80	3.81
550	0.45	2.21	0.62	1.61	3.57
570	0.44	2.26	0.67	1.49	3.38
670	0.56	1.80	0.91	1.10	1.98
700	0.56	1.79	0.93	1.08	1.92
720	0.51	1.96	0.95	1.05	2.06
750	0.49	2.02	0.97	1.03	2.09
900	0.48	2.07	0.71	1.40	2.90
970	0.47	2.14	0.45	2.22	4.75

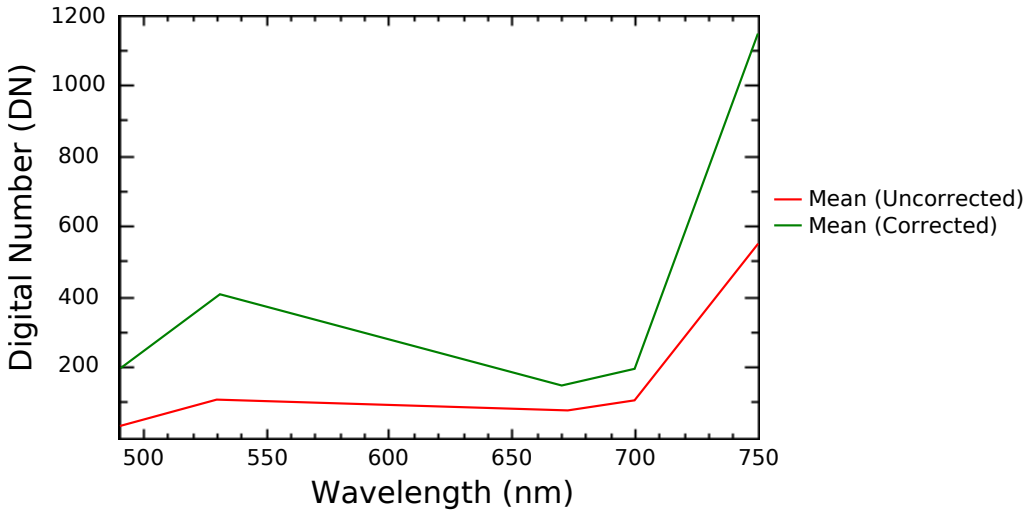

Figure 2.18: Effect of corrective factor upon mean spectral profile of saltmarsh sedge *Gahnia filum*.

The six channels of the mini-MCA share a single common exposure setting. To avoid overexposure, the exposure interval must be short enough to accommodate the highest filter efficiency present across the six channels. This leaves less efficient filters suffering a relative reduction in radiance strength. Radiance reduction therefore generates a filter dependent restriction upon the available dynamic range. Dynamic range ultimately represents the precision with which data are recorded, thereby defining the smallest difference between pixels that can be detected. Reductions in dynamic range result in coarser quantisation of the data as well as degrading the SNR. Although correction factors may restore values between bands to a proportional level, both this quantisation effect and SNR remain due to the original radiance reductions set by a single exposure.

2.4.4 Vignetting

Effect of Sensors

LUT images were generated for each mini-MCA channel without filters for vignetting correction. Uniform settings were maintained between channels for comparative purpose. The vignetting structure differs between sensors both in the point of origin and in the

rate of radial falloff. A visual assessment illustrates the shift in vignetting pattern origin generated by differences in the optical pathways between sensors (see Fig. 2.19). Dust particles are evident upon the lens of Channel 2, 5 and M.

Channels additionally exhibit varying rates of vignetting radial falloff (see Fig. 2.20). This rate of falloff is highest within channel M and lowest within channel 2. Channels 3, 4 and 5 all exhibit the most similarity in falloff rates. The variation exhibited in both origin and rate of radial falloff warrant the generation of channel specific vignetting correction LUTs.

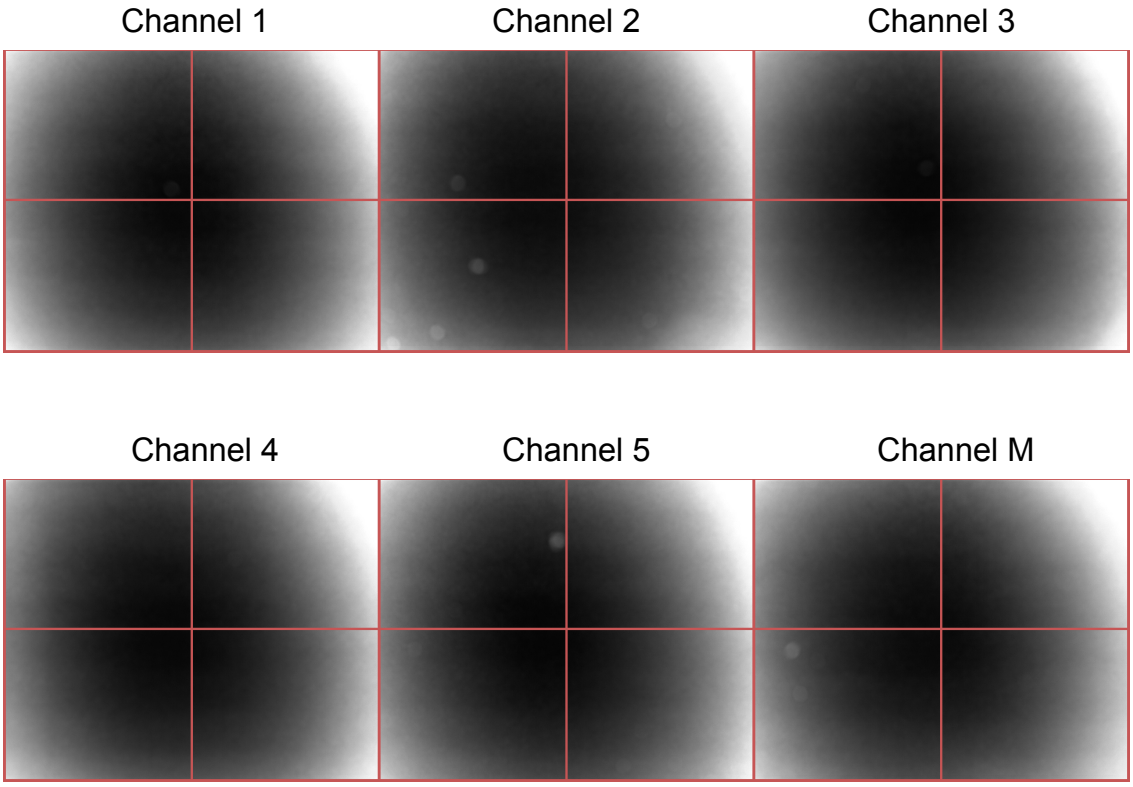

Figure 2.19: Vignetting LUTs generated from all six channels of the mini-MCA.

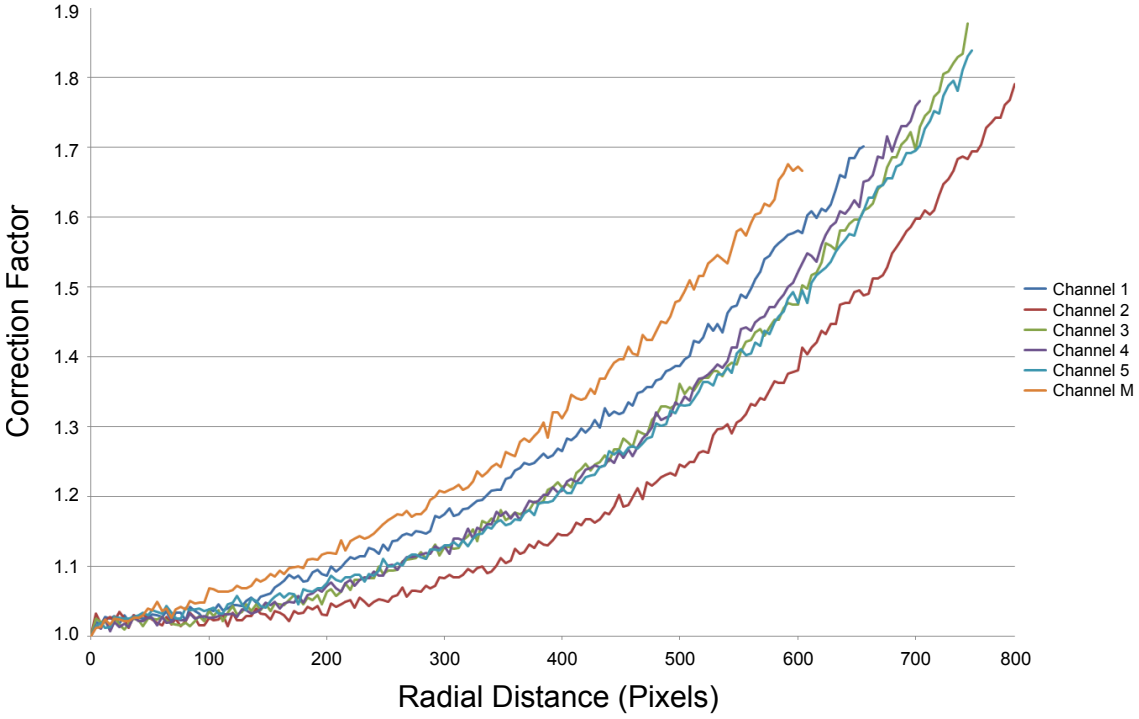

Figure 2.20: Vignetting radial falloff for all six sensors of the mini-MCA.

Effect of Exposure

Filterless LUTs were generated across a range of exposures. The LUT based approach for vignetting correction is effectively a per-pixel quantisation of the vignetting function. The degree of this quantisation is dependent upon the available dynamic range. The exposure time, therefore, ultimately determines the dynamic range of the stored flat field image. Short exposures limit the dynamic range with the subsequent quantisation generating a radial banding in the vignetting correction data (see Fig. 2.21). Radial banding represents a coarser representation of illumination radial falloff. Conversely long exposures can result in saturation washing out the vignetting function. Exposure for LUT generation was balanced between maximisation in order to minimise the effects of low dynamic range in both terms of reduced SNR and the reduced smoothness of the vignetting rate of change, while avoiding the washed out effect of excessive exposure levels.

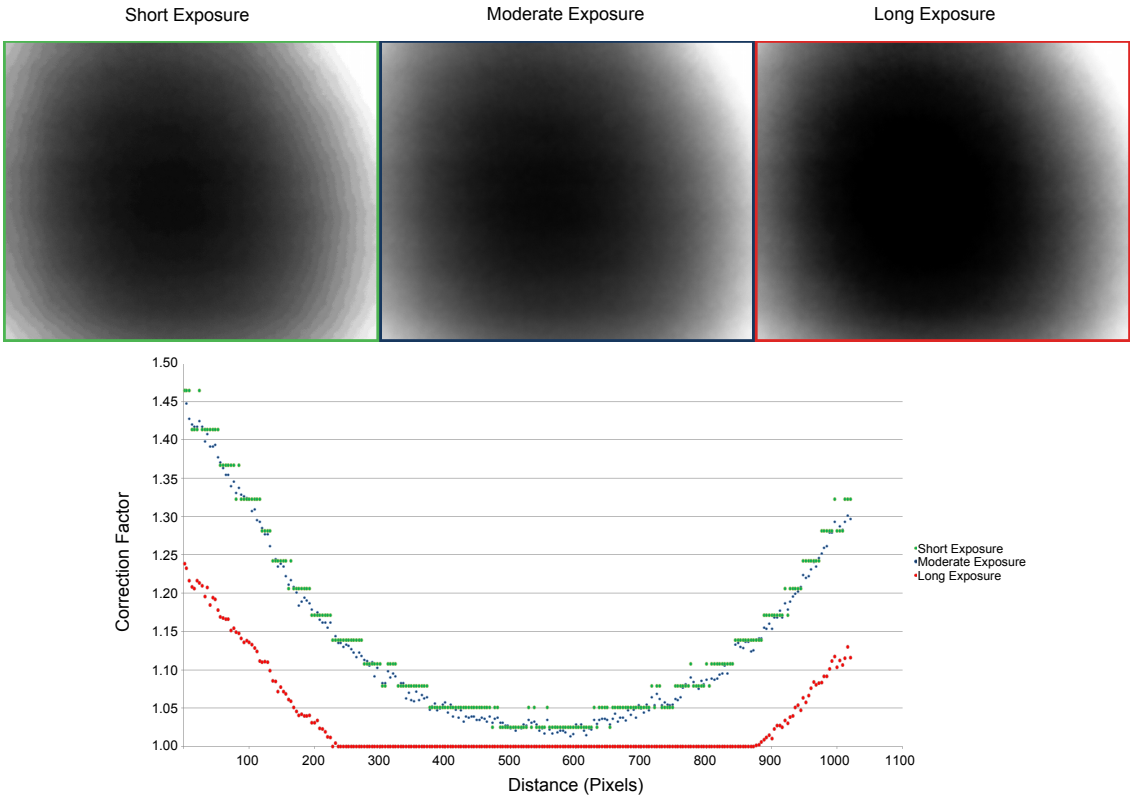

Figure 2.21: Effect of exposure on quantisation, and subsequent effect upon the vignetting radial falloff.

The reduction in radiance due to the effects of vignetting raises additional concerns. A reduction of radiance directly decreases the SNR and increases the coarseness of quantisation. This effect, however, is no longer uniformly global across an image, but radially dependent from the origin of vignetting. Consideration with the per-pixel SNR may necessitate the cropping of image edges if the combination of vignetting, filter transmission and monochromatic efficiency excessively degrade the SNR.

Effect of Filters

Filters intuitively represent a potential, additional source of mechanical vignetting. Vignetting LUTs were generated from select combinations of filters and channels. The combinations were selected based on a noise minimisation across the entire sensor. A com-

parison of the vignetting radial falloff reveals the effect of mounted filters. The increase in occlusion at wider angles introduced by the filter requires a corresponding increase in correction values (see Fig. 2.22).

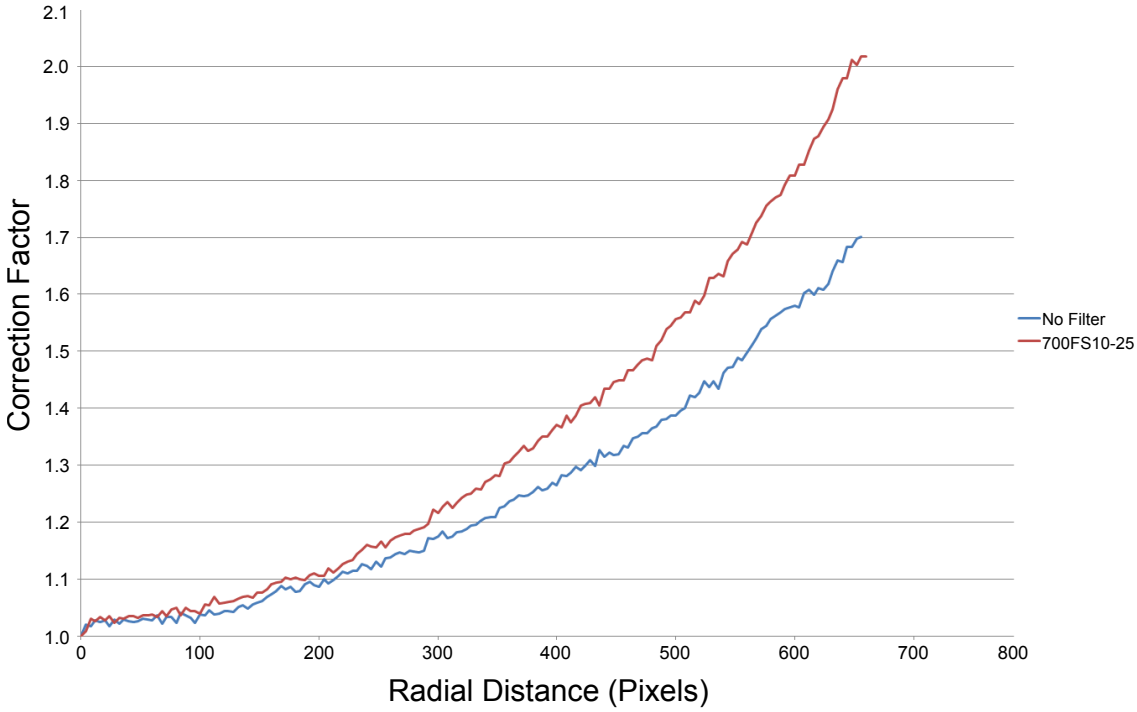

Figure 2.22: Comparison of the rate of vignetting radial falloff in the presence/absence of a filter.

Vignetting LUTs and test field data were generated from a select combination of filter and sensor. Vignetting LUTs, generated with and without filters, were applied to the test field data (see Fig. 2.23). The application of filter generated LUTs provides a noticeable improvement in vignetting correction over filterless LUTs.

2.4.5 Lens Distortion

The AgiSoft Lens software package was used to calculate the distortion principal point, radial and tangential coefficients from a calibration pattern for each of the mini-MCA channels (see Table 2.5). Radial distortion was limited to just two coefficients as calculation of a third substantially inflates the margin of error. The AgiSoft package applies the

(a) UAS false colour, no vignetting correction (b) UAS false colour, filterless vignetting correction (c) UAS false colour, filter specific vignetting correction

Figure 2.23: Application of vignetting correction : Original uncorrected image, application of filterless LUTs, application of Filter LUTs. Note increasing homogeneity of road and grass with decreasing effect of vignetting.

Brown–Conrady lens distortion model, implementing both radial and tangential distortion coefficients.

Table 2.5: Lens Distortion Coefficients.

Channel	**cx**	**cy**	**k1**	**k2**	**p1**	**p2**	**Fx**	**Fy**
1	629.169	465.738	-0.068745	0.0623006	-0.000639335	-0.000509879	1622.5	1622.5
2	628.961	464.003	-0.0579649	0.0356426	-0.000102067	-0.00221439	1606.81	1606.81
3	632.575	472.777	-0.0506697	0.021484	0.000077687	0.0011317	1625.74	1625.74
4	633.999	470.756	-0.0912427	0.132531	-0.000135051	0.00124068	1623.55	1623.55
5	632.498	470.568	-0.0748613	0.0729301	0.000851022	-0.000399902	1625.88	1625.88
M	638.965	460.592	-0.0922108	0.124107	0.000614466	0.000842289	1619.26	1619.26

The Brown–Conrady model, using the calculated correction coefficients (Table 2.5), was applied to individual mini-MCA images. All lenses within the mini-MCA exhibit pincushion distortion (see Fig. 2.24). The degree of lens distortion varies between sensors, with channel 5 exhibiting the strongest distortion while channel M exhibited the weakest. Lens distortion correction was applied to mini-MCA data.

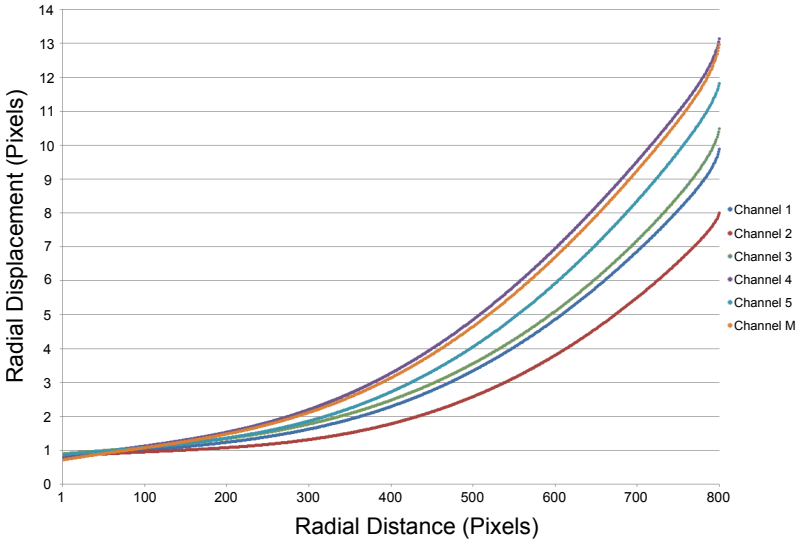

Figure 2.24: Radial distortion of all six channels within the mini-MCA.

2.4.6 Saltmarsh Case Study

ENVI[6] was used to convert the raw mini-MCA data into 10 bit uncorrected image bands. Corresponding image bands were identified and stacked to generate uncorrected six band multispectral data. A single six band multispectral saltmarsh image was selected to demonstrate the effects of sensor correction. Image bands were co-registered within ENVI using an rotate-scale-transform (RST) transformation. Co-registration was performed to aid in visualisation of the sensor corrections by reducing aberrations generated by differing IFOV of the sensor channels. Uncorrected true and false colour composite data are shown in Figure 2.25.

Dark offset subtraction was used to reduce the effects of noise within the data. Figure 2.26 provides an illustrative comparison of dark offset subtraction between high and low efficiency filters (750 and 490 nm respectively). Attention is drawn to the horizontal band noise strongly evident within the low efficiency filter, but masked within the high efficiency. The low efficiency filter also illustrates the limited capacity of dark offset subtraction for noise reduction.

[6]http://www.exelisvis.com/

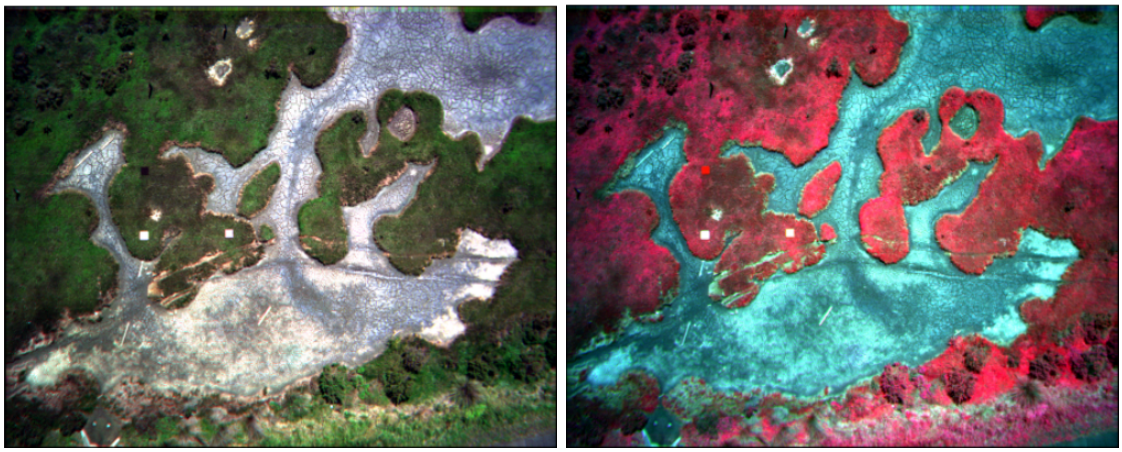

(a) Uncorrected false colour image. (b) Uncorrected false colour image.

Figure 2.25: Uncorrected true and false colour composite mini-MCA data. Note the disparity in vegetation luminosity between central and edge portions of the data generated by the effects of vignetting.

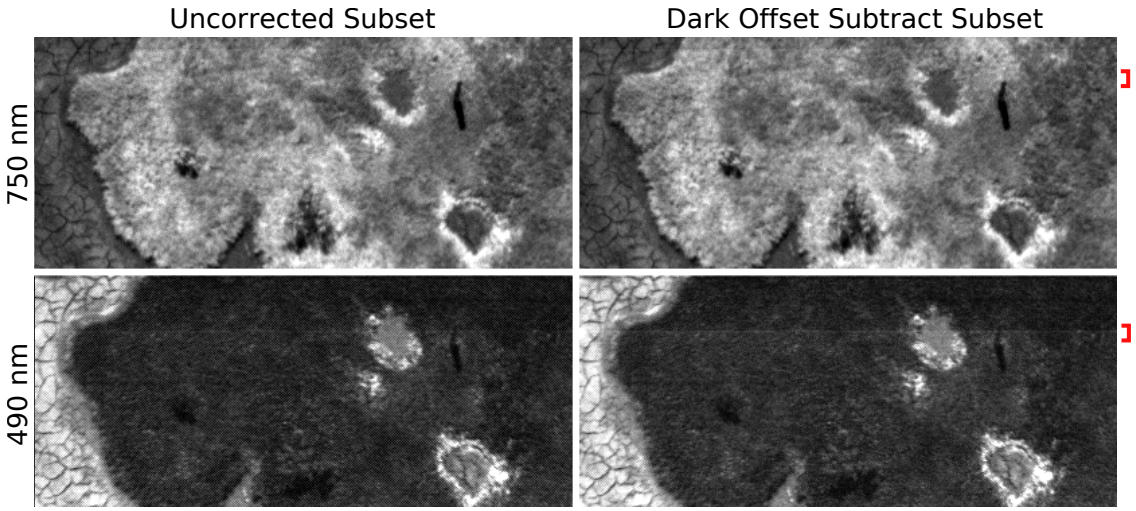

Figure 2.26: Comparative dark offset performance between high and low efficiency filters. Of particular note is the effect of dark offset subtraction upon the rolling shutter noise (evident as a thin horizontal band) between high and low efficiency filters.

Flat field derived LUTs were used to reduce the effects of vignetting within the saltmarsh data. Figure 2.27 provides an illustrative comparison for vignetting correction. The correction demonstrates noticeable visual improvement to vegetative measurements at the periphery of the data, illustrating the capacity for LUTs to reduce the vignetting

effect.

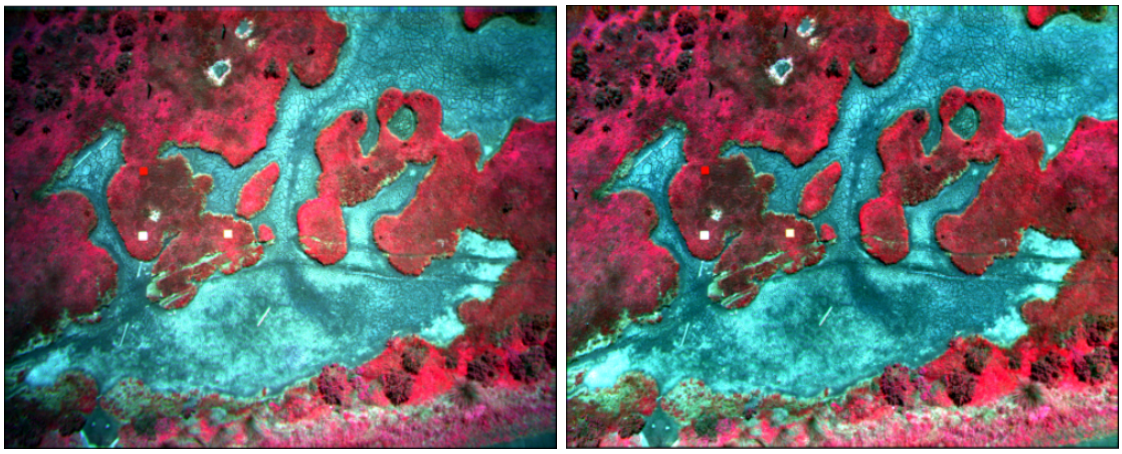

(a) Vignetting uncorrected. (b) Vignetting reduced.

Figure 2.27: Vignetting correction of false colour composite image. Of note is the restoration of luminosity between vegetation located within the centre and the edge of the image.

The effect of lens distortion correction is demonstrated by an illustrative comparison of the performance of band alignment (see Fig. 2.28). The six mini-MCA channels all exhibit different degrees of lens distortion (see Fig. 2.24). As the difference in distortion increases between sensor channels, it results in corresponding increase in band misalignment towards the periphery of data. Improving the geometric properties of the data through lens distortion correction improves the capacity for band alignment.

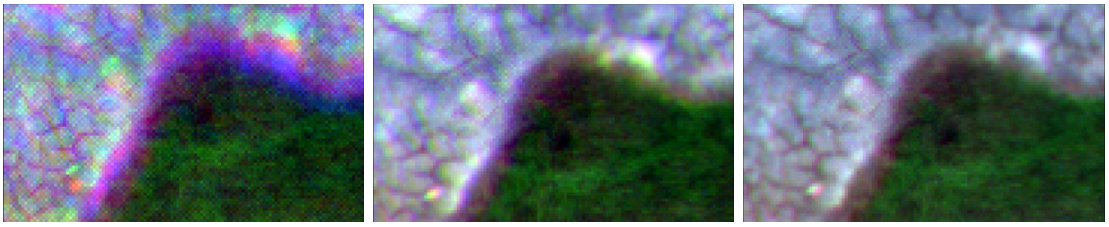

(a) No band alignment and no lens distortion correction.

(b) Band alignment and no lens distortion correction.

(c) Band alignment and lens distortion correction.

Figure 2.28: Comparative band alignment illustrating subtle improvement due to lens distortion correction. Coarse band misalignment results in a subtle purple hue along the sharp transition between vegetation and saltmarsh. With band alignment and no lens distortion correction, this hue is greatly reduced but remains subtly present. Only when both band alignment and lens distortion corrections are applied is purple misalign hue absent.

Figure 2.29 provides a final illustrative comparison, for both true and false colour imagery, of the combined effect of implemented sensor corrections.

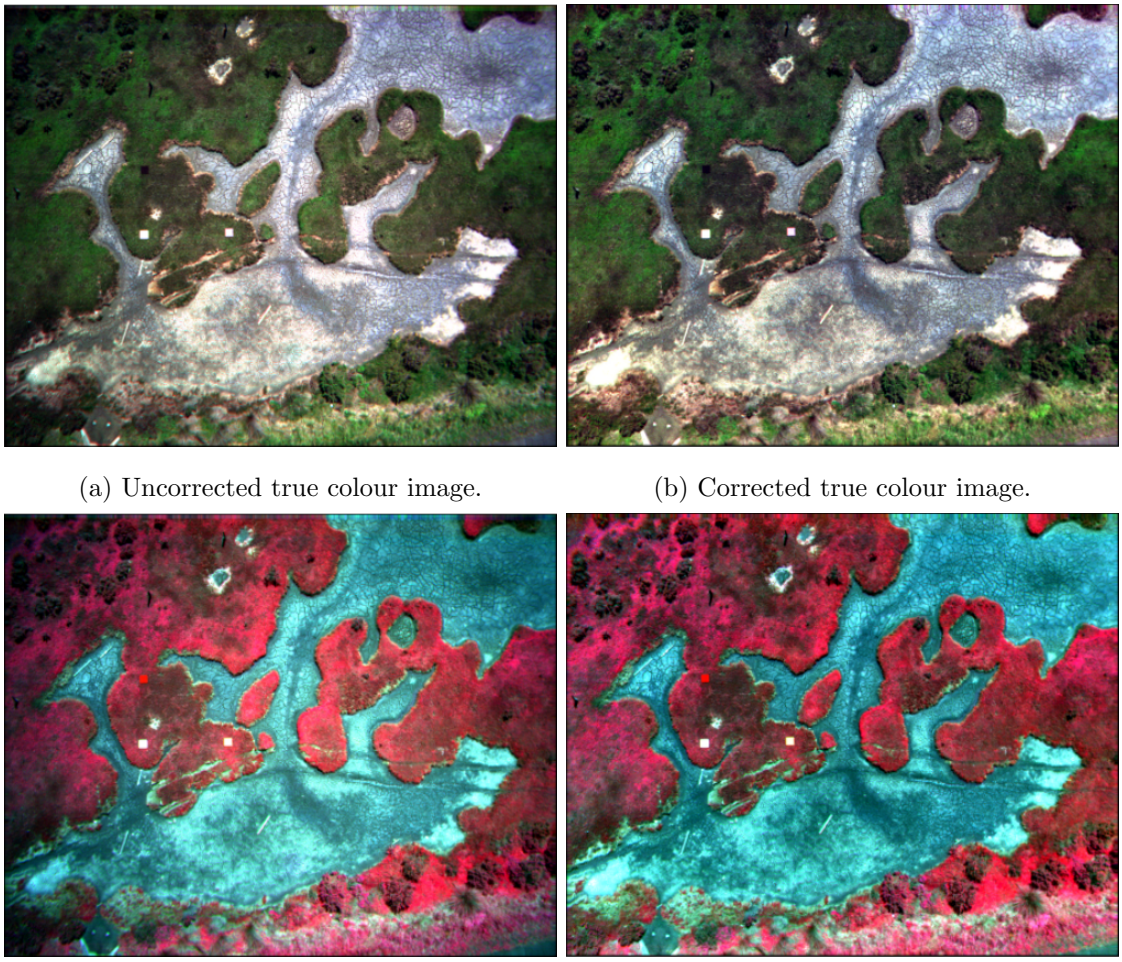

(a) Uncorrected true colour image.

(b) Corrected true colour image.

(c) Uncorrected false colour image.

(d) Corrected false colour image.

Figure 2.29: Comparative true and false colour composites before and after sensor corrections.

2.5 Discussion

The phase of sensor correction serves dual roles in raw data post-processing. It is an essential preliminary phase in the overall goal of extracting at-surface reflectance information from raw data. It also provides, however, the opportunity to investigate and assess data characteristics of a sensor. Such an investigation provides a practical insight into the limitations of a sensor system and the identification of potential flow-on effects of sensor idiosyncrasies.

2.5.1 Channel Dual Distributions

It is arguable that the dual distributions effect exhibited by channels of the mini-MCA represents the strongest compromise of data quality. The exact origin of this alternating gains observed within this study remains uncertain. Regardless of its origins, the fundamental problem is the additional uncertainty generated by two distinct, yet alternating, data distributions within a single image (see Fig. 2.13). Surfaces with similar spectral properties will exhibit dual distributions, adding strong uncertainty over the suitability of analyses based solely upon uncorrected DN values.

It is important to stress that the role of sensor correction is the extraction of DN values. Given the consistent difference between the two alternating sensor gain states, it becomes arguable that both states represent different, but nonetheless valid DN measurements. The stable variation exhibited between states is characteristic of recording differences that arise between different sensors.

The simplest approach for correcting this condition would be the adoption of some form of spatial averaging to reduce the differences between alternating pixels. A second option would be to adopt a dual radiometric correction/calibration approach. Although the primary role of radiometric calibration is to generate consistency between datasets, it may be forced to assume a greater role by generating consistency within datasets. As each state behaves like an individual channel, they may be treated individually during the application of radiometric calibration techniques. Calibrating for each state individually may reduce this checkered effect and improve consistency across an image.

The fundamental problem with this second approach, however, is that it is reliant upon the stable pattern of alternating distributions. Geometric corrections, particularly image mosaicking, modify the spatial properties of an image which may result in the loss of the stable alternating distributions of pixels. Therefore the application of dual radiometric calibration must be applied prior to any geometric corrections to an image.

2.5.2 Vignetting Model

The vignetting effect within this study was modelled through an image based flat field approach. Maximisation of the dynamic range allowed for a more smoother estimate of the per pixel falloff. An extension to this approach is the calculation of both the vignetting origin point and its rate of radial illumination falloff from the flat field, allowing for the calculation of a a smooth function (Lelong, 2008). This function describes the reduction in radiance striking the detector. The conversion of this radiance to a digital form, however, imparts a quantisation effect which is dependent upon the overall illumination within the scene. Such an effect becomes relevant when combinations of filters with contrasting efficiency are used, resulting in different quantisation levels. Strong quantisation may render the application of a smooth function for vignetting correction unsuitable.

2.5.3 Sensor Dynamic Range

UAS studies are particularly sensitive to variability in dynamic range. A major advantage of the UAS platform is the ultra-fine spatial resolution data that it can acquire. Past perspectives considered that increases in resolution would result in a corresponding increase in feature identification. This was found not to be the case, however, as the increased resolving power of finer spatial resolutions resulted in an increase in fine-scale spatial variability, thus leading to the development of more advanced image analysis techniques, including texture modelling and geospatial object-based image analysis (Puissant et al., 2005). It is therefore important for UAS mounted sensors to have the necessary level of dynamic range to capture the fine-scale spatial variability inherent of ultra-fine spatial resolution data.

2.5.4 UAS Sensor Selection

All sensors exhibit some variability in quantum efficiency across their spectrally sensitive range, in part with production quality. More expensive remote sensing platforms may opt for several individual sensors targeting specific portions of the wavelengths. Low-cost sensors, however, are inevitably forced to make concessions in production quality. The mini-MCA clearly demonstrates a flexible approach in the use of bandpass filters to select specific wavelengths. Such a flexible approach, however, requires that sensors maintain an adequate response across a wide range of wavelengths to accommodate multiple scientific purposes. Maintaining high levels of responsiveness across a wide spectral range is both technically difficult and prohibitively expensive. The resulting high variation in efficiency highlights the interplay of low-cost, flexibility, and data quality of sensor characteristics.

2.6 Conclusions

The mini-MCA is a low-cost, lightweight 6-channel multispectral sensor suitable for UAS remote sensing platforms. Sensor correction techniques were applied to illustrate their dual role in data quality improvement and analysis of sensor characteristics. The adoption of techniques covering noise reduction, filter transmission and relative monochromatic efficiency compensation, vignetting and lens distortion correction allowed for both improved image quality and the extraction of DN measurements. The process of sensor correction allowed for the identification of a number of issues with data collected by the mini-MCA: firstly the alternating gain states within a channel that result in dual noise distributions across an image, and secondly the high variability in relative monochromatic efficiency, with its associated effects upon SNR and quantisation. The dual gain states will require the implementation of careful post-processing techniques to generate consistency within data. The option to set each individual mini-MCA channel's own unique exposure would allow for a match between integration times and filter wavelength to help offset the

reduction in radiance, thereby improving both SNR and quantisation level.

Sensor correction is only the first phase of post processing. DN and at-sensor radiance measurements are both limited in their applicability due to the lack of consistency with other datasets. Radiometric calibration improves consistency between datasets by reducing temporally and spatially variable environmental effects and transforming at-sensor radiance to a more universal at-surface reflectance measurement scale. Further spatial transformations include map registration, image band co-registration, and image mosaicking. Georeferencing and mosaicking is a particular important step in the creation of seamless multispectral mosaics from a large number of UAS data (Laliberte et al., 2011b). The sensor correction techniques proposed in this study should improve the results of these spatial transformation techniques due to an improved radiometric response across the individual images in a UAS survey.

Encouraged by the increased accessibility of UAS as a remote sensing platform, small-scale in-house UAS programs will become a more commonly adopted approach for scientific endeavours. The development of these small-scale programs, however, will require a broad skillset capable of addressing all facets of UAS platform development, data post-processing, and image analysis. The adoption of low-cost UAS platforms requires the development of improved post-processing techniques in order to generate robust quantitative studies. Ultimately, the development of UAS programs necessitates a balance between accessibility (both from a technical skills and cost standpoint) with application flexibility and data quality.

Acknowledgements

We would like to acknowledge the Winifred Violet Scott Trust and the Australian Antarctic Division for financially supporting this project. We thank Darren Turner for his technical input and UAS piloting skills in the field. Finally, we would like to thank Steven de

Jong for his comments on an earlier version of this manuscript.

Thesis Context

High quality data are essential for any quantitative spatial analysis. This chapter successfully demonstrates a preprocessing framework that improves data quality for the Tetracam Mini-MCA 6-band multispectral sensor. The effects of sensor noise, vignetting and lens distortion were quantified, and an automated framework was developed to correct raw Mini-MCA data. The following two chapters incorporate this automated correction framework in the construction of Mini-MCA multispectral spatial dataset.

Chapter 3

An Image Texture Modelling Framework for Ultra-Fine Spatial Resolution UAS Data

The focus of Chapter 3 is upon the development of a texture modelling framework that analyses and identifies relevant class-specific texture metrics. The Chapter is the first stage of a broader framework for the spatial generalisation of UAS ultra-fine spatial resolution data to a suitable class-specific analysis scale.

3.1 Abstract

The ultra-fine resolution sampling scale of unmanned aircraft systems (UAS) generates data with high spatial variability. Analysis of UAS data requires spatial generalisation to reduce data complexity, and extract meaningful information. Image texture modelling is one approach to spatial generalisation. Its optimal application however, is undermined by the vast number of texture models, metrics and analysis scales. This paper presents a machine-learning framework for the identification of texture metrics for image classification. This framework relies upon class spatial subsets to rapidly generate texture metrics.

A random forest framework is then used to compare and identify suitable class-specific texture metrics for the classification of UAS saltmarsh data. A total of 693 texture metrics were tested for seven groundcover classes. A total of 20 metrics were identified and incorporated into a geospatial object-based image analysis (GEOBIA). Texture metrics were found to improve both the overall GEOBIA classification accuracy (17.23% improvement) of the saltmarsh study site, as well as class-specific accuracy. The demonstrated framework is rapid, robust and flexible, and is widely adaptable to various remote sensing classification contexts and image texture models.

3.2 Introduction

3.2.1 Unmanned Aircraft Systems

Unmanned aircraft systems (UAS) are gaining popularity within the remote sensing community. The capacity for researchers to tailor UAS to fit their specific research niche creates new opportunities for scientific research (Chao et al., 2008). Furthermore, UAS are capable of acquiring spatial data at ultra-fine resolution (<10 cm) (Dunford et al., 2009), and occupy a sampling scale unavailable with manned aircraft or satellite remote sensing platforms. Despite these benefits however, UAS present several challenges. The detail of UAS ultra-fine resolution data may over-complicate data by introducing excessive spatial and spectral variation (Puissant et al., 2005; Agüera et al., 2008).

3.2.2 UAS Image Analysis

Ultra-fine spatial resolution is a defining characteristic of UAS data and is the result of its low observational altitude. Relative to an image feature under observation, this low observational altitude determines the complexity and content of spatial measurements. The lower the altitude of UAS, the finer the spatial scale of data (Dunford et al., 2009). As the sampling scale becomes finer, the spectral generalisation of coarse mixed pixels within

an image feature is reduced (Lechner, 2012; Blaschke, 2010; Cracknell, 1998), revealing fine-scale spatial detail (see Fig. 3.1). As fine-scale detail further increases, feature components may become spatially separable, thereby giving rise to distinct spectral properties (Maillard, 2003). For closely related image features, feature components may be shared (e.g. wood among plant species). This overlap in spectral characteristics may significantly reduce the accuracy of image classification.

(a) Satellite image (2 m) (b) Aerial image (60 cm) (c) UAS image (1 cm)

Figure 3.1: Comparative imagery illustrating the change in resolving power of different operational heights. The effects of mixed pixels is steadily reduced between satellite data, aerial photography and UAS data. High resolving power of UAS data reveals vegetation structural details lost to the mixed pixel effect in the coarser sample scale images.

Image classification relies upon definitions to assign an image feature to a thematic class. Definitions are traditionally built from the spectral characteristics of discrete pixels. Classification confusion is introduced when definitions overlap, which may result in misclassification (Congalton, 1991). The high spatial complexity of UAS data may result in significant overlap of these pixel-based definitions, and is therefore unsuitable for traditional discrete pixel-based classification (Yuan and Bauer, 2006). In response, techniques have been developed to move spatial analysis away from discrete pixels towards broader spatial generalisations (Myint et al., 2011). Two commonly adopted approaches are geospatial object-based image analysis (GEOBIA) and image texture.

3.2.3 Geospatial Object-based Image Analysis

GEOBIA shifts the focus of spatial analysis from discrete pixels to image objects (Blaschke, 2010; Powers et al., 2012). Image segmentation is used to deconstruct an image into objects. Image objects are constructed by grouping together neighbouring pixels that exhibit similar spectral properties (Stuckens et al., 2000). A homogeneity threshold is used to control the degree of pixel similarity within an object. Relaxing this threshold leads to greater intra-object spectral variability, and subsequently larger image objects.

GEOBIA extends beyond discrete pixel analyses by providing spatial generalisation and object geometric properties (Duro et al., 2012). Objects can be used to statistically generalise the pixel data they contain. Furthermore, geometric properties may be extracted based upon an object's shape and size. The spatial analysis of image object neighbour relationships can reveal wider landscape patterns. GEOBIA has been successful utilised in a number of environmental studies (Lechner, 2012; Jones et al., 2011; Powers et al., 2012).

3.2.4 Texture

Texture is an important spatial factor of image interpretation (Herold et al., 2003). Digital image texture research has established a range of texture models that quantify local image texture into a metric. Texture models operate by defining a local neighbourhood centred around each pixel. Modifying the size this neighbourhood allows the exploration of texture at different scales of analysis. A metric is derived from a statistical analysis of this neighbourhood (Puissant et al., 2005).

It is argued that texture is an abstract concept that lacks a clear, precise definition (Maillard, 2003). This lack of clarity has resulted in a range of texture definitions. To illustrate this point, Hay et al. (1996) argues that texture can be defined by two characteristics: a rotationally variant spatial structure and a rotationally invariant measure of contrast.

Conversely, Zhu et al. (2010) presents a no-less valid argument that texture can be represented by a structural continuum, which ranges between an absolute geometric and an absolute stochastic structure. The choice of definition provides the foundation for how a texture model quantifies local tonal variation into a metric. The lack of a single definition has resulted in numerous models to quantify image texture.

The dominant characteristic of an image feature class falls within a gradient between homogeneous tone and texture (i.e. the absence to the total dominance of spatial structure) (Tuttle and Jensen, 2006). Furthermore, the dominant characteristic may be dependent upon the scale of phenomena (see Fig. 3.2). Identifying the dominant characteristic appropriate to both the feature class and scale of phenomena is fundamental to the success of image texture modelling. This paper adopts Woodcock and Strahler (1987) definition of texture as the replications, symmetries and patterns within tonal structure occurring within an image at different analysis and sampling scales.

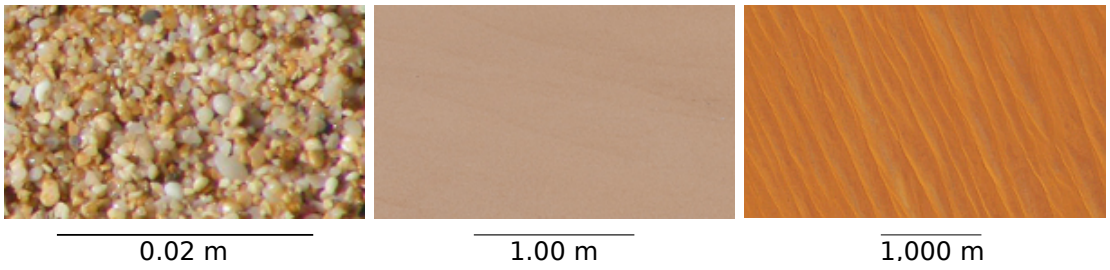

(a) Stochastic sand grains (b) Homogeneous sand (c) Geometric sand dunes

Figure 3.2: Illustration of the effects of phenomena scale on the dominate visual characteristic of sand image feature class: Fine phenomena-scale reveals the stochastic tonal structure of individual grains, a medium scale results in homogeneous sand free of tonal structure, and broad phenomena-scale reveals the geometric tonal structure of sand dunes.

3.2.5 Quantification of Image Texture

Numerous texture models have been explored within remote sensing. Tuttle and Jensen (2006) successfully employed 1st and 2nd order image texture models in distinguishing texture differences between nesting sites of two closely related bird species. Local binary

patterns were used by Shinde and Shrivastava (2012) in a multiscale approach to first separate agricultural crop cover from other land cover types, followed by a species-level classification. Discrete wavelet decomposition, a signal processing technique, was found by Chen (2007) to provide a slight improvement over spectral values alone in the separation of classes with low and high homogeneity. Marmol (2011) implemented Gabor filters, a technique typically used for edge detection, as a texture model to successfully delineate vegetation and structures from both imagery and LiDAR data. Dorigo et al. (2012) explored the use of a 2^{nd} order image texture model for the classification of an invasive weed species.

Despite demonstrating the value of texture, the reasoning behind selecting a specific model and metric for a particular application remains ambiguous. A robust selection of image texture is confounded by a number of complex factors which include: the absence of an *a priori* method to identify image texture; generating and comparing the statistical measures and analysis scales of available texture metrics across the vast range of texture models; the dependence of texture upon sample scale (see Fig. 3.2); feature class definition and separability; and improvements in classification accuracy even with an arbitrary selection of texture metrics. The successful application of texture models and metrics is explored in past studies.

Texture metric selection for image classification requires identifying the minimum number of metrics that generate the maximum performance. Given the vast number of texture models and their metrics (including image bands, statistical measures and neighbourhood sizes), a comparison of potential metrics based upon classification accuracy is prohibitive due to computational demands. What is required is a focused, rapid framework for the identification of relevant texture models and metrics. Central to such a framework are feature variable selection techniques, which allows for comparison and identification of optimal texture metrics.

3.2.6 Feature Variable Selection

Feature variable selection is a phase in predictive model construction. Feature variable selection aims to construct the most parsimonious model by identifying and selecting only the most relevant variables. This process serves three primary tasks: dataset reduction, the identification and ranking of relevant variables, and improving model prediction (Genuer et al., 2010; Guyon and Elisseeff, 2003; Laliberte et al., 2012). Feature variable selection improves model prediction when there are a large number of potential predictor variables. The Hughes phenomenon (Laliberte et al., 2012), also known as the curse of dimensionality (Duro et al., 2012), is a reduction in statistical confidence that occurs when there is a low number of training samples used to construct a model relative to a high number of predictor variables. Feature variable selection reduces the number of variables by identifying and removing those of least influence on a model's predictive power. Reducing the number of variables improves processing times and reduces the effect of the Hughes phenomenon on the model's statistical confidence (Cheng et al., 2006).

3.2.7 Remote Sensing Texture Feature Selection

Texture models can generate metrics with a range of different statistical data types, which include both numerical and categorical. Furthermore, the statistical properties of spatial data rarely exhibits a predictable distribution. To fit these qualities, the technique of remote sensing feature selection is required to be both non-parametric and capable of directly comparing a range of statistical data types. Decision trees are a non-parametric approach to classification that are capable of handling dimensionally large, complex datasets of differing data types (Friedl and Brodley, 1997; Pal and Mather, 2003; Safavian and Landgrebe, 1991)

3.2.8 Random Forest

Random forest (RF) is an ensemble machine learning technique introduced by Breiman (2001). A RF model is comprised of numerous, individual decision trees. Each tree is constructed using bootstrap aggregation, whereby only a random subset of variables are used. For each tree, a proportion of samples are randomly chosen for tree construction while the remaining samples are used for cross-validation. As a part of cross-validation, random forest can assess the relative importance of a variable to the models predictive accuracy. Therefore a RF model constructed from texture metrics calculated using different models, can be used to compare and estimate the relative importance of each specific texture metrics overall and on a class definition basis.

RF modelling was quickly adopted within the remote sensing community for feature selection and classification. Duro et al. (2012) used a combination of RF modelling and expert knowledge to select a number of environmental variables, including a texture metric, for object-based classification across an agricultural region. Stumpf and Kerle (2011) utilised RF for variable selection of a number of object landscape metrics for the classification of four landslide areas. Chan and Paelinckx (2008) included RF as part of a study evaluating two ensemble classifiers, utilising aspects of feature selection to identify hyperspectral band ranges relevant for vegetation classification. Rodriguez-Galiano et al. (2012) compared RF with a traditional single decision tree classifier, in addition to testing RF model sensitivity to forest size, number of variables and noise simulated within the data. Dorigo et al. (2012) used RF models to identify the most suitable texture metrics for identifying an invasive weed in multi-temporal aerial photography.

One noted issue with random forest is that variable importance has a bias towards correlated predictor variables. As the importance of variables is tested on an individual basis, derived lists of variable importance can be dominated by highly correlated variables (Strobl et al., 2008). Additional filtering is therefore required to reduce the number

of correlated variables, and clearly identify a minimal number of texture metrics that still maintain high predictive power.

3.2.9 Paper Aims

The primary aim of this study is to present a rapid framework for the comparison and selection of suitable class specific texture metrics for ultra-fine spatial resolution UAS multispectral data. The presented framework is flexible towards different texture models and may be further embedded within a GEOBIA workflow to enhance both thematic accuracy of image classification. The frameworks flexibility is illustrated using four common models for the calculation of texture: a 1st order kernel-based texture model, a 2nd order grey level co-occurrence matrix (GLCM), a categorical local binary patterns operator (LBP), and the discrete wavelet transformation.

3.3 Methods

3.3.1 Study site

The site selected for this study is a remnant patch of cold temperate saltmarsh vegetation at Ralphs Bay in Tasmania, Australia (see Fig. 3.3; Table 2.2). Ralphs Bay consists of 40 km of sheltered coastline within the Derwent estuary. The restricted inlet into the bay partially protects the shoreline from strong wave action, resulting in the formation of intertidal sand flats and pockets of established saltmarsh vegetation. The saltmarshes of Ralphs Bay are of noted ecological importance as habitat for the endangered Spotted Handfish as well as a feeding and nesting site for migratory birds (Prahalad, 2010).

Figure 3.3: Study site QuickBird image: Ralphs bay, Racecourse flats saltmarsh (42°55′43.50”S, 147°29′2.50”E)

Saltmarshes have been historically viewed as a threat to public health, with the muddy, stagnant, decaying organic conditions blamed as a source of disease. Wholesale clearing of saltmarsh vegetation was encouraged during reclamation efforts, to both reduce the risk of disease and reclaim prime fertile lands (Adam, 2002). Rising environmental awareness has shifted this viewpoint to acknowledge ecological values and a growing need to conserve the remaining habitat (Laegdsgaard, 2006).

Central to any conservation effort is high quality spatial data to accurately map current habitat, monitor changes in the environment and to assess the application of management techniques (Goetz, 2006). Reclamation efforts have reduced and fragmented the spatial extents of saltmarsh communities to small areas (Adam, 2002). Mapping these smaller areas requires the ultra-fine resolution spatial data that UAS can provide.

Vegetation distribution within saltmarshes is strongly restricted by environmental conditions. Topographic exposure to frequent tidal inundation and salt water spray results in a strong environmental gradient. This results in the fine-scale zonation of species distribution, leading to sharp species transitional boundaries and greater spatial homogeneity.

The level of detail of ultra-fine spatial resolution UAS data are required to generate to map this species-level zonation.

Data of the study site was collected using a MikroKopter Oktokopter UAS (see Chapter 2). Battery life for a single Oktokopter UAS flight is approximately 15 minutes, allowing for a two hectare area to be covered in a single flight. The UAS was mounted with the Tetracam miniature multiple-camera-array (mini-MCA) allowing for the generation of six-band multispectral data. Data was collected at 490, 530, 570, 670, 700 and 750 nm (full width at half maximum (FWHM) of 10 nm) to generate traditional true and false colour composites, as well as vegetation indices (Kelcey and Lucieer, 2012).

Field sampling was conducted across the site, with detailed groundcover characteristics recorded for over 50 points. The location of each point was recorded using a differential dual-frequency RTK Leica GPS receiver (positional accuracy of 2 - 5 cm). Each sample point consisted of a visual groundcover assessment, a geolocated terrestrial digital photograph and a spectral signature generated with an ASD HandHeld2 spectrometer.

3.3.2 UAS Data Pre-processing

The raw image data was pre-processed using a sensor correction methodology developed for the mini-MCA using IDL script (Kelcey and Lucieer, 2012). Mini-MCA data was corrected for errors generated by sensor noise, alternating gains, vignetting, and lens distortion. Individual image bands were aligned and a georeferenced orthomosaic was generated using the Agisoft Photoscan Professional[1] software package.

The georeferenced orthomosaic was radiometrically calibrated to reflectance using spectral targets. Three spectral targets were distributed within the study site. These targets represented low, mid and high ranges of spectral reflectance. The spectral reflectance of each target was recorded using an ASD HandHeld2 spectrometer. An empirical line calibration was used to transform the image digital numbers to spectral reflectance. Two

[1] http://www.agisoft.ru/

vegetation indices were derived from the calibrated orthomosaic: the normalised difference vegetation index (see equation 3.1) and the red-edge normalised difference vegetation index (see equation 3.2) Viña et al. (2011); Sims and Gamon (2002).

$$NDVI = \frac{750 - 670}{750 + 670} \qquad (3.1) \qquad\qquad RENDVI = \frac{750 - 700}{750 + 700} \qquad (3.2)$$

3.3.3 Saltmarsh Groundcover Class Definition

A study site assessment revealed seven fine scale groundcover classes divided between two broader scale definitions of vegetated and non-vegetated. Four plants were represented within the vegetated areas: a sedge *Gahnia filum*, a herbeaceous groundcover *Samolus repens*, a succulent groundcover *Sarcocornis sp.* (consisting of *Sarcocornia blackiana* and *Sarcocornia quinqueflora*) and a succulent shrub *Tecticornia arbuscula*. Areas absent of vegetation included intertidal sand flats, inundated mudflats, and saltpans.

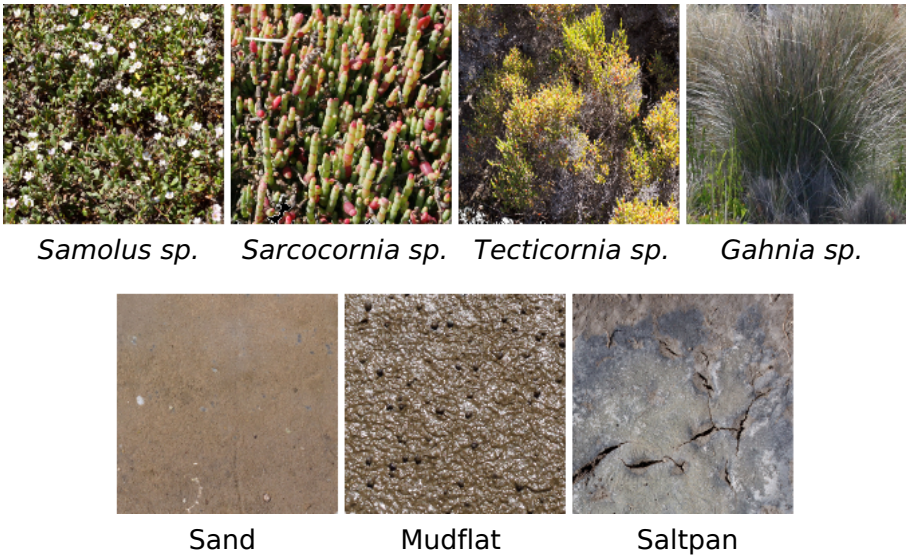

Figure 3.4: The seven groundcover classes. The vegetation classes (L-R): *Samolus sp.*, *Sarcocornia sp.*, *Tecticornia sp.*, *Gahnia sp.*. The non-vegetation classes (L-R): Sand, Mudflat, Saltpan

3.3.4 Texture Analysis

A texture analysis framework was constructed to identify and extract class-specific texture metrics (see Fig.3.5) The calculation of texture models and metrics across the spatial and spectral extents of the image is computationally time consuming. Therefore in order to maximise the number of texture metrics investigated, a smaller image subset was extracted and used. For each groundcover class, three homogeneous areas were identified. From these areas, a 60 x 60 pixel subset (9 m^2) was extracted and a representative groundcover class mosaic was constructed. Four texture models were applied to this mosaic: first order kernel, the grey-level co-occurrence matrix, the local binary pattern operator, and the discrete wavelet transformation.

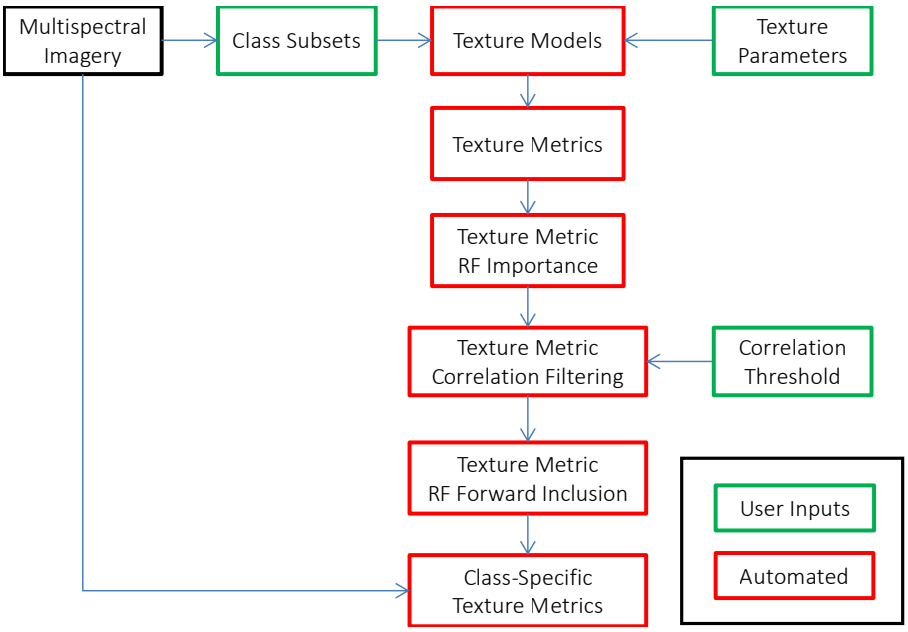

Figure 3.5: Workflow for the identification and extraction class specific texture metrics.

First Order Kernel Model

The first order texture analysis was the simplest of the four models (see Fig.3.6). First order texture metrics use the statistical properties of pixel values within a local neighbourhood to represent tonal structure (Tuttle and Jensen, 2006). Texture metrics were

calculated from a square kernel that is moved across the image. Statistical properties were calculated from the pixels within the kernel and were assigned to the location of the centre pixel. Altering the size of the kernel modified the analysis scale of the metrics. First order texture metrics were calculated using the mean, standard deviation, variance and kurtosis. Analysis scales were explored using kernel sizes between 3 and 15 pixels. Metrics were calculated for all spectral and indice bands.

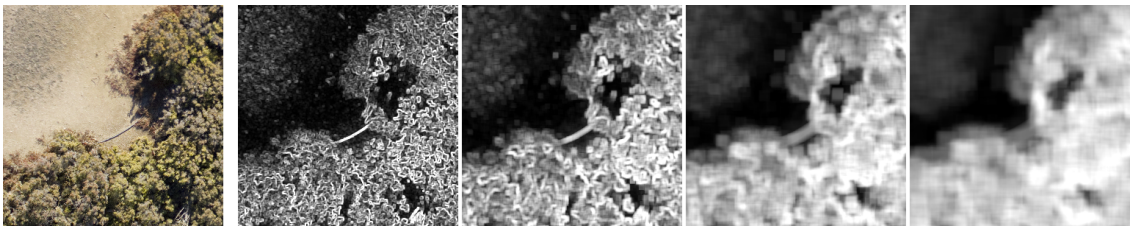

Figure 3.6: Illustration of the first order texture metric 'standard deviation', generated from four different square kernel sizes (pixel length): 3, 9, 15, and 25.

Grey Level Co-Occurrence Matrix Model

The grey level co-occurrence measure (GLCM) is a second order texture model that also utilises a moving kernel (see Fig.3.7). Second order texture metrics expand upon first order metrics by including the spatial orientation and direction of tonal structure (Tuttle and Jensen, 2006). The GLCM initially calculates a frequency matrix of the co-occurrence of pixel pairs at a spatial offset (Haralick, 1973). Statistical properties of this matrix were derived to quantify tonal structure. The GLCM texture metrics explored in this study were mean, variance, homogeneity, contrast, angular second moment, entropy and correlation. GLCM spatial scales are explored using kernel sizes ranging between 3 and 15. Metrics were calculated for all spectral and indice bands.

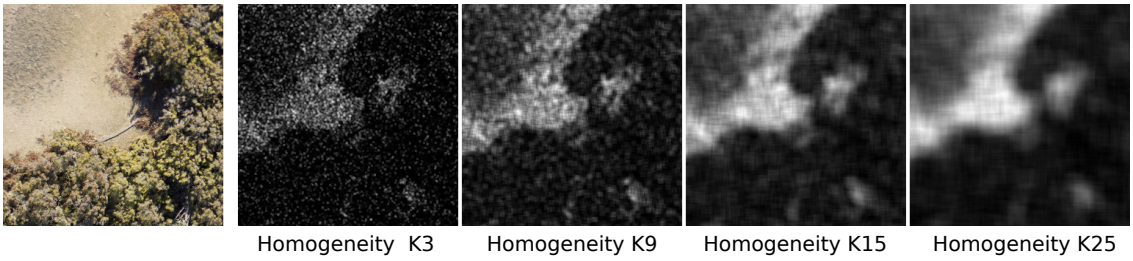

Figure 3.7: Illustration of the GLCM texture metric 'homogeneity', generated from four different square kernel sizes (pixel length): 3, 9, 15, and 25.

Local Binary Patterns Operator Model

The local binary pattern (LBP) model generates a ranked integer texture metric (see Fig.3.8). Integer rankings were calculated from the micropatterns generated by the concatenation of a circular binary gradient around each pixel (Zhao and Pietikainen, 2007; Ojala and Pietikäinen, 1999). The LBP incorporates a user-defined number of points evenly spaced on a circle at a user-defined radius from the centre pixel. A threshold function applied to these points with respect to the centre pixel, returns a binary representation for the central point. The concatenation of these binary numbers generates a ranked integer label. Rotational invariance of LBP is achieved by calculation and application of a pre-generated look-up-table (Guo et al., 2010). LBP metrics were explored using radial points ranging between 5 and 8 at radii ranging from 2 to 5. Metrics were calculated for all spectral and indice bands.

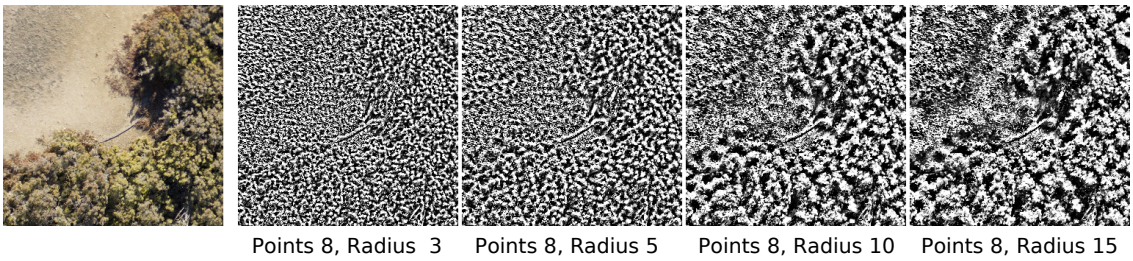

Figure 3.8: Illustration of the local binary pattern texture metric, generated using 8 points at four different radii: 3, 5, 10, and 15.

Discrete Wavelet Transformation Model

The wavelet transform is a signal decomposition technique (see Fig.3.9). Image data were treated as a 2D signal and was decomposed with respect to a mother wavelet. To be decomposed using a wavelet, an image must have square 2^n spatial dimensions. The initial pass decomposes the image into both high-pass and low-pass information (Carvalho et al., 2001). Successive decomposition is performed upon the resultant low-pass information, while the high-pass information is retained. This results in the generation of high-pass information at successively coarser analysis scales (Chen et al., 2007). The retained high-pass images provided an insight into how energy is distributed in terms of both scale and space within the image. Wavelet decomposition was implemented using a moving kernel of spatial sizes ranging between 5 and 15 pixels. Cubic interpolation was used to pad out the spatial dimensions of kernels in order to fit the 2^n requirement. The energy metric was derived using a Haar mother wavelet (Chen et al., 2007; Wu et al., 2005).

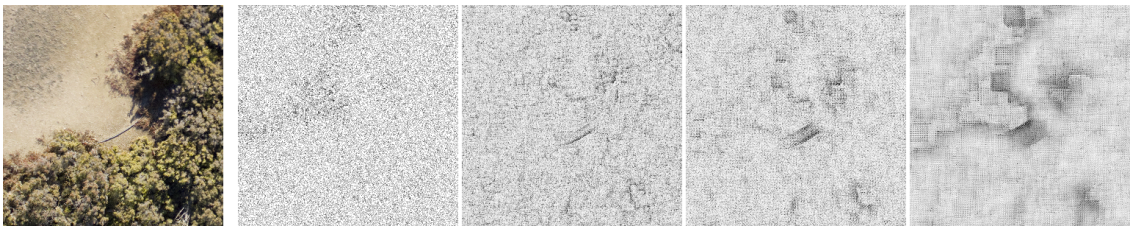

Figure 3.9: Illustration of the wavelet energy texture metric, generated from four different square kernel sizes (pixel length): 5, 9, 15, and 25

3.3.5 Class Texture Calculation and Random Forest Analysis

RF models were trained based on the test mosaic image. The RF model was used to assess the relative importance of individual texture metrics and to identify an accurate classifier for object classification. As a part cross-validation, RF can assess the relative importance of a texture metric to the model. Importance was measured by substituting a metric within the cross-validation set with a random permutation. This random value

substitution has the effect of mimicking the metrics absence from the model (Strobl et al., 2008). The change in cross-validation accuracy provides a relative measure of the metrics importance.

RF was implemented using the R statistical package randomForest[2]. RF requires two settings: the number of decision trees, and the number of random variables used to determine the binary split at each individual node. The number of decision trees was set at 4,000 while the variable number to use at each node followed the convention of using the square root of the total number of available variables (Shi and Horvath, 2006; Svetnik et al., 2003; Granitto et al., 2007).

Texture was assessed using a RF model generated using all available texture models and metrics. Class specific importance of individual texture metrics were calculated from the RF model and subsequently sorted in order of descending importance. To address RF bias towards correlated variables, we implemented a forward inclusion, class-by-class analysis to select only the most important, least correlated texture metrics. Texture metrics were iteratively assessed in order of descending importance. Correlation of a texture metric was calculated against all texture metrics of greater importance. Texture metrics were retained only if the correlation remained beneath a defined threshold of 0.7.

The last step of texture selection is to identify the minimum number of texture metrics required for optimal classification. This was achieved through a forward inclusion approach using RF. RF models were iteratively generated, adding successive texture metrics to the model based upon their importance. The change in per-class out-of-bag (OOB) error rate was recorded. An optimal classification is achieved once the OOB error is either reduced to zero, or converges with additional texture metrics. Texture metrics were calculated for the entire image based upon optimal class-specific texture lists.

[2]http://cran.r-project.org/web/packages/randomForest/index.html

3.3.6 Texture Metric GEOBIA Performance

The performance of selected texture metrics was explored using GEOBIA. Image data was segmented using the eCognition software package. The 'scale' level of the multi-resolution segmentation was set to 50. Training objects were selected based upon the field sampling. Image objects were classified first using only spectral properties and then spectral with texture metrics.

In situations where there are a large number of thematic classes, there exists the potential generation of a large number of texture metrics. An excessive number of metrics may introduce the Hughes phenomenon. Therefore, the classification approach taken generates class-specific RF models, limiting the number of variables in any given model. Class-specific probabilities for each object were calculated by the respective RF model.

3.4 Results

3.4.1 UAS Data Construction

A 5 cm spatial resolution orthomosaic of UAS multispectral data was generated of a 200 x 100 m stretch of saltmarsh vegetation at Ralphs Bay (see Fig.3.10). Spatial accuracy of the georecitification was measured at 0.15 m using 23 ground control points (see Table 3.1) and an empirical line calibration was applied to transform image DN-values to reflectance (see Table 3.2). Sensor malfunction within the 490 nm channel resulted in severe oversaturation and poor calibration results. The 490 nm band was excluded from further analysis, thereby limiting the selection of vegetation indices to the normalised difference vegetation index (NDVI) and the red-edge normalised difference vegetation index (RE-NDVI).

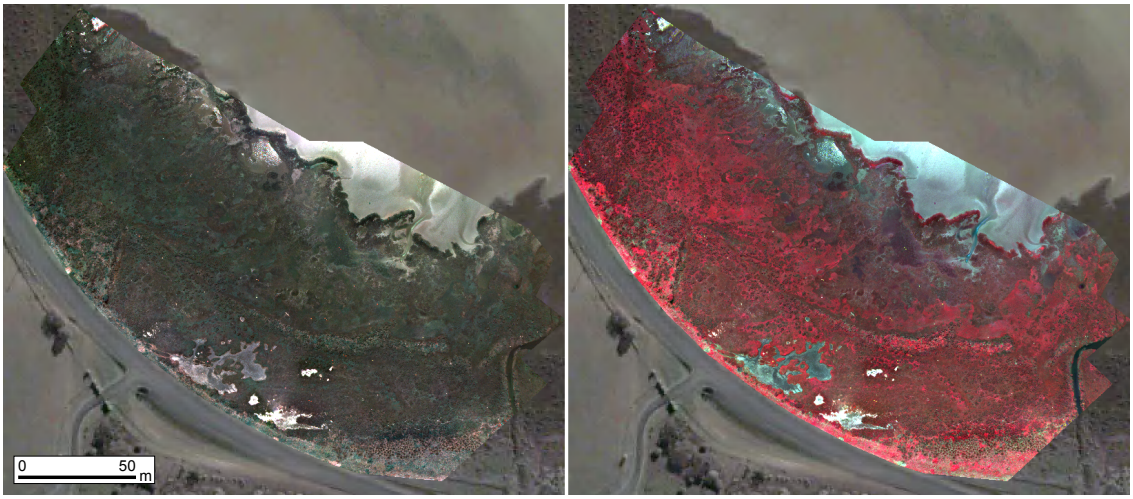

Figure 3.10: QuickBird image of the saltmarsh study site overlaid with both UAS generated RGB and false colour orthophotos.

Table 3.1: Image Acquisition Details and Construction Accuracy

Site	Date	UAS Images	GCPs	Samples	Bands	Spatial Res.	RMSE
Ralphs Bay	25/11/2011	149	23	53	6	0.05 m	0.15 m

Table 3.2: Sensor Calibration Results

Wavelength (nm)	490	530	570	670	700	750
EL Calibration (r^2)	0.514	0.989	0.971	0.983	0.956	0.835

3.4.2 Class Mosaic

Figure 3.11 illustrates the seven groundcover classes from a terrestrial and UAS perspective, as well as the mean spectral response and associated standard deviation. Notable is the higher spectral variation, and by extension tonal structure, exhibited by three of the vegetation classes: *Sarcocornia sp.*, *Tecticornia sp.*, and *Gahnia sp.*. *Samolus sp.* and

the non-vegetation classes all exhibit lower spectral variation. In addition, a higher than expected mean and variation of NIR reflectance exhibited by the non-vegetation classes is arguably attributable to the higher radiometric calibration error within the 750 nm spectral band (see Table 3.1).

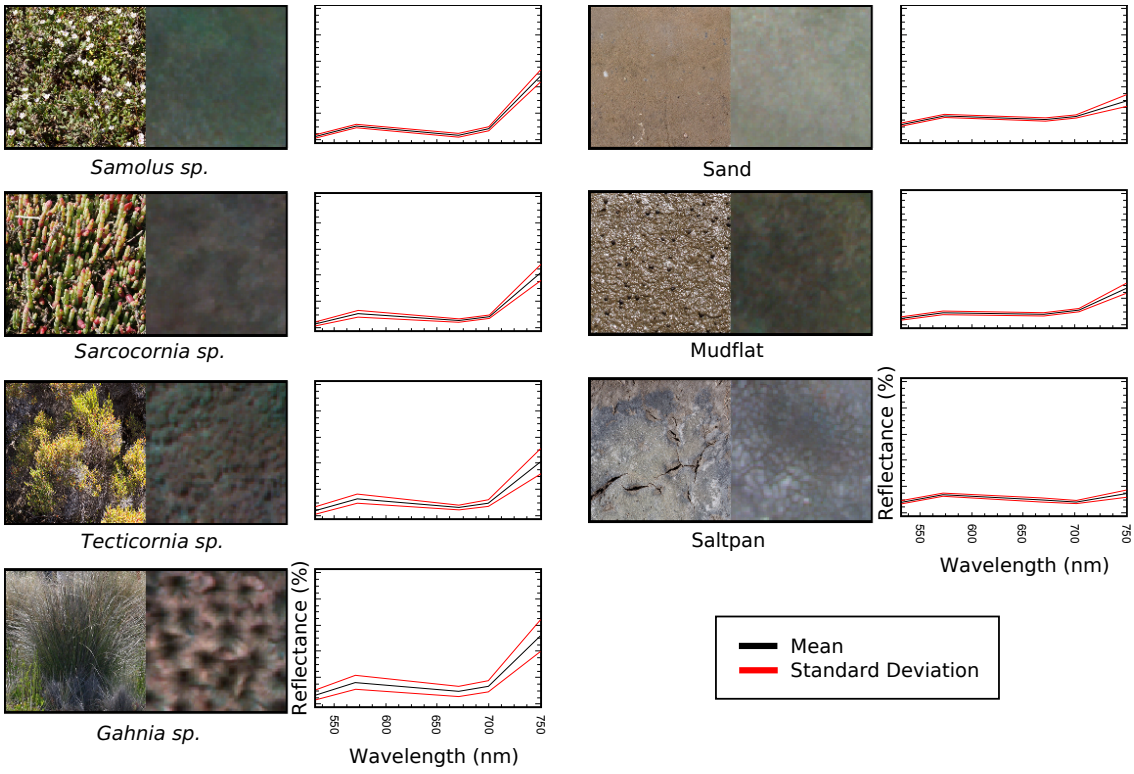

Figure 3.11: Groundcover class comparison: Terrestrial photo, UAS-derived data and calibrated spectral profile.

3.4.3 Object-Based Spectral Classification

The entire saltmarsh study site was classified using GEOBIA. The saltmarsh image was segmented into image objects. A RF model was constructed using the spectral attributes of training objects, and was then used to classify the remaining objects (see Fig. 3.12). An accuracy assessment of the classification is presented in Table 3.3. Misclassification occured predominately within the broader vegetation and non-vegetation classes, with the exception of confusion between mudflats and *Gahnia sp.*. Of the vegetation classes, only *Samolus sp.* achieved satisfactory results. Confusion was strongest between *Sarcocornia*

sp. and *Tecticornia sp.*.

Table 3.3: Full image GEOBIA classification confusion matrix generated utilising object spectral properties only (%).

Class	*Samolus*	*Sarcocornia*	*Tecticornia*	*Gahnia*	Sand	Mudflats	Saltpan
Samolus	87.3	5.11	10.11	19.78	0	0	0
Sarcocornia	5.06	53.39	18.79	8.87	0	7.88	0
Tecticornia	7.54	33.93	68.68	10.27	0	0.84	0
Gahnia	0.1	0.56	0.1	48.14	0.27	15.95	1.66
Sand	0	0	0	10.56	95.92	8.76	31.43
Mudflats	0	7	2.32	0.19	0	58.41	5.15
Saltpan	0	0	0	2.2	3.81	8.16	61.76

Overall Accuracy 67.66

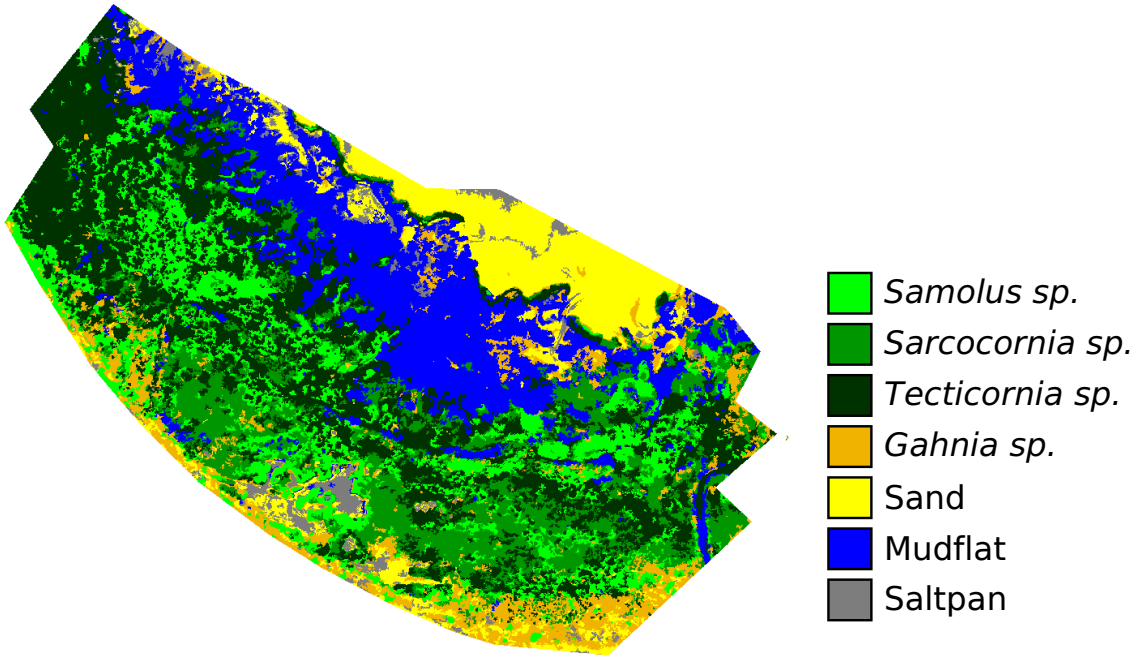

Figure 3.12: Saltmarsh object-based classification (spectral data only).

3.4.4 Texture metric Selection

All texture metrics from the four texture models were generated for each class tile of the representative mosaic. A RF model was generated from these texture metrics, and the relative importance of each metric was calculated for both the overall model and on a class-by-class basis. Figure 3.13 presents a simplified graph of the overall importance measures, providing a broad overview of the overall performance of the four texture models. The graph illustrates the high importance of both first order and GLCM texture models relative to the LBP operator and wavelet energy. In addition, for first order, GLCM and LBP models, increasing kernel size generally improves importance irrespective of the metric.

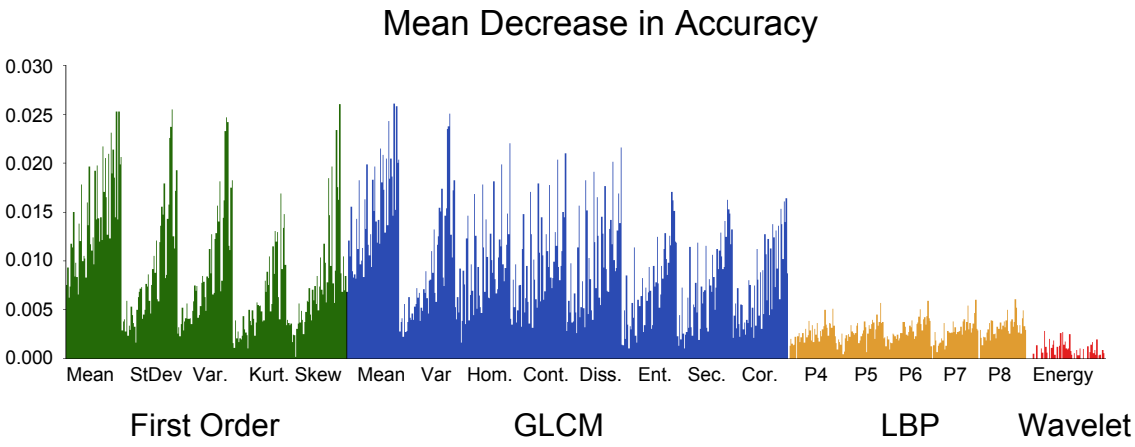

Figure 3.13: Simplified graph illustrating the relative overall importance of different texture methods to provide a qualitative comparison of the overall performance of texture models. Increasing spatial generalisation through neighbourhood size (kernel or radius) increases the relative importance of any given metric (with the exclusion of wavelet).

For each class, a list of texture metrics was sorted in descending order of importance and filtered with a correlation threshold of 0.7. Forward inclusion of texture metrics proceeded until an optimal OOB class error was identified. Figure 3.14 illustrates the reduction in class specific OOB error rate with additional texture metrics. Classes of higher spectral variability (*Sarcocornia sp.*, *Tecticornia sp.*, and *Gahnia sp.*) all required

at least 4 additional texture metrics to reduce the class error to below 1% (OOB error of 0.01). Classes with low spectral variability (Sand, Mudflats and Saltpan) required only a single texture metric. *Samolus sp.* required two additional texture metrics.

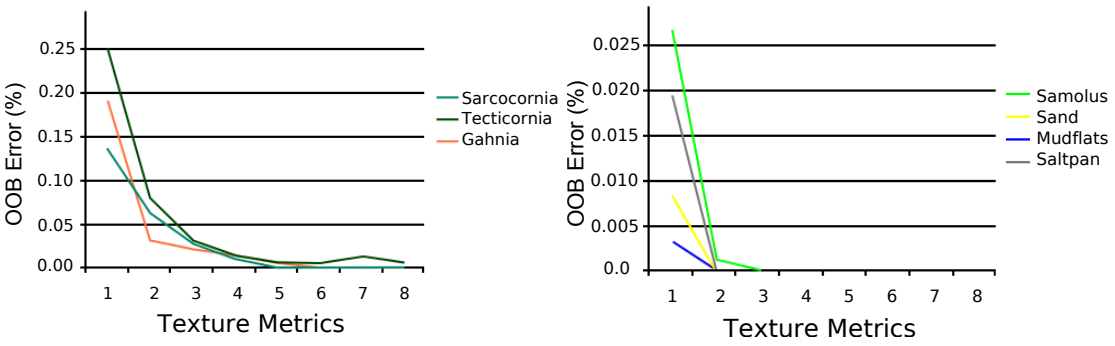

(a) Change in OOB error of *Sarcocornia sp.*, *Tecticornia sp.*, and *Gahnia sp.*.

(b) Change in OOB error of *Samolus sp.*, Sand, Mudflats and Saltpan.

Figure 3.14: Graph illustrating the change in class-specific OOB error rate with additional texture metrics.

The final class-specific texture metric selection is presented in Table 3.4. The most frequently selected texture model was the first order kernel, followed by the GLCM. The high performance of first order and GLCM metrics resulted in the exclusion of both wavelet-based and LBP metrics. The texture of NIR bands and vegetation indices were most frequently utilised. Repetitions of texture metrics between classes provided insight into characteristics responsible for separating those classes. The GLCM Mean of the RE-NDVI spectral index was listed as the most important texture metric for mudflats, sand and saltpan, and therefore clearly represents a major feature of texture for class separation within the broader non-vegetation classes. In contrast the vegetation classes exhibited a wide range of first order and GLCM texture metrics.

Table 3.4: List of the final determination of class-specific texture metrics.

Samolus sp.	*Sarcocornia sp.*	*Tecticornia sp.*	*Gahnia sp.*
FO: NDVI Mean K15	FO: 750 Mean K15	GLCM: 670 Mean K15	FO: 670 Mean K15
GLCM : 750 Mean K15	GLCM: RE-NDVI Dis K15	FO: 700 Skew K15	FO: NDVI Mean K13
	GLCM: RE-NDVI Hom K15	FO: 530 Kurt K15	FO: 700 Skew K15
	GLCM: 700 Ent K15	GLCM: NDVI Cor K15	FO: 750 Mean K15
	GLCM: 700 Cor K15	FO: 700 Kurt K15	GLCM: RE-NDVI Hom K15

Sand	Mudflats	SaltPan
FO: RE-NDVI Mean K13	FO: RE-NDVI Mean K13	FO: RE-NDVI Mean K13

3.4.5 Final Classification

RF models were generated upon a class-by-class basis incorporating the class-specific texture metrics. Class probability for each object was calculated from the respective class-specific RF. Objects were classified based upon the highest class probability (see Fig. 3.15).

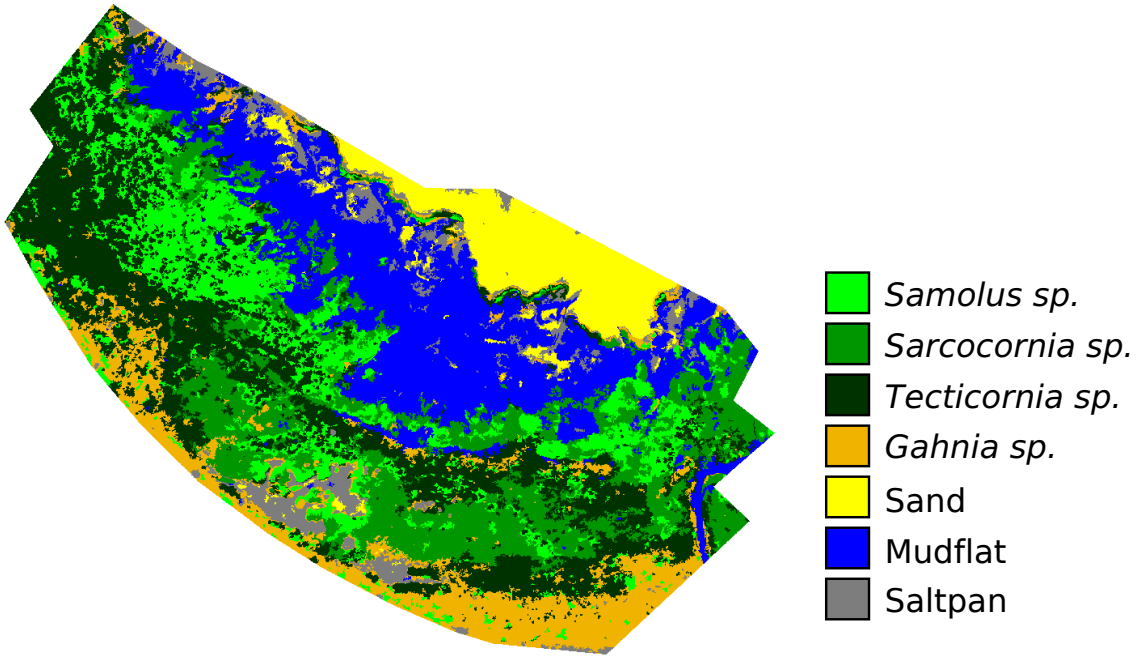

Figure 3.15: Saltmarsh object-based classification (spectral and texture data).

The error matrix of the texture-based classification is presented in Table 3.5. All classes show an improvement in classification rate, and with the single exception of *Sarcocornia sp.* and mudflats, all remaining misclassifications between the broader vegetation and non-vegetation groups are eliminated. The greatest gains in classification accuracy are made within the spectrally variable vegetation classes, namely *Tecticornia sp.* and *Gahnia sp.*. Improvement of classification accuracy in *Sarcocornia sp.* is reduced by strong increased misclassification with mudflats. Misclassification within the non-vegetation group persists between mudflats and saltpan.

Table 3.5: Full image GEOBIA classification confusion matrix generated utilising both object spectral and texture properties (%).

Class	*Samolus*	*Sarcocornia*	*Tecticornia*	*Gahnia*	Sand	Mudflats	SaltPan
Samolus	98.44	6.61	0.95	9.56	0	0	0
Sarcocornia	1.45	73.57	1.25	0	0	0	0
Tecticornia	0.01	1.01	97.24	15.14	0	0	0
Gahnia	0.1	0.32	0.56	75.3	0	0	0
Sand	0	0	0	0	98.39	4.68	21.58
Mudflats	0	18.49	0	0	0	76.21	3.33
Saltpan	0	0	0	0	1.61	19.11	75.10

Overall Accuracy 84.89

3.5 Discussion

3.5.1 Role of Texture and GEOBIA

The results of this study illustrate that texture metrics and GEOBIA are mutually beneficial approaches for the analysis of ultra-fine spatial resolution UAS data. We established that the inclusion of texture metrics into GEOBIA improved classification accuracy over spectral-based GEOBIA (see Tables and). Misclassifications are evident between mudflats and *Sarcocornia sp.* (see Table 3.5). These errors occur within an environmental gradient between the two classes (see Fig.3.16). The changes in tidal inundation create this gradient whereby areas closer to the shoreline experience longer periods of salt-water inundation. *Sarcocornia sp.* is gradually excluded along this gradient as it becomes unable to cope with longer periods of inundation. This in turn results in a gradual exposure of the underlying mudflats. In the absence of texture metrics, these mixed areas are being regularly misclassified as *Tecticornia sp.* (see Table 3.3).

Figure 3.16: Illustration of the gradient between *Sarcocornia sp.* and mudflats. Variable periods of saltwater inundation result in a gradual thinning of *Sarcocornia sp.*.

3.5.2 Random Forest Texture Selection

The RF classifier provides a rapid and robust texture selection framework. The processing time of this framework is dependent upon both the total number of texture metrics and the number of thematic classes. Starting with a representative training mosaic is key for achieving rapid execution of this proposed framework. The study, however, implements no preliminary analyses that may further reduce this dataset, instead opting for inclusion of a wide range of texture models, kernel sizes, and metrics. Variable selection studies have illustrated the value of implementing expert knowledge to provide an initial reduction in the volume of variables. This is, however, typically done when using less abstract phenomena, such as environmental or topographic variables. Given both the abstract nature of texture and its high sensitivity to sample scale and classification context, expert knowledge on texture may be limited to very broad intuition of class-specific dominant tonal or spectral band characteristics. Herold et al. (2003) illustrates this expert knowledge approach by limiting GLCM measures to the near-infrared band for vegetation while Dorigo et al. (2012), when faced with highly correlated image bands, selected only the band of highest entropy for texture analysis.

The RF training mosaic is created from homogeneous, representative image sections of each class. This therefore excludes the confusion of fuzzy gradients experienced between

mudflats and *Sarcocornia sp.*. It can therefore be expected that class separability within this texture training dataset is greater than that for the whole image. Despite this limitation, the training mosaic may provide some first insight into class separability. The results of the mosaic illustrate some difficulty in class separability within the broader vegetation and non-vegetation groups. This provides the first hint that the more heterogeneous vegetation classes would benefit from additional texture metrics.

The goal of a texture model is to spatially generalise image tonal structure. It therefore follows that the more spectrally homogeneous a class is (i.e. the less tonal structure), the less benefit texture metrics will have. This concept is illustrated in the change of accuracy of *Samolus sp.* and the three non-vegetation groundcover classes. Figure 3.11 illustrates the lack of spectral variability of these four classes, with the noted exception of the 750 nm band. In this case, the texture selection framework has selected for mean texture metrics used to smooth out tonal variation rather than quantifying its structure. An examination of the texture metrics selected by the RF reveals that all layers for these four classes, either directly or indirectly, utilise the 750 nm band (see Table 3.4). Furthermore, the non-vegetation classes all select the same first order mean measure of the RE-NDVI band. The reduced calibration success of the 750 nm band may be a contributing factor for the additional variation it exhibits. These texture metrics may therefore be more of a response to miscalibration rather than any actual tonal structure.

Further potential exists in reducing processing time of this framework by focusing upon two aspects: i) assessment of the need for texture on a class-by-class basis, and ii) the spectral input bands from which to derive texture metrics. Maillard (2003) highlights that the value of texture lies in its capacity to spatially generalise image tonal structure. There remains a need for a framework to quantitatively identify both the dominant tonal structure within a class (homogeneous or texture) and its separability with other classes, before committing processing time to identifying a suitable texture metric for entire images.

3.5.3 Texture Selection Framework Comparison

Past literature has explored the development of texture analysis frameworks. Ella and van den Bergh (2008) presented a similar framework to this study, in that representative tiles extracted from a larger dataset are used to compare the performance of nine different texture models. The overall accuracy of support vector machine classification was used to assess the performance of a texture model. Maillard (2003) assesses the performance of three texture models for the pixel-based separation of highly different textures, with a direct comparison to an overall classification task as well as assessing a models capability to separate classes of varying similarity.

The dimensionality of a texture metric dataset is a limiting factor in the approach of these studies. Given the wide availability of texture models and metrics, a comprehensive analysis of texture can significantly expand the dimensionality of data. Coupled with a texture selection framework that limits the analysis to a reduced subset, a texture analysis may achieve a condition known as the 'large p, small n' problem. The 'large p, small n' problem occurs when the number of parameters (i.e. texture metrics) in a dataset exceeds the number of samples (Loh, 2012). This is known to undermine the assessment of variable importance using traditional regression or decision tree analyses (Kitchen, 2011).

We believe that our framework advances the selection of texture within the context of remote sensing studies. The random forest model has been demonstrated as robust against high dimensionality data, thereby maintaining classification performance even under conditions of 'large p, small n' (Strobl et al., 2007; Loh, 2012). Random forest is an appropriate model for the selection of texture metrics given its reduced vulnerability to high dimensional data, and is therefore capable of accurately processing a large array of texture metrics. Our framework builds upon past remote sensing random forest implementations (Duro et al., 2012; Stumpf and Kerle, 2011; Chan and Paelinckx, 2008; Rodriguez-Galiano et al., 2012; Dorigo et al., 2012) by explicitly focusing upon texture metric selection, ex-

panding the study to include multiple models, and ensuring random forest bias is reduced through the addition of a correlation threshold. This study illustrates the capabilities of this random forest framework through the direct assessment of 693 different texture metrics derived from four texture models, and the final identification of metrics that produced practical accuracy improvements.

3.6 Conclusion

This study demonstrates a texture selection framework for identifying class-specific texture metrics. The framework utilises spatial subsets to rapidly generate metrics from four different texture models: first order kernel, the grey-level co-occurrence matrix, the local binary pattern operator, and the discrete wavelet transformation. A random forest ensemble model was used to identify class-specific texture metrics at an appropriate analysis scale. The framework tested 693 texture metrics for the classification of unmanned aerial systems (UAS) saltmarsh data. A total of 20 metrics for seven saltmarsh groundcover classes. Class-specific metrics were shown to improve the classification of ultra-fine spatial resolution UAS data, both for the overall accuracy (a 17.23% improvement) as well as for each of the seven groundcover classes.

This study further demonstrates the complementary natures of texture metrics and geospatial object-based image analysis (GEOBIA). Texture modelling and GEOBIA represent different approaches to spatial generalisation. Texture modelling in this study was incorporated into a broader GEOBIA. However, the application of GEOBIA within this study was rudimentary, with little exploration of the different available GEOBIA parameters or spatial characteristics of image objects. The next task is to explore the complementary nature of GEOBIA and texture modelling. This will require the development of a GEOBIA framework that analyses the role of object spatial characteristics, and identifies the specific role of texture modelling within GEOBIA.

Thesis Context

The UAS generates spatial data at an ultra-fine spatial resolution previously unavailable. Chapter 3 provides a texture modelling framework that utilises random forest based machine learning to identify class-specific texture metrics. It was demonstrated that the scale of analysis of these identified texture metrics improved the classification of ultra-fine spatial resolution UAS saltmarsh data. The following Chapter details the second stage of the broader spatial generalisation framework, building upon texture modelling by introducing GEOBIA.

Chapter 4

A Semi-Automated GEOBIA Framework for the Classification of Ultra-Fine Spatial Resolution UAS Data

The focus of Chapter 4 is upon the development of a GEOBIA framework that analyses and identifies relevant class-specific image segmentation parameters. The Chapter is the second stage of a broader framework for the spatial generalisation of UAS ultra-fine spatial resolution data to a suitable class-specific analysis scale.

4.1 Abstract

The sample scale of unmanned aircraft systems (UAS) results in fine scale measurements of high spatial complexity. Geospatial object-based image analysis (GEOBIA) can be used to spatially generalise information by segmenting image data into image objects. Optimal image segmentation is dependent upon the relative scale of analysis required. This paper presents a framework for the identification of class-specific GEOBIA segmentation parameters. The framework utilises digitised user subsets to test the accuracy of segmentation scales. Spatial and classification accuracy assessments are used to identify

class-specific scales of under- and over-segmentation. Optimal class-specific segmentation scales are identified using this information. Incorporating class-specific segmentation scales improved the GEOBIA classification accuracy of UAS saltmarsh data over a single scale GEOBIA (16.4%). Additional texture metrics increased both classification and spatial accuracy of GEOBIA, demonstrating the complimentary nature of texture modelling and GEOBIA for spatial generalisation. This paper improves the analysis of ultra-fine spatial resolution UAS data by providing a framework for the identification of class-specific relative analysis scales.

4.2 Introduction

4.2.1 Ultra-fine spatial resolution data

The capacity to generate ultra-fine spatial resolution data are a fundamental appeal of low-flying unmanned aerial systems (UAS). Flying at altitudes between 50 to 200 m, allows the generation of geographic data at spatial resolutions finer than 5 cm (Laliberte et al., 2011a; Lechner, 2012). The increased resolving power of UAS provides a fine sample scale that allows small image features to be distinguished. However, the fine sample scale also vastly increases the spatial complexity of image data as the structural variation within image features becomes distinguishable (Woodcock and Strahler, 1987; Blaschke, 2010). New image analysis techniques are required to adapt to the increase in UAS sample scale.

4.2.2 Scale

Features, patterns, and processes may be observed and characterised across a range of spatial scales (Marceau, 1999). The scale of sampling using remote sensing techniques, records a specific level of organisation (Marceau, 1999), and therefore determines what features, patterns, or processes can or cannot be observed (Turner et al., 1989). The appropriate sampling scale is determined by the environment and information sought,

the type of analysis needed to extract this information, and the spatial structure of the image (Woodcock and Strahler, 1987). Within a remote sensing context, sampling scale is the spatial resolution of the data. It is also important, however, to recognise the relative scale of phenomena (Benz et al., 2004). Within the context of remote sensing, there is a need to clearly distinguish between the absolute sample scale, and the appropriate scale of analysis relative to the scale of image phenomena (Marceau and Hay, 1999).

Sample Scale

Sample scale within remote sensing refers to the fixed observation characteristics of collected data. These characteristics are independent of any image feature under observation. Sample scale has two main components: grain and extent (Marceau and Hay, 1999). The grain defines the finest spatial area generalised into a single observation. This is represented by the spatial resolution of an individual pixel. Conversely the extent represents the cumulative spatial span of all detected grains, and therefore represents the spatial extents of the image.

A fundamental drawback of data sample scale is the modifiable areal unit problem (MAUP) (Wu and Qi, 2000). MAUP arises from the vast number of ways an area can be divided into non-overlapping areal units (grains), and the data variation these differences generate (Wu et al., 2002). MAUP arises from two issues known as the scale and the aggregation problem (Marceau and Hay, 1999). The MAUP scale problem represents the variation in data caused by grains that differ in shape and/or spatial extents of sampling. The MAUP aggregation problem is due to differing spatial distributions of grains, which spatially modifies the area of spatial generalisation for each pixel.

Analysis Scale

Where sample scale provides information on how image data are constructed and represented, the scale of analysis is the scale at which phenomena is observed (Marceau and

Hay, 1999; Marceau, 1999). The analysis scale is defined as the window of observation through which an analyst interprets the image, and thereby provides both a direct and relative spatial context to phenomena. Phenomena within a natural environment rarely occur at the same spatial scale. An image may therefore have numerous relative scales of analysis, each one relevant to different phenomena (Marceau, 1999; Laliberte et al., 2012).

Strahler *et al.* (1986) distinguishes two categories of analysis scale relative to the capacity of an images sample scale to resolve phenomena: H- and L- resolution. Within H-resolution imagery, the scale of phenomena exceeds the size of the image grain. This results in spatially and spectrally distinct image features. Conversely within L-resolution imagery, phenomena are smaller than the grain and has pixels with mixed spectral properties (Plaza et al., 2009). Given the variety of spatial scales of image phenomena, image data can be either described as either H- or L- resolution depending upon the resolving power.

4.2.3 Spatial Generalisation

Traditional discrete pixel-based approaches to image analysis operated at the sample scale of the image. This approach has been most successful within L-resolution imagery (Blaschke et al., 2014; Blaschke, 2010), whereby the spectral mixing homogenises the variability of features (Powers et al., 2012). In contrast, ultra-fine spatial resolution of UAS data results in predominately H-resolution data (Blaschke, 2010; Lechner, 2012). As fine-scale feature detail becomes increasingly measurable due to the scale of UAS, the internal complexity of features increases (Woodcock and Strahler, 1987; Marceau and Hay, 1999). This added complexity places considerably limitations on traditional discrete pixel-based techniques, as individual pixels lack broader geometric generalisation and contextual information (Stumpf and Kerle, 2011). To compensate for the increased scale of ultra-fine spatial resolution data, image analysis has shifted away from a pixel-based

absolute scale to the relative scale of image phenomena. This is achieved using spatial generalisation to shift the scale of the analysis.

4.2.4 GEOBIA

A recent development in spatial generalisation is the use of geospatial image object analysis (GEOBIA). The foundation of GEOBIA is the segmentation of an image into smaller, meaningful image objects. Image objects are neighbouring pixels that have been grouped together due to their similarity (Castilla and Hay, 2007; Lechner, 2012). A common approach to GEOBIA relies upon a region growing algorithm to construct non-overlapping objects (Blaschke, 2010). Region growing first identifies initial seed pixels within an image. Homogeneous image objects are then 'grown' from these seeds by iteratively merging neighbouring pixels or objects of similar spectral properties (Feizizadeh and Blaschke, 2013). The selection and weighting of suitable image bands as well as the sequence of pixel aggregation determine individual object boundaries and therefore the overall segmentation result (Blaschke, 2010; Benz et al., 2004). Modifying the object homogeneity threshold provides a degree of control of the size image objects (Duro et al., 2012), and therefore the extent of spatial generalisation. Region growing techniques have the potential to spatially generalise the absolute sample scale of data to a relative scale of analysis appropriate for image phenomena.

Image objects may not initially relate to real-world features. Instead, they provide an essential building block for additional image processing that aggregates objects into meaningful features Benz et al. (2004). Albrecht et al. (2010) distinguishes between two groups of image object boundaries: bonafide and fiat (see Fig.4.1). Bonafide boundaries are tangible delineations between image features. Conversely fiat boundaries lack a clear image border, and represent object boundaries within a feature. Image objects may represent a mixture of bonafide and fiat boundaries.

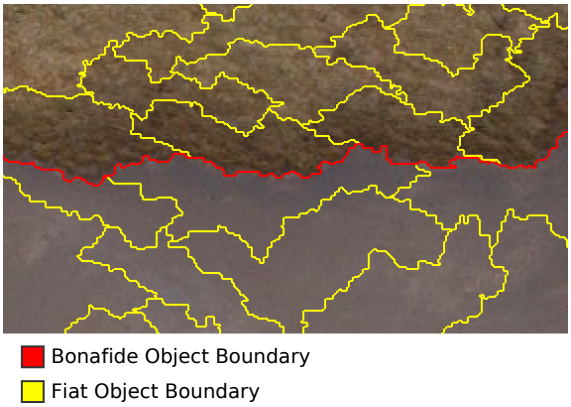

Figure 4.1: Segmentation results illustrating objects with both bonafide and/or fiat boundaries. Red bonafide boundaries are the tangible inter-object boundaries between mudflat and vegetation. Yellow fiat boundaries lack a visible border and represent intra-feature objects within either mudflat or vegetation.

The second phase of GEOBIA is the classification of objects (Aguilar et al., 2013; Benz et al., 2004). Objects classification predominately uses a mixture of image and geometric properties. Standard statistical measures, including the mean and standard deviation, are calculated from enclosed pixels. Object geometry characteristics are also used, and may include object shape, size, and relationships with neighbouring objects (Blaschke, 2010; Benz et al., 2004; Laliberte et al., 2012). As these characteristics are derived at the relative analysis scale of the segmentation, the application of GEOBIA has the potential to address limitations associated with MAUP. The capacity to segment an image at multiple scales allows for the spatial generalisation of the absolute sample scale of an image into relative scales of analysis that are meaningful to specific image phenomena.

The Segmentation Scale Issue

GEOBIA image segmentation is entirely dependent upon image structure. This results in inconsistencies when transferring segmentation parameters between different imagery, even when of similar content. This creates difficulty in predetermining segmentation parameters without some evidence of result. In earlier studies, it was common to test

an arbitrary range of segmentation parameters with the segmentation choice selected by a visual appraisal or a final accuracy assessment (Darwish et al., 2003). However, such approaches are time-consuming and too broad to take into consideration the relative scale of class features. A conceptual and practical framework is required for rapidly identifying optimal class-specific segmentation parameters prior to a full-scale GEOBIA.

4.2.5 GEOBIA Accuracy Assessment

The complex spatial representations of GEOBIA relative scales of analysis creates a new challenge in evaluating object validity (Albrecht et al., 2010). In addition to thematic accuracy, objects have geometric boundaries. These boundaries require an additional spatial accuracy assessment to determine the degree of fitness of a segmentation to represent image features. Object validation therefore requires both an accurate representation of feature boundaries and correct thematic classification.

Object Boundary Assessment

In a spatial comparison between between geospatial objects, differences fall within two distinct groups: geometric and topological (Möller et al., 2007). Geometric differences arise through misregistration between image data. This is a factor only when data used for segmentation is separate from that used for validation. Misregistration error in the geographic space defined by the two datasets results in projection and spatial location differences. Conversely, topographical differences arise from a direct spatial comparison of object shape. Topographical differences are subdivided into five categories based upon the characteristics of object overlap (Whiteside et al., 2012b).

The simplest implementation of object validation is through a trial-and-error visual appraisal of the segmentation results (Lechner, 2012; Duro et al., 2012). This approach offers only a qualitative assessment of object spatial characteristics, relying more upon traditional point-based thematic accuracy assessment to quantify accuracy. However, this

approach lacks objectivity and robustness in assessing the spatial characteristics of objects. To ensure consistency over repeated assessments, the reference representation of a spatial dataset is required. The validation dataset most commonly used is a user-digitised image interpretation (Radoux et al., 2008; Whiteside et al., 2012b; Albrecht et al., 2010).

The use of a user-digitised dataset provides a fixed source for object assessment. It also raises some considerations however, as the user themselves determine what relative scale of analysis is appropriate for feature delineation. The selection of analysis scale is not only variable between individuals, but may also change and adapt as individual experience grows.

User-digitisation may be extracted from either an independent dataset or the dataset under analysis. If derived from the specific image under analysis, generating a validation dataset for all new data is required. For temporal studies of a single site, this may introduce potential errors through inconsistent user digitisation. It does, however, eliminate geometric differences in object comparison as segmentation and validation stem from the same data source (Möller et al., 2007). Conversely, if validation is derived from an independent source, geometric differences may be introduced. Additionally, differences in the sample scale of collected and validation data may alter how an analyst generalises boundaries. Despite this, the independence of the validation dataset makes it more suitable for on-going temporal studies. Past studies have explored both pixel and object based metrics to assess object accuracy relative to user-digitisation.

Whiteside et al. (2012b) and Möller et al. (2007) adopted an approach whereby random points within the image are selected for accuracy assessment. Within a circular area, groundcover delineations are interpreted and digitised. Albrecht et al. (2010) implement a technique to address variability within user image-interpretation, whereby delineations from multiple analysts were generalised in the accuracy assessment. This was achieved under the assumption that from multiple delineations, an average, meaningful measure of object boundary may be derived. Object fate analysis (OFA), a techniques that aims

to categorise the overlap between reference and segmented objects with regard to an expanding epsilon error band, was then implemented to assess topological object accuracy. Conversely, Möller et al. (2007) assessed both geometric and topological differences using two different object metrics within eCognition. This was achieved using multiple hierarchical object layers whereby reference data layer is super to the segmentation layer. Topological accuracy was derived using the relative area in super-object, and the geometric accuracy was derived using the relative position to super-object metrics.

Thematic Accuracy

The other aspect of GEOBIA accuracy assessment is thematic accuracy. Thematic accuracy assesses the predictive power of a classification algorithm. Thematic accuracy is typically point based, whereby the thematic assignment by a classifier at a location is compared against that of a validation set. Point-based thematic assessments provide class-by-class accuracy of a classification, from which the overall accuracy can be calculated. Where practical, validation datasets are constructed from direct field measurements to ensure maximum accuracy.

Remote sensing classification is built upon class definitions that are both mutually exclusive and exhaustive. Under these definitions, each unit of an analysis (whether object or pixel) can be assigned to one, and only one, thematic class. The objective of spatial generalisation is to improve the exclusivity and exhaustiveness of class definitions. Application of the wrong analysis scale (through an incorrect segmentation scale), may result in an inappropriate degree of spatial generalisation that fails to meet these class definition goals. Classification accuracy may be degraded by two forms of segmentation inaccuracy: under-segmentation and over-segmentation (Liu and Xia, 2010).

4.2.6 Under-segmentation

Under-segmentation occurs when segmentation results in image objects that are larger than the corresponding real-world objects (see Fig. 4.2) (Liu and Xia, 2010). Under-segmented objects fail to adequately capture bonafide boundaries (Johnson and Xie, 2013). This results in either object boundaries that cross multiple features, or smaller features merged into larger surrounding objects. The properties of these objects no longer represent a single class, violating mutual exclusivity, and reducing classification accuracy. As under-segmentation reduces bona fide boundary accuracy, an object spatial accuracy assessment may be used to identify under-segmentation.

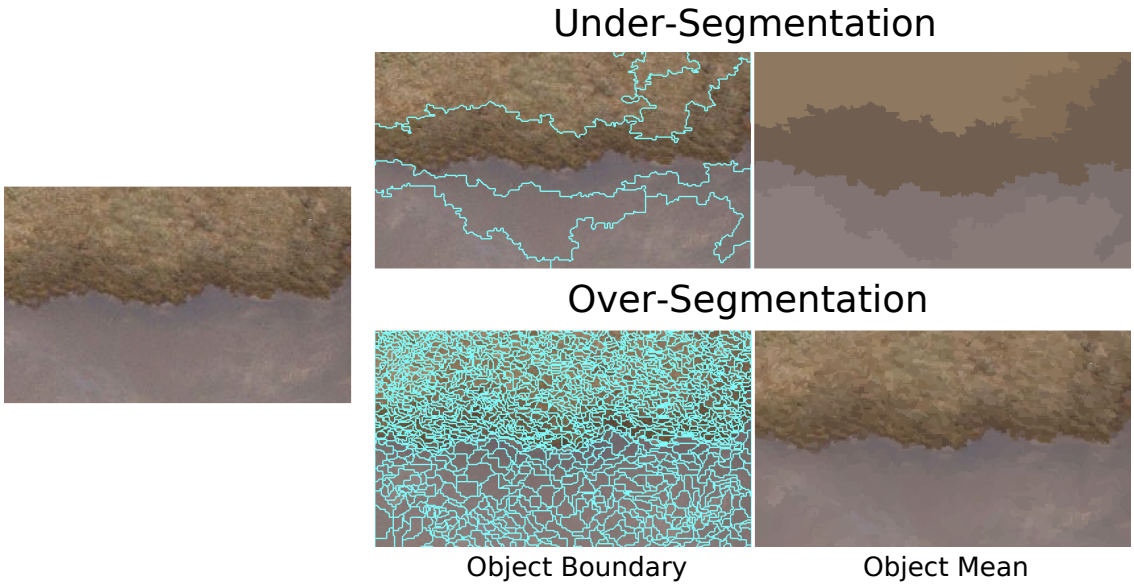

Figure 4.2: Comparison of the effects of under- and over-segmentation. Under-segmentation fails to delineate the bonafide boundaries between grasslands and mudflat. Over-segmentation fails to remove excess spatial variability.

4.2.7 Over-segmentation

Over-segmentation occurs when segmentation generates small image objects that lack spatial generalisation (see Fig. 4.2) (Liu and Xia, 2010). This lack of spatial generalisation fails to significantly reduce local variance. This is represented by features with excessive

object fiat boundaries. As a feature is progressively segmented into smaller and smaller objects, the overall spatial generalisation is reduced. Insufficient spatial generalisation fails to reduce the spatial variation that undermines accurate classification. As over-segmentation reduces classification accuracy, a thematic accuracy assessment may be used to identifying over-segmentation.

Under- and over-segmentation are linked with the relative scale of analysis. However, features between classes may occur at different relative scales. It is therefore clear that a single segmentation scale is inappropriate for addressing both the under- and over-segmentation of all classes. This requires the identification of class-specific relative analysis scales and their incorporation into the one analysis.

4.2.8 Texture

In addition to GEOBIA, image texture models provide a second approach to spatial generalisation. Texture models attempt to quantify the replications, symmetries and patterns in tonal structure across the image (Woodcock and Strahler, 1987). A texture model attempts to quantify the tonal structure within a local neighbourhood using a single metric. Compared with the relative analysis scale of GEOBIA whereby object shape and size shift according to the underlying data, the analysis scale of texture metrics retain the static structure of sample scale. However, unlike the absolute sample scale of data, the analysis scale of texture metrics are not fixed. Modifying the local neighbourhood extents of the model allows control over the scale of analysis for the derived metric.

Previous research has demonstrated that GEOBIA and image texture modelling are by no means mutually exclusive approaches for spatial generalisation (Puissant et al., 2005; Shinde and Shrivastava, 2012; Kim et al., 2009; Laliberte et al., 2012). Limitations remain in the integration of texture metrics into GEOBIA. The blurring of class boundaries that occurs with neighbourhood-based texture models obscures boundaries between features. This excludes the applicability of texture metrics within the segmentation phase. The

value of texture metrics therefore lies more within the statistical measures a defined object may extract from them.

4.2.9 Paper Aim

The primary aim of this paper is to present a framework that identifies optimal segmentation parameters for class-specific relative scales of analysis. Image segmentation is conducted using the eCognition software package. The identification of eCognition parameters is achieved through the use of user-digitised training subsets. The framework explores the separation of GEOBIA into two phases: the identification of relative analysis scale and the refinement of object shape. Scale identification aims to identify the optimal, class-specific relative scales of object segmentation. This identification is achieved with regard to the principles of over- and under-segmentation. Furthermore, the role of additional texture metrics for identifying relative analysis scales are explored. The second phase of shape refinement expands upon the identified relative segmentation scales by exploring the potential for further shape refinement. Refinement of object shapes seeks to improve the spatial fit of segmented objects to digitised reference objects.

4.3 Methods

4.3.1 Study Site and Data Collection

The study revisits a dataset previously explored within a texture metrics selection framework (see Chapter 3). Table 4.1 presents the data collection and spatial accuracy, while Table 4.2 presents the radiometric calibration results. UAS data was collected over a 200 m stretch of coastline using a 6-band TetraCam miniature multiple camera array (Mini-MCA) attached to a MikroKopter UAS (see Fig. 4.3). Filters used were 490, 530, 570, 670, 700 and 750 nm (10 nm FWHM). The 490 nm channel was discarded however, due to poor calibration results. Individual images were corrected for sensor aberrations, and

mosaicked into an orthophoto with a 5 cm spatial resolution, using the AgiSoft PhotoScan Professional software package. The multispectral ortho-imagery was calibrated to reflectance using an empirical line transformation based on three spectral ground control targets measured with an ASD HandHeld2 directly after the UAS flight. The normalised difference vegetation index (NDVI) and the red-edge normalised difference vegetation index were derived from the multispectral image.

Table 4.1: Image Acquisition Details and Construction Accuracy

Site	Date	UAS Images	GCPs	Samples	Bands	Spatial Res.	RMSE
Ralphs Bay	25/11/2011	149	23	53	6	0.05 m	0.15 m

Table 4.2: Sensor Calibration Results

Wavelength (nm)	490	530	570	670	700	750
EL Calibration (r^2)	0.514	0.989	0.971	0.983	0.956	0.835

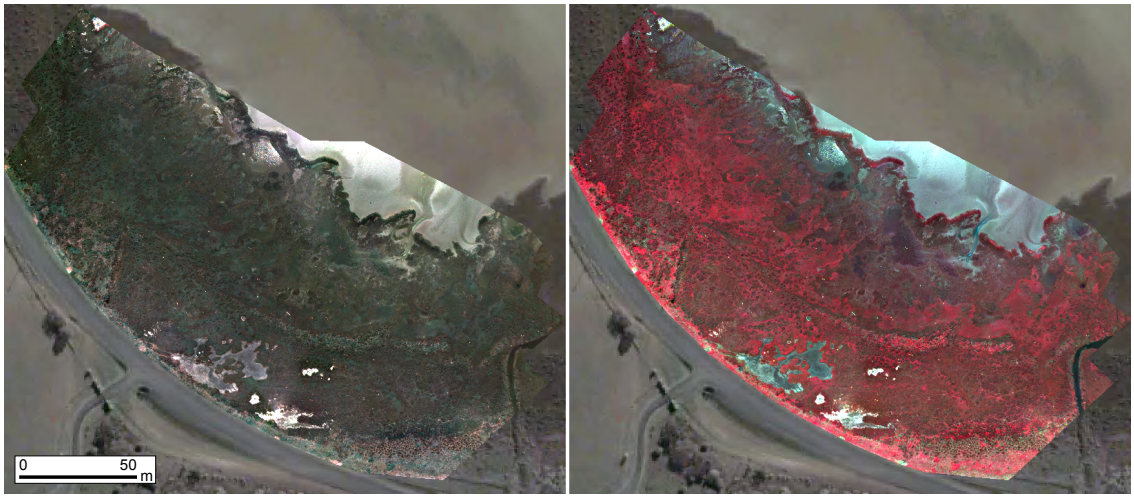

Figure 4.3: QuickBird image of the saltmarsh study site overlaid with both UAS generated RGB and false colour orthophotos.

The saltmarsh study site was dominated primarily by seven groundcover classes divided into four native vegetation and three non-vegetation classes. The four vegetation classes consisted of common native saltmarsh species: *Samolus repens*, *Sarcocornia sp.* (*Sarcocornia blackiana* and *Sarcocornia quinqueflora*), *Tecticornia arbuscula* and *Gahnia filum*. The three non-vegetation classes were intertidal sand flats, inundated mudflats, and saltpans. The spatial structure of these seven groundcover classes was explored in more detail in a previous texture-selection framework study (see Chapter 3).

4.3.2 Calculation of Texture Metrics

A random forest-based machine learning framework was previously implemented to identify relevant texture metrics. Texture metrics were assessed from four different models: first order kernel, GLCM, LBP and wavelet. Class-specific texture metrics were identified (see Chapter 3) and calculated for the full image (see Table 4.3) . Texture metrics were excluded from the segmentation process, and were used only to derive additional statistical properties for the final image objects.

Table 4.3: List of the final determination of class-specific texture metrics.

Samolus sp.	*Sarcocornia sp.*	*Tecticornia sp.*	*Gahnia sp.*
FO: NDVI Mean K15	FO: 750 Mean K15	GLCM: 670 Mean K15	FO: 670 Mean K15
GLCM : 750 Mean K15	GLCM: RE-NDVI Dis K15	FO: 700 Skew K15	FO: NDVI Mean K13
	GLCM: RE-NDVI Hom K15	FO: 530 Kurt K15	FO: 700 Skew K15
	GLCM: 700 Ent K15	GLCM: NDVI Cor K15	FO: 750 Mean K15
	GLCM: 700 Cor K15	FO: 700 Kurt K15	GLCM: RE-NDVI Hom K15

Sand	Mudflats	SaltPan
FO: RE-NDVI Mean K13	FO: RE-NDVI Mean K13	FO: RE-NDVI Mean K13

4.3.3 eCognition Image Segmentation

Image data was segmented by the eCognition[1] software package developed by Trimble. Data was segmented using the multi-resolution segmentation algorithm (Benz et al., 2004). This algorithm utilises a bottom-up approach, beginning with objects of individual pixels. Neighbouring objects are iteratively merged until the threshold of intra-object homogeneity is reached. Image segmentation in eCognition is controlled by four main parameters: scale, image layer selection, layer weightings and shape/compactness.

Scale is a unitless parameter used to set a relative threshold for intra-object homogeneity (Duro et al., 2012). As the algorithm is a bottom-up approach, increasing scale does not redefine segmentation boundaries, but rather dissolves existing ones (see Fig.4.4). The image layer selection provides the underlying pixel values for object growing. Layer weighting can be applied to image layers to preference specific data layers in the segmentation process.

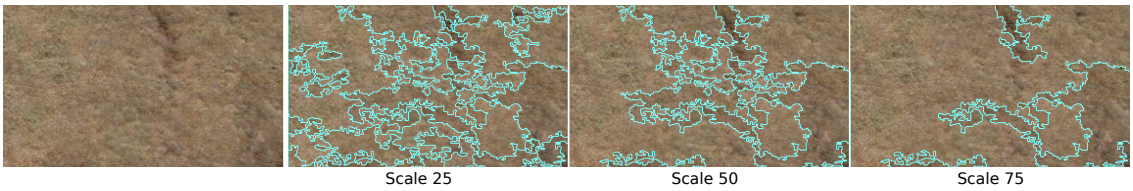

Figure 4.4: Comparison of increasing scale of grassland segmentation. Notable is that increasing scale does not introduce new boundaries but rather dissolves existing ones.

The shape setting and its extension compactness provide additional refinement of object boundaries. Shape provides a relative measure of the importance of pixel values for calculating an objects border. The lower the measure, the more strictly a border's path follows the pixel values. Conversely, the larger the measure, the more relaxed object borders become. This results in a smoother, more generalised border path (see Fig.4.5).

[1] http://www.ecognition.com/

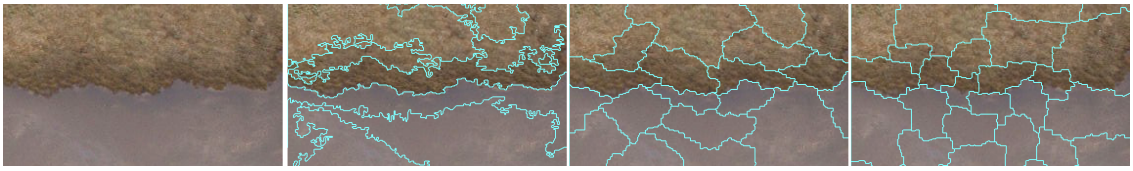

Figure 4.5: Comparison of the effects of shape and compactness measures. Noteable is the decreased boundary variation within increasing shape and the decreased object variability with increasing compactness.

The compactness setting is an extension of shape. Object compactness is defined as the ratio of perimeter to area, whereby the circle is the most compact object. Therefore, higher compactness index result in object shapes more closely resembling circles. This in turn reduces variation between object shape.

Increasing scale dissolves object boundaries. As class intra-variation is less than inter-variation, it can be expected that an increasing scale will disolve within-class fiat boundaries before between-class bonafide boundaries. The GEOBIA framework is required to identify two aspects of this process: i) bonafide boundaries that spatially delineate neighbouring features, and ii) fiat boundaries that provide optimal spatial generalisation for class separation. Towards these goals, the GEOBIA framework proposed in this study investigates the scale, shape, and layer weighting parameters of eCognition segmentation. The compactness parameter was set at constant value of 0.

Training Subsets

In the proposed GEOBIA framework, the identification of segmentation scale was class-specific. It identified class-specific boundaries through machine learning assisted by user digitisation of bonafide boundaries. Training data were digitised from the same UAS source layer used in the segmentation to mitigate spatial object inaccuracy through mis-registration. Representative subsets were identified for each of the thematic classes based upon expert knowledge, field experience and collected sample field-data (including geolo-

cated terrestrial data). Subsets were extracted using eCognition, and user-digitised using ArcGIS to produce qualitative class boundaries.

4.3.4 Optimal Segmentation Scale

A workflow was developed to identify the optimal scale of image segmentation (see Fig.4.6). The optimal scale of image segmentation was defined as the scale of greatest class separability with spatial delineation of all class features. This requires a spatial accuracy assessment to determine spatial delineation and classification accuracy assessment to determine class separability.

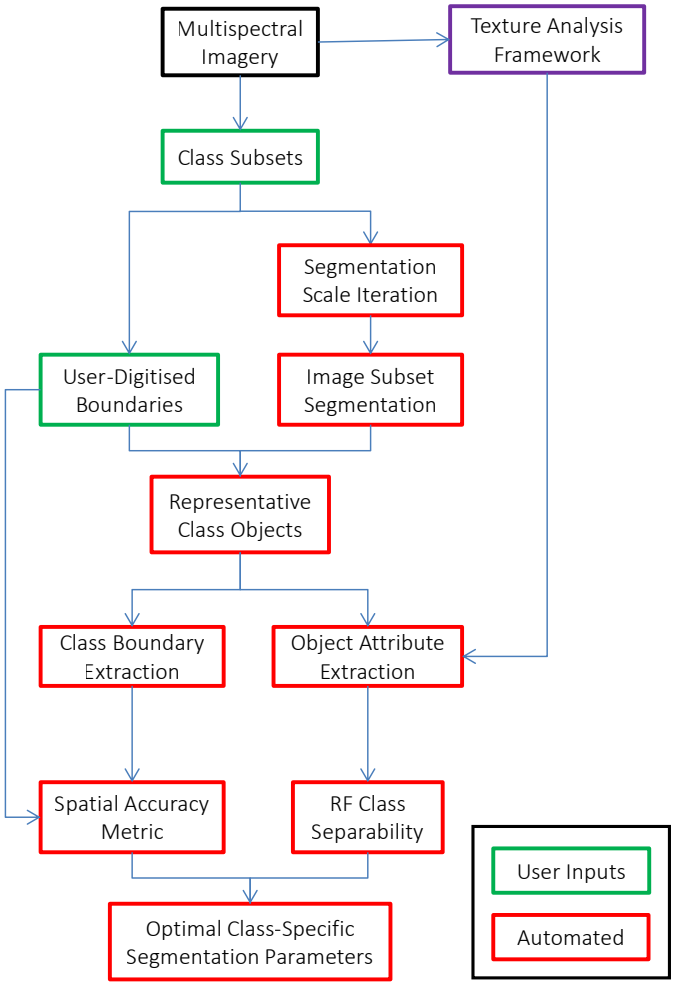

Figure 4.6: Workflow for identifying class-specific optimal scales of image segmentation with regard to over- and under-segmentation.

Spatial Accuracy & the Identification of Under-Segmentation

Subsets are first extracted using eCognition, and then segmented between scales 3 and 100. Each segmentation result was exported as a vector file (Shapefile). Vector objects contain the statistical attributes of the underlying spectral and texture metrics. The OGR Python library was used to process the segmentation and digitised subset layers. A best-fit segmentation bonafide boundary was identified based upon the user digitised boundary (see Fig.4.7). This was done by calculating the area overlap of each object with the classes within the user digitised layer. Objects were then labelled based upon the highest proportion of class overlap. Spatial metrics used to assess object overlap are: agreement, omission and commission. These three metrics were used to determine the spatial accuracy of the segmentation relative to the user-digitisation.

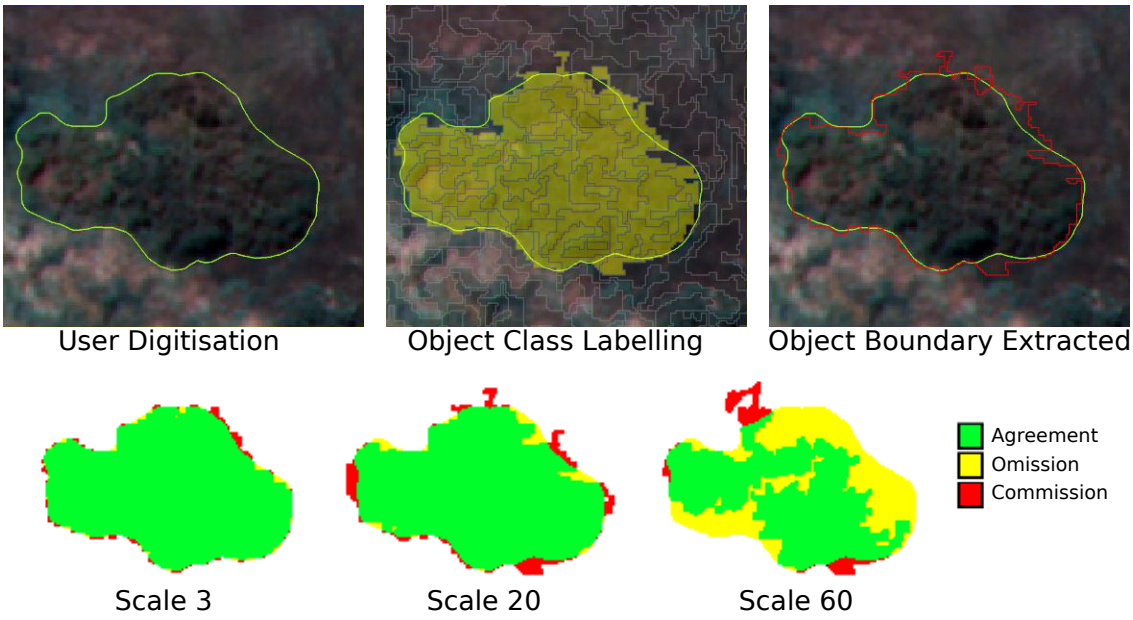

Figure 4.7: Illustration of object extraction based upon user digitisation for spatial accuracy assessment. Segmentation objects are initially labelled based upon user digitasation, and the best-fit boundary extracted. Spatial metrics of agreement, omission and commission are used to assess accuracy.

An analysis of the spatial accuracy over the segmentation range was used to identify

under-segmentation. This was achieved through the confirmation of bonafide boundaries within all class-specific subsets. The scale of under-segmentation was identified whereby any class-specific training subset recorded a 100% rate of omission. This segmentation scale marked the upper threshold limit, whereby scales at or in excess of this fail to reliably segment class features.

Classification Accuracy & the Identification of Over-Segmentation

Over-segmentation was used to identify the scale of optimal class separation. The degree of spatial generalisation to achieve optimal class separation is relative to the characteristics of the classes to be separated. It therefore requires a test of class separability of the labelled objects generated by fiat boundaries within each segmentation scale. The Random Forest (RF) ensemble classifier was used to test class-specific separability. Objects labelled within all subsets at each scale of segmentation, were used to create a RF model (see Fig.4.8). The class-specific out-of-bag (OOB) error is used to test class-specific separability at each segmentation scale. The scale of optimal segmentation was identified as the scale of greatest class separability lower than the scale of under-segmentation.

Figure 4.8: Illustration of object extraction based upon user digitisation for classification accuracy assessment. Segmentation objects are initially labelled based upon user digitasation, and individual object statistics are extracted. A random forest model is constructed from all subsets at the same segmentation scale, and class-specific separability is subsequently tested.

4.3.5 Random Forest Layer Weight

Layer weighting requires an estimate of the relative importance of image layers in delineating a specific class. Random forest can be used to assess the relative importance of image layers. A random forest model was generated from training areas using only pixel-based information. Class-specific importance measures for each spectral band were estimated. These importance measures were used to set the layer weights in the image segmentation.

4.3.6 Optimal Object Scale Shape Refinement

The second phase of the GEOBIA framework aims to optimise the fit of segmented object boundaries with the user digitised subset. The identification of class-specific scales produces bonafide boundaries that best fit the qualitative boundaries represented in the user digitisation. Application of the shape parameter to the segmentation scale increases the generalisation of these boundaries, potentially creating a better match to the reference boundaries digitised by the user.

Segmentation of the subset areas was repeated once more for each class. The segmentation scale remained at each classes identified optimal scale. The shape parameter was iterated between 0.0 and 0.8 with increments of 0.01. The resulting segments were labelled based upon the corresponding user digitisation of the subset. The fiat boundaries were dissolved, and the area agreement spatial metric was used to test the spatial accuracy of the segmentation. The optimal shape parameter was identified as that which minimises disagreement between the segmentation and the photo-interpretation training set.

4.3.7 Analyses Overview

The GEOBIA framework was used to test the classification and spatial accuracy performance of a number of segmentation approaches (see Table 4.4). the Static Scale analysis

provided a baseline GEOBIA result, and was the same approach utilised in Chapter 3. The Optimal Scale analysis expanded upon the Static Scale to explore the effects of class-specific segmentation scales. The Texture analysis incorporates additional texture metrics into object attributes to explore the effects of texture-based spatial generalisation with the GEOBIA framework. The Layer Weight analysis extended upon the Texture analysis, exploring the effect on spatial accuracy of using RF-derived layer weighting. The Shape analysis was similar to the goals of the Layer Weight analysis, except the shape parameter is explored for improving spatial accuracy. The final analysis was Shape & LW, which aims to test the combined RF-derived layer weights and shape parameter for improving spatial accuracy.

Table 4.4: List of the six different analyses and their corresponding parameters.

Analysis	Object Attributes	Scale	Layer Weight	Shape
Static Scale	Spectral	75	1	0
Optimal Scale	Spectral	Class-Specific	1	0
Texture	Spectral & Texture	Class-Specific	1	0
Layer Weight	Spectral & Texture	Class-Specific	RF Class Specific	0
Shape	Spectral & Texture	Class-Specific	1	Class-Specific
Shape & LW	Spectral & Texture	Class-Specific	RF Class Specific	Class-Specific

4.4 Results

4.4.1 Subset Analysis

Static Scale Analysis

The rudimentary GEOBIA approach implemented within Chapter 3 was repeated. This time however, the spatial validity of image segmentation at a scale of 75 was tested (see Table 4.5). The additional spatial accuracy assessment reveals the scale under-segments the image, with features from two separate groundcover classes (*Tecitcornia sp.*

and *Gahnia sp.*) returning 100% omission within a subset.

Table 4.5: Static Scale GEOBIA class-specific spatial and classification accuracy (%).

Class	Scale	Spatial Acc.	Class Acc.
Gahnia sp.	75	-	0.777
Mudflats	75	0.803	0.813
Saltpan	75	0.804	0.759
Samolus sp.	75	0.813	0.436
Sand	75	0.838	0.692
Sarcocornia sp.	75	0.717	0.454
Tecticornia sp.	75	-	0.567

Over- and Under-Segmentation Assessment

The full image was segmented between scales 3 and 100. Each segmentation result was tested for over- and under-segmentation. Classification and spatial accuracy assessments were made for class-specific subsets. The overall classification and spatial accuracy reveal the effects of over-segmentation (see Fig.4.9). The overall spatial accuracy illustrates that as objects become smaller, the potential fit of segmented class boundaries with the user digitisation is improved. Conversely, the reduction in object size leads to decreased classification accuracy, as insufficient spatial generalisation results in less separability.

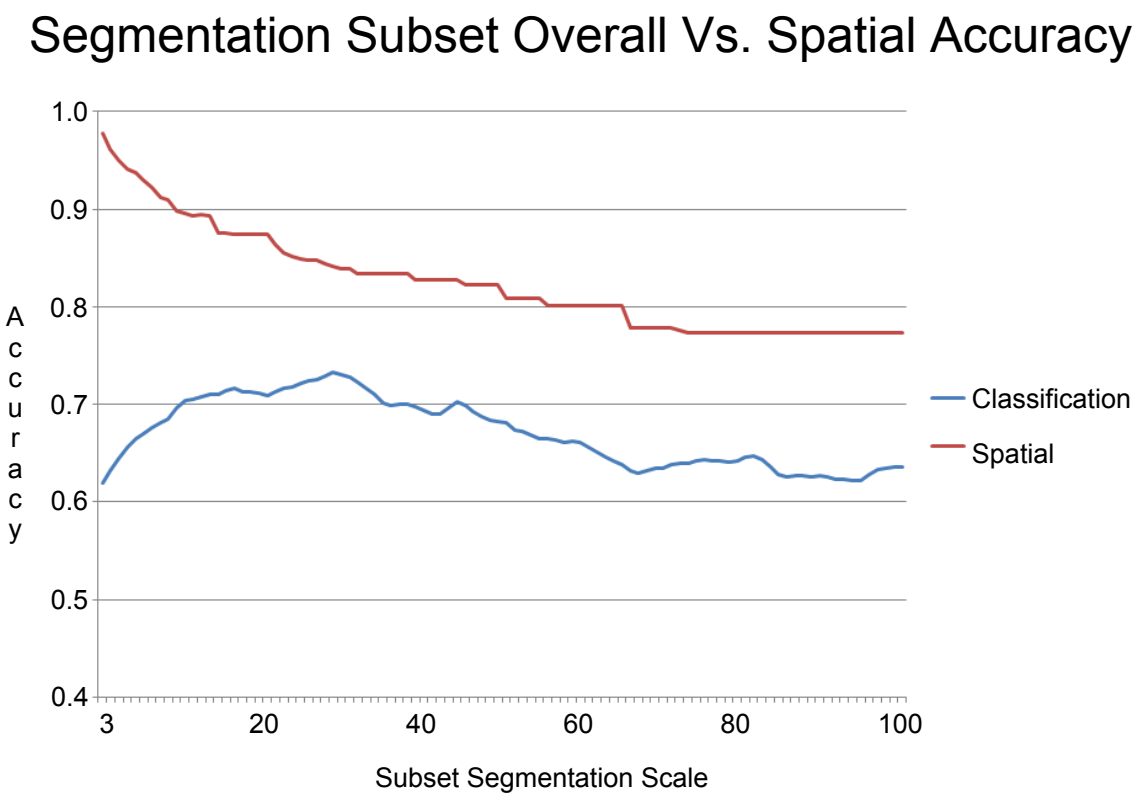

Figure 4.9: Comparison of increasing segmentation scale upon the overall spatial and classification accuracy of the training subsets.

The initial class labelling of the segmentation subsets was used to identify under-segmentation. An analysis of the class subsets revealed that within the maximum scale limit of 100, two classes were found to have recorded 100% omission within a subset: *Gahnia sp.* (scale 71) and *Tecticornia sp.* (scale 52).

Optimal Scale Analysis

Class-specific scales (based solely upon spectral data) were tested across the segmentation scale range. Optimal class-specific scales were selected and their classification and spatial accuracy recorded (see Fig.4.10). The identified relative scales ranged between 19 (*Samolus sp.*) and 55 (*Gahnia sp.*). Selecting class-specific scales improved both classification and spatial accuracy for all classes (see Table 4.6).

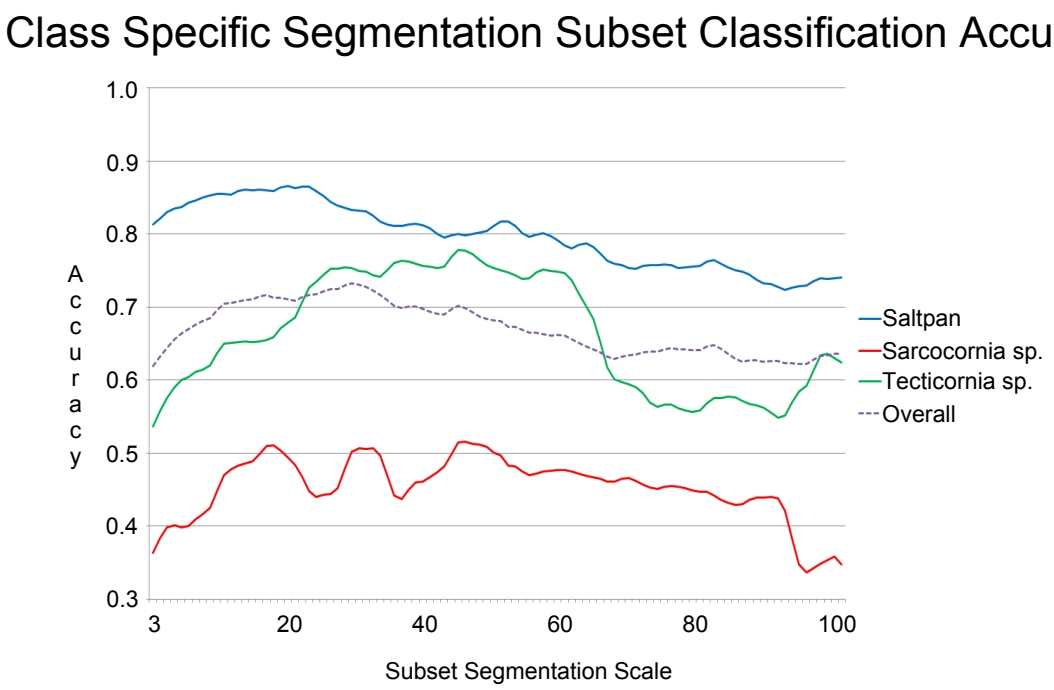

Figure 4.10: Comparison of increasing segmentation scale upon the classification accuracy of the three training subsets: Saltpan, *Sarcocornia sp.* and *Tecticornia sp.*.

Table 4.6: Optimal Scale GEOBIA class-specific spatial and classification accuracy (%).

Class	Scale	Spatial Acc.	Class Acc.
Gahnia sp.	55	0.798	0.802
Mudflats	52	0.808	0.841
Saltpan	22	0.872	0.861
Samolus sp.	19	0.874	0.654
Sand	29	0.847	0.811
Sarcocornia sp.	46	0.822	0.515
Tecticornia sp.	47	0.827	0.770

Spectral & Texture

Class-specific texture metrics were identified by implementing a RF-based texture selection framework (see Table 4.3). Classification of the subset segmentation between 3 and

100 was repeated, this time including texture metrics as object attributes. Optimal class-specific scales, classification and spatial accuracy were calculated and compared against the previous spectral-only subset (see Table 4.7). Overall classification performance was improved with the addition of texture metrics. Furthermore, classification performance at smaller scales was also improved for all classes (see Fig.4.11). This resulted in a reduction of the optimal class-specific segmentation scale. This reduction of optimal scale resulted in smaller image objects that improved spatial accuracy. The largest scale change was recorded by *Sarcocornia sp.* with a scale reduction of 17 resulting in a 5.2% increase in spatial accuracy. Conversely, the scale of sand was reduced by a single scale, with no measured effect upon its spatial accuracy.

Table 4.7: Texture GEOBIA class-specific spatial and classification accuracy (%).

Class	Scale	Spatial Acc.	Class Acc.
Gahnia sp.	29	0.847	0.824
Mudflats	42	0.827	0865
Saltpan	18	0.875	0.866
Samolus sp.	16	0.893	0.664
Sand	28	0.847	0.819
Sarcocornia sp.	18	0.874	0.539
Tecticornia sp.	30	0.843	0.778

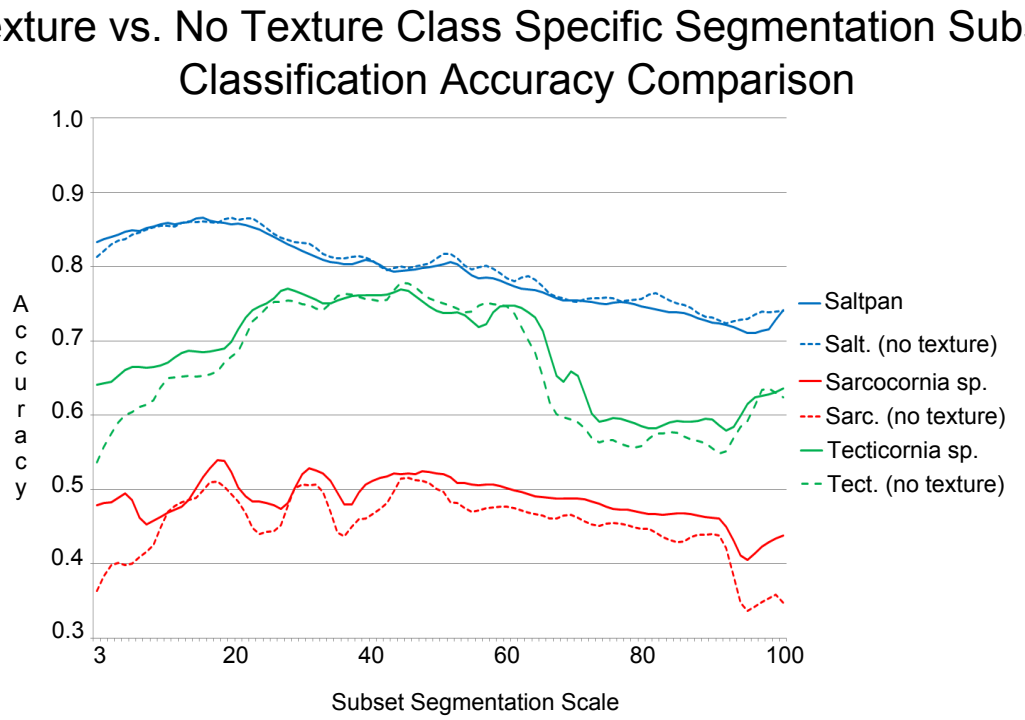

Figure 4.11: Comparison of increasing segmentation scale upon the classification accuracy of the three training subsets: Saltpan, *Sarcocornia sp.* and *Tecticornia sp.* between texture and no texture object attributes. Notable is the increase in classification accuracy at smaller scales.

Layer Weighting

A RF model was used to calculate the relative importance of each spectral layer to each class. Layer weightings were set to these class-specific relative importance measures (see Table 4.8). Image subsets were segmented and the corresponding classification and spatial accuracy were recorded in Table 4.9. It was found that the layer weight substitution improved the spatial accuracy of all classes. The greatest spatial improvements were recorded by mudflats (12.6%) and sand (11.8%). *Tecticornia sp.* recorded the lowest spatial improvement (1.3%). The overall classification accuracy was reduced, with only *Samolus sp.* recording an increase in accuracy, while the accuracy of mudflats was unchanged. Sand suffered the greatest reduction in classification accuracy (-11.8%), followed by *Gahnia sp.* (-7.2%) and *Tecticornia sp.* (-7.1%).

Table 4.8: Class-specific spectral layer weightings derived from random forest importance

	530	570	670	700	750	NDVI	RENDVI
Gahnia sp.	1.325	1.459	1.305	1.253	1.429	1.201	1.436
Mudflats	0.605	0.694	0.680	0.916	0.875	1.078	1.487
Saltpan	1.291	1.384	1.272	1.147	1.359	1.227	1.371
Samolus sp.	1.434	1.308	1.474	1.335	1.277	1.454	1.439
Sand	1.435	1.422	1.180	1.280	1.348	1.419	1.501
Sarcocornia sp.	1.488	1.526	1.503	1.470	1.463	1.482	1.492
Tecticornia sp.	1.135	0.822	1.445	1.115	1.254	1.324	1.012

Table 4.9: Layer Weight GEOBIA class-specific spatial and classification accuracy (%).

Class	Scale	Spatial Acc.	Class Acc.
Gahnia sp.	29	0.908	0.752
Mudflats	42	0.953	0.865
Saltpan	18	0.971	0.858
Samolus sp.	16	0.980	0.674
Sand	28	0.965	0.701
Sarcocornia sp.	18	0.959	0.538
Tecticornia sp.	30	0.856	0.707

Shape

The shape parameter was iterated between 0.0 and 0.8, using optimal class segmentation scales with a default layer weighting of 1. The classification and spatial accuracy of the subsets was calculated. The optimal weight parameter was selected based upon the greatest class-specific spatial accuracy. Spatial and classification accuracy are presented in Table 4.10. When compared against RF-derived layer weighting, boundary generalisation using the shape parameter further improves the overall spatial accuracy but continues to

degrade the classification performance.

Table 4.10: Shape GEOBIA class-specific spatial and classification accuracy (%).

Class	Shape	Spatial Acc.	Class Acc.
Gahnia sp.	0.36	0.939	0.701
Mudflats	0.06	0.962	0.847
Saltpan	0.13	0.974	0.846
Samolus sp.	0.40	0.977	0.52
Sand	0.26	0.963	0.722
Sarcocornia sp.	0.36	0.957	0.435
Tecticornia sp.	0.02	0.863	0.769

Shape and Layer Weighting

The subsets were segmented once more to explore the combined effects of RF-derived layer weighting and the shape parameter. Utilising the RF-derived layer weighting, subset segmentations were generated using the shape parameter iterated between 0.0 and 0.8. Optimal shape parameters were identified, and the spatial and classification accuracies recorded (see Table 4.11). The complementary effect of layer weighting and shape result in the highest spatial accuracy of all the analyses. However, the increase in spatial accuracy is offset by a further decrease in classification accuracy. Furthermore, with the single exception of *Tecticornia sp.*, less border generalisation using the shape parameter was required when segmenting the image using the RF-derived layer weighting.

Table 4.11: Shape & LW GEOBIA class-specific spatial and classification accuracy (%).

Class	Shape	Spatial Acc.	Class Acc.
Gahnia sp.	0.12	0.941	0.803
Mudflats	0.02	0.968	0.831
Saltpan	0.06	0.974	0.863
Samolus sp.	0.04	0.982	0.592
Sand	0.08	0.970	0.775
Sarcocornia sp.	0.18	0.966	0.599
Tecticornia sp.	0.22	0.892	0.450

4.4.2 Full Image Classification

The subset analyses were extended to explore their real-world application. Parameters identified in each of the six analyses were applied to the entire saltmarsh image. For each analysis, class probability layers were calculated. A final thematic layer was generated by collapsing each point to the class of highest probability. The spatial and classification accuracy of these final classification maps were recorded and compared (see Table 4.12).

The results indicate that optimal classification performance is achieved using texture metrics and no object boundary refinement. Refining object boundaries using the shape and RF-based layer weightings improves spatial accuracy, but at the cost of classification accuracy. This is illustrated with the greatest gain in spatial accuracy achieved by utilising a combination of shape and RF-based layer weightings. Doing so however, almost entirely negates the improvements in classification accuracy provided by texture metrics.

Table 4.12: Overall spatial and classification accuracies for full image classification (%).

Full Image Class.	Spatial Acc.	Class Acc.
Static Scale	-	0.677
Optimal Scale	0.835	0.841
Texture	0.858	0.967
Layer Weight	0.941	0.897
Shape	0.947	0.860
Shape & LW	0.956	0.844

Figure 4.12 illustrates the differences between the classification results produced by the static scale, texture, and shape & LW analyses. Of particular note is the differences within the transitional area between *Sarcocornia sp.* and the mudflats. The inclusion of texture metrics notably improves the classification of this area. The refinement of object shape, however, once again introduces misclassification despite smoother class boundaries.

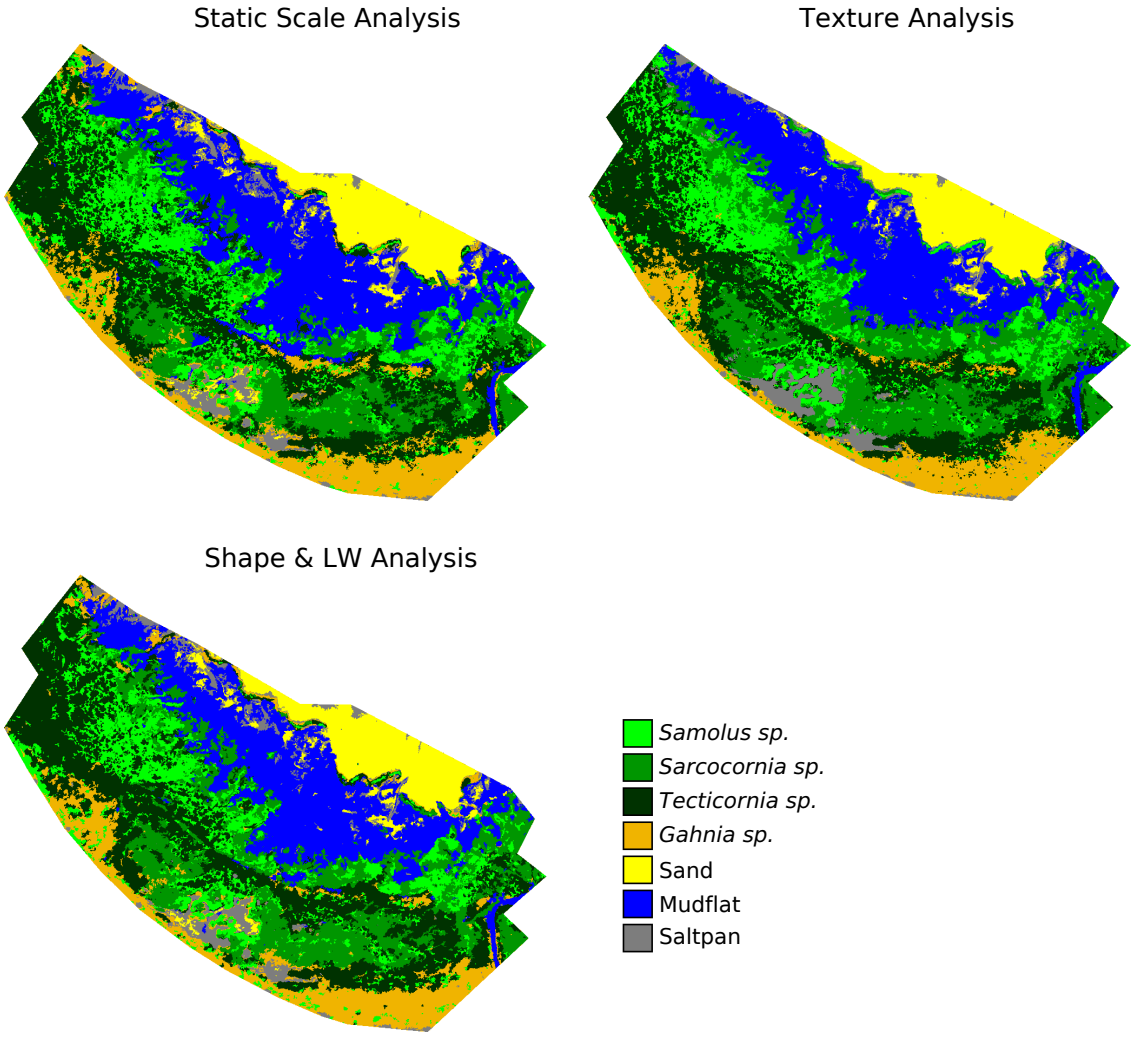

Figure 4.12: Classification results illustrating the effects upon both classification and spatial accuracy of three GEOBIA analyses: static scale, texture analysis, and shape & LW analyses.

4.5 Discussion

The results of this study illustrate the importance of assessing the spatial accuracy of GEOBIA. The restriction of the Static Scale analysis to a single segmentation scale ignores that each class has its own optimal scale of analysis. This is reflected in the resulting under-segmentation revealed by the spatial accuracy assessment (see Table 4.5). By identifying class-specific segmentation scales, this framework incorporates these class-

specific scales of analysis into the analysis. This has measureable benefits for both spatial and classification accuracy (see Table 4.6).

4.5.1 Spatial Analysis Domain and The Role of Texture Metrics

Figure 4.9 illustrates that within the training subsets, the high spatial accuracy from over-segmentation is counteracted by decreasing classification accuracy. While it is well established that texture metrics are beneficial to classification accuracy, they may also offer indirect benefits. Table 4.12 shows that texture metrics directly improved classification accuracy. In addition, the inclusion of texture reduced the optimal segmentation scale, as classification performance was maintained for smaller objects. It is therefore suggested that texture metrics within GEOBIA have both direct and indirect benefits: a direct influence on classification accuracy and an indirect influence on spatial accuracy.

The benefit of texture metrics to GEOBIA may arise from differences in their respective spatial analysis domains. The spatial analysis domain of a texture metric is defined by the scale of the model (e.g. a kernel or radius). In that regard, each texture metric has a spatial analysis domain that remains fixed across the extents of the data. This domain is therefore independent of the underlying tonal variation. Conversely, the spatial analysis domain of an image object is defined by the perimeter of that object. As local variance changes across the extents of an image, so too do the defined shape of any given image object. In that regard, it can be said that GEOBIA has a dynamic spatial analysis domain that is dependent upon local tonal variation.

Image object attributes are derived from the statistical properties of their enclosed pixels. These properties are analogous with a simple first order texture model, albeit that the spatial analysis domain of the texture model is fixed while objects is dynamic. However, as image texture is scale dependent, larger image objects may generalise broader tonal structure more efficiently than smaller objects.

The success of balancing classification and spatial accuracy requires the identification of an optimal scale of analysis large enough to adequately generalise tonal structures while also small enough to spatially delineate features. This highlights a potential value of additional texture metrics. Texture metrics may be used to shift the burden of generalising tonal structure from the spatial analysis domain of objects, to the domain of a texture metric. This would reduce pressure on image objects for spatial generalisation, allowing segmentation to focus more upon spatial accuracy. Within this context, the utility of texture metrics becomes linked with segmentation scale, with smaller scales benefiting more than larger ones (see Fig.4.11).

The selection of segmentation scale within this study relies upon identifying two parameters: the scale of under-segmentation and the scale of optimal class separability. The scale of under-segmentation relies upon identifying the scale where the smallest class feature is omitted. Conversely the optimal class separability relies upon maximising class separability. It may therefore be possible, under certain conditions (e.g. structurally complex features of highly variable size) that the scale of optimal class separation exceeds the scale of under-segmentation. While one approach is to recognise the limitations of the classification, and exclude smaller features, another approach would be to introduce texture metrics into the analysis for the sole task of reducing the optimal segmentation scale.

4.5.2 Role of Qualitative User Digitisation within Quantitative Analysis

Attempts to refine object boundary shape using the shape parameter and RF-based layer weighting were successful. However, the result shows that improvements in spatial accuracy corresponded with increased misclassification rates. Confusion that contributes to this may arise from the use of user-digitised subsets, specifically the generalisation of feature boundaries that occurs with visual digitisation.

An automated digital segmentation results in a precise boundary. Small-scale quantitative

variation in the underlying data results in small fluctuations in object boundary paths (see Fig. 4.5). In contrast, the visual interpretation of an analyst downplays this small scale variation in favour of broader structures of shape, texture and image context. This results in generalised, qualitative boundaries. The increased misclassification recorded in this study, may arise from shifting a quantitative boundary to more closely fit a qualitative one. However, the classification accuracy assessment still remains a quantitative process. Ignoring small scale fluctuations may excise characteristics from a class into their neighbours. These mixed class objects may reduce class separability.

This questions the role of user digitisation within GEOBIA. Specifically if user digitisations should be treated as an approximation to identify suitable analysis scales, or as an exact representation of spatial boundaries. Utilised as an approximation, GEOBIA can skip further boundary generalisation, and avoid impacts on classification accuracy. However, by treating user digitisation as a rough approximation, it undermines their use for spatial accuracy assessments. What is required is a quantitative validation dataset that avoids the qualitative nature of visual digitisation. In this regard, it may be better to reduce the dimensionality of the dataset to limit user generalisation. One way would be to rely upon field-based point measurements that mark shifts between groundcover classes.

The alternative approach of utilising a qualitative digitisation as an exact representation may undermine further quantitative analysis. This may be preferable, however, if an analyst forgoes the final quantitative classification in favour of visual image interpretation. In this regard, the analyst benefits from the pre-construction of meaningful, spatially consistent objects prior to class labelling. Arguably, fitness-for-use also guides whether the training subset should be extended to spatial validation. Central to this is assessing the final use of the data, and therefore the practicality of quantitative or qualitative boundaries. For measuring phenomena through remote sensing analysis, including distribution, biomass estimates and change detection of vegetation, a quantitative analysis is

appropriate. Conversely, the smoother, generalised objects of qualitative boundaries may better translate to real-world mapping applications.

4.5.3 Important GEOBIA Characteristics

Developing a framework for GEOBIA parameter selection requires evaluating the spatial validity of object segmentation scales (Albrecht et al., 2010). Early GEOBIA assessments adopted the traditional point-based thematic accuracy assessments used within previous pixel-based classification (Darwish et al., 2003; Powers et al., 2012). However, it was clear that object spatial accuracy is a fundamental component of GEOBIA assessment. A large range of spatial metrics have been explored in the context of GEOBIA (Albrecht et al., 2010; Powers et al., 2012; Möller et al., 2007; Whiteside et al., 2012a). Both thematic and spatial accuracy are essential components of GEOBIA assessment, and are therefore critical elements in the development of a GEOBIA framework. When assessing the final GEOBIA results, only real bonafide boundaries have evident value. However fiat boundaries, while conceptual, still have a distinct value that is not represented within the final spatial accuracy assessment. The framework therefore requires the transfer of accuracy metrics to a preliminary phase to assess object validity.

From a visual perspective, fiat boundaries are abstract, conceptual delineations. They cannot therefore be spatially assessed using the same user-digitisation approach as bonafide boundaries. Their role, however, is in spatial generalisation, not delineation. Therefore classification separability becomes a more meaningful overall assessment of fiat boundaries. The framework presented here illustrates the significant accuracy benefit of identifying optimal fiat boundaries based upon class separability. By testing for over-segmentation, this framework acknowledges and incorporates the important role of fiat boundaries alongside bonafide boundaries.

In this study, texture metrics were calculated at fixed analysis scales prior to image segmentation. Other studies, however, have opted for the calculation of texture metrics based

upon segmentation results. These utilise the spatial delineation of objects to determine the analysis scale for texture metrics (Powers et al., 2012). This approach has obvious spatial benefits as it constrains texture metrics within object borders, thereby avoiding the characteristic smearing (i.e. border effect) that occurs between neighbouring classes when using a fixed neighbourhood. This approach however, relies upon the segmentation scale to determine the analysis scale of the texture metric, which in turn may be variable across the image extents. The results of this study suggest that the independence of texture analysis scale may be an important characteristic to reduce the burden of spatial generalisation upon segmentation scale.

4.5.4 Conclusion

This study successfully demonstrates a geospatial object-based image analysis (GEOBIA) framework that incorporates class-specific relative scales of segmentation to improve classification and spatial accuracy. Relative segmentation scales were selected by utilising digitised class-specific subsets. Spatial and classification accuracy assessments of subset segmentations were used to detect class-specific over- and under-segmentation. Through these accuracy assessments, optimal class-specific segmentation scales of observation were identified. Incorporating relative scales of segmentation improved GEOBIA classification of UAS saltmarsh data over a single scale GEOBIA (a 16.4% improvement).

A spatial accuracy assessment revealed that over-segmentation potentially improves GEOBIA spatial accuracy. This improvement however, was constrained by reduced classification accuracy as smaller objects provided insufficient spatial generalisation. It was found that texture metrics provided an additional, spatially independent source of spatial generalisation. This reduced the reliance upon GEOBIA for spatial generalisation, allowing limited over-segmentation. The addition of texture metrics alongside class-specific segmentation scales resulted in an improvement in both classification (12.6%) and spatial accuracy (2.3%). This demonstrates the dual role of GEOBIA for spatial delineation

and generalisation, and the capacity for texture metrics to assist in the role of spatial generalisation.

The foundation of this GEOBIA framework is user-digitised subsets. This study found that utilising the user-digitised subsets as an approximation resulted in the highest classification results. Attempts to further refine object shape to conform more closely to the user-digitised subsets succeeded in improving spatial accuracy. However, fitting GEOBIA segmentation to a qualitative digitisation resulted in a reduction of classification accuracy. A fundamental task that remains for this GEOBIA framework is the development of methodology to address the qualitative nature of user-digitisation, and improve the balance of GEOBIA spatial and classification accuracy.

Thesis Context

The sample scale of ultra-fine spatial resolution UAS imagery results in high local spatial complexity. Spatial generalisation of this complexity is key for the analysis and extraction of meaningful information. Chapter 4 demonstrates a GEOBIA framework that incorporates user digitised subsets for the identification of class-specific segmentation parameters. Additionally, Chapter 4 demonstrates the role additional texture metrics may play within GEOBIA. Chapters 3 & 4 together provide a broader framework for incorporating both texture modelling and GEOBIA for class-specific spatial generalisation, with demonstrated improvements for UAS image classification. Chapter 5 utilises this broader image analysis framework to map the spatial distribution of a saltmarsh shrub species as a precursor to estimating shrub above-ground biomass.

Chapter 5

Modelling Above-Ground Biomass of the Saltmarsh Shrub *Tecticornia arbuscula* Utilising UAS Remote Sensing

Chapter 5 focuses upon utilising UAS remote sensing for estimating the above-ground biomass of a small saltmarsh shrub species. Chapter 5 adapts field-based allometric modelling parameters for fine-scale UAS measurements.

5.1 Abstract

Estimations of plant above-ground biomass (AGB) are central for understanding carbon uptake by the bioterrestrial environment. Allometric modelling is the most accurate method for estimating plant AGB. The coarse sample scale of traditional manned aerial remote sensing platforms prohibits the direct measuring of allometric parameters, restricting the direct application of allometric AGB models. The unmanned aircraft system (UAS) is a novel remote sensing platform capable of generating data at an ultra-fine resolution sample scale suitable for measuring allometric parameters. This study demonstrates the application of UAS remote sensing for the AGB estimation of a small scale

saltmarsh shrub *Tecticornia arbuscula*. GEOBIA was used to classify UAS imagery, and extract the spatial distribution of *Tecticornia sp.*Ṡtructure-from-motion (SfM) was used to construct a high density point cloud, which after bare Earth filtering, was used to extract vegetation height information. *Tecticornia sp.* allometric structural modelling was used to constrain GEOBIA in order to segment *Tecticornia sp.* into candidate stems. *Tecticornia sp.* allometric AGB modelling was used to estimate the total *Tecticornia sp.* AGB across the study site. *Tecticornia sp.* AGB was estimated between 3,440.77 and 4,482.77 kg. This study demonstrates the capacity for ultra-fine resolution UAS data to measure allometric properties of small scale vegetation. The UAS has the potential for improving AGB estimation by generating consistent, accurate measurements.

5.2 Introduction

The upcoming fifth assessment of the United Nations Framework Convention on Climate Change (UNFCCC) identifies that anthropogenic carbon dioxide (CO_2) emissions are a significant contributor to the changing global climate. While burning fossil fuels are the primary source of human CO_2 emissions, deforestation of the terrestrial biosphere is also a major contributor. CO_2 is drawn from the atmosphere by vegetation and fixed within woody biomass, providing a long term carbon storage (Stephenson et al., 2014; Ahmed et al., 2013). Deforestation both releases stored CO_2 and reduces the capacity for the bioterrestrial environment to draw CO_2 from the atmosphere.

National efforts have begun to address climate change by assessing sources and sinks of CO_2 (Schimel, 1995). Financial incentives have been proposed in response to the economic benefits of deforestation. This introduces a competing market value to conserve established vegetation. Central to evaluating vegetation is calculating the potential carbon uptake and storage. The rate vegetation accumulates carbon is governed by local climate, seasonal changes, nutrient availability and vegetation age.

While the wood of forests may represent a significant carbon pool, once developed into a climax vegetation, their capacity to increase overall biomass may be limited environmentally (Anaya et al., 2009). Conversely, small-scale vegetation that lacks large woody species may not represent a significant storage of wood. However, the lack of a stable climax state, particularly in frequently disturbed environments, may result in a rapid cycle of establishment, carbon accumulation and senescence. Research has revealed that riparian environments, including saltmarsh and floodplains, have a high storage capacity for carbon within the build-up of anaerobic soil (Suchenwirth et al., 2012; Frolking et al., 2009). Fundamental to calculating either the carbon storage or uptake potential of vegetation are estimates of plant biomass (Lutz et al., 2008).

5.2.1 Biomass - Field Techniques

Biomass refers to plant or plant-derived biological material (Lutz et al., 2008) and has an approximate carbon content of 50% (Drake and Knox, 2003; Robinson et al., 2013). Although plant biomass is generated both above- and below-ground, the difficulty in extracting, measuring and modelling below-ground biomass commonly restricts estimation to above-ground biomass (AGB). The distribution of AGB in an ecosystem is a function of vegetation type, community structure and site condition (Roy and Ravan, 1996). Allometric models are the most accurate method for estimating plant AGB (Lu, 2006).

Allometry is the relationship between the shape and size of natural objects (Ahmed et al., 2013). Allometric modelling relies upon destructive sampling (Baskerville, 1972), whereby individual plants are harvested, dried and weighed. Structural parameters of harvested plants are measured (i.e. trunk diameter and height), and their relationship to dry weight statistically modelled (Picard et al., 2012; Baskerville, 1972; Feldpausch et al., 2012). Field-based estimations of AGB can then be made based upon measurable plant parameters (Roy and Ravan, 1996; Anaya et al., 2009). The selection of plant parameters is a balance between the speed of application and the accuracy of biomass estimation.

Allometric AGB modelling methods have been developed for a range of structural vegetation types. This includes trees (Ketterings et al., 2001; Nickless et al., 2011), shrubs (Murray and Jacobson, 1982; Ludwig et al., 1975) and groundcover (Ohmann et al., 2006; Johnson et al., 1988). Tree modelling is focused upon the main concentration of biomass within the central trunk, commonly utilising parameters of tree height (Feldpausch et al., 2012) and trunk diameter-at-breast-height (DBH) (Priedtis et al., 2012). Groundcover is typically dominated by thick mats of herbaceous species, which leaves AGB estimates of individual plants impractical. Instead groundcover AGB estimation focuses upon density and percentage area coverage. With shrubs, however, the branching structure and lack of centralised biomass makes AGB modelling more challenging. Rapid approaches to estimate AGB generalise the complex shrub structure to a single, volumetric shape (Ludwig et al., 1975; Murray and Jacobson, 1982), while more robust models estimate the AGB of individual shrub stems, leading to a more accurate yet labour intensive result (Rosenschein et al., 1999).

The traditional field approach first estimates AGB within representative plots, which are then extrapolated across broader geographic areas to estimate total AGB (see Fig. 5.1). Field studies are time consuming and expensive (Lutz et al., 2008), which may limit the number and thoroughness of plot AGB estimations. Trees commonly represent the greatest concentration of AGB and can be measured efficiently. This often leads to plot estimates being restricted to tree AGB to ensure rapidity and coverage. The exclusion of smaller vegetation inevitably underestimates the total AGB within a plot.

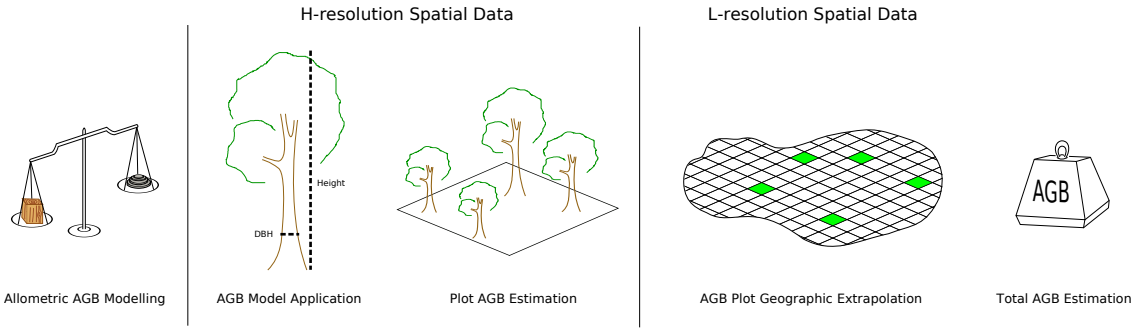

Figure 5.1: Workflow for field-based AGB estimation. Allometric model is constructed and applied to calculate the AGB of species. The total AGB within plots are calculated and used to extrapolate a total AGB across a suitable geographic area. The stage of incorporating remote sensing is limited by the relationship between image resolution and size of ground features. H-resolution data may provide allometric parameter measurement, allowing remote sensing to implemented during application of allometric models and during plot AGB estimation. Coarser L-resolution lacks allometric parameters, limiting it's involvement to the extrapolation stage.

Total AGB estimates are further undermined by the lack of standard allometric models, variability between different field surveys, and variation in species morphology with environmental clines. This variation creates additional uncertainty when extrapolating AGB estimates consistently over changing topography and climatic conditions (Lutz et al., 2008). Remote sensing techniques are critical for consistent fine-scale biomass estimation over broad spatial extents (Clark et al., 2011; Ahmed et al., 2013; Anaya et al., 2009).

5.2.2 Biomass - Remote Sensing Techniques

Remote sensing provides the spatially contiguous measurements that are key for broad-scale AGB modelling. Landscape metrics can be integrated into an analysis to improve AGB extrapolation over broad geographic areas. LiDAR and optical remote sensing for AGB estimation are well established (Roy and Ravan, 1996; Lu, 2006; Lutz et al., 2008; Anaya et al., 2009; Clark et al., 2011; Shrestha and Wynne, 2012). Allometric parameters for tree AGB modelling have been directly estimated from 3D point clouds generated from

airborne LiDAR (Drake and Knox, 2003; Dubayah et al., 2010; Chisholm and Cui, 2013). Furthermore, the capacity for multi-return LiDAR to partially penetrate canopy layers (Anaya et al., 2009) can reveal vegetation structure beneath the canopy (Shrestha and Wynne, 2012; Clark et al., 2011).

Conversely, optical remote sensing has traditionally modelled AGB indirectly using spectral properties. Optical AGB models rely upon correlating spectral reflectance with biomass measurements. The major limitation of an optical approach has been its restriction to a 2D horizontal plane (Shrestha and Wynne, 2012; Anaya et al., 2009), excluding important 3D structural allometric parameters (Drake and Knox, 2003). Furthermore, dense canopies may block optical measurements, hiding lower vegetation strata (Anaya et al., 2009). The absence of structural information has limited the direct application of accurate allometric AGB models from optical data. Recent advancements in computer vision, however, have led to stereopsis techniques that can derive 3D structural information from optical imagery.

Structure-from-motion (SfM) generates a fine-scale 3D point cloud from overlapping optical data (Westoby et al., 2012). SfM first identifies Scale Invariant Feature Transform (SIFT) features. SIFT features are region features which are invariant to geometrical transformations (Lingua et al., 2009; Wallace et al., 2012). SfM extracts a 2D vector for each SIFT feature within an image. By identifying multiple occurrences of individual features across overlapping images, 2D SIFT features can be transformed into a 3D space by estimating the intersection of vectors (Fonstad et al., 2013). Using SfM techniques, optical remote sensing can benefit from both the radiometric resolution of an optical system as well as the 3D structural information previously limited to LiDAR. SfM techniques, however, require a high degree of image overlap ($\approx$80%) (Berni and Zarco-Tejada, 2009) and lack the multi-return structure of LiDAR.

5.2.3 Allometric Parameters & Remote Sensing Scale

Image spatial resolution defines the scale of samples. There are two distinctions in image sample scale with regard to the observation of image features: H-resolution and L-resolution (Strahler et al., 1986). Within H-resolution imagery, the size of features exceeds the sample resolution. Features are represented by multiple pixels which provides a distinct geometric delineation. Conversely in L-resolution, image features are smaller than the sample scale, which leads to features without a geometric definition beyond an individual pixel. The relationship between sample and image feature scale determines the feasibility of deriving allometric parameters including geometric properties (Wulder, 1998). It therefore also restricts the role of remote sensing within AGB modelling (see Fig. 5.1).

H-resolution is the ideal image scale for direct AGB modelling, whereby relevant allometric parameters become measurable. This traditionally has not been the case, however, with early satellite and airborne sensors dominated by L-resolution data (Eckert, 2012). The inability to measure allometric parameters shifted remote sensing AGB estimation to broader vegetation community scales. Models derived from field-based plot estimations of total AGB are linked spatially with spectral characteristics (Ahmed et al., 2013). However, this approach increases uncertainty within the model by relying upon spatially generalised L-resolution parameters, coarse and inconsistent field plot estimations of overall biomass, and the inherent spatial and temporal uncertainty of linking the two different types of measurements (Lutz et al., 2008).

Technological advances are shifting remote sensing technology towards H-resolution data, increasing the spatial separability of features within vegetation communities. As geometric delineations of individual plants become measurable, the direct application of allometric models becomes viable (Wulder, 1998; Lutz et al., 2008). H-resolution can be integrated earlier within AGB modelling process, replacing or eliminating the need

for generalising field plot biomass (Ahmed et al., 2013). However, the sampling scale of established remote sensing platforms continues to limit the analysis of smaller vegetation (diameter <1 m). The recent advent of unmanned aircraft systems (UAS) introduces a new paradigm in the sampling scale of remote sensing.

UAS are small, semi-autonomous unmanned aircraft capable of operating as a remote sensing platform. Their low operational height (<100 m) generates data at ultra-fine spatial resolutions (<10 cm). The controllable flight path and rapid image generation makes the UAS ideal for generating large datasets of overlapping imagery suitable for SfM techniques. This combination of ultra-fine spatial resolution and 3D structure makes UAS remote sensing potentially valuable for measuring the allometric parameters of small scale vegetation. The potential of UAS monitoring of small scale vegetation is already being explored for precision agriculture (Primicerio et al., 2012; Zhang and Kovacs, 2012; Lelong, 2008) and natural environments (Laliberte et al., 2010; Lucieer et al., 2011).

5.2.4 Study Goal

The goal of this study is to investigate UAS optical remote sensing for the AGB estimation of the saltmarsh shrub species *Tecticornia arbuscula*. The study specifically explores the potential for UAS to advance shrub AGB estimations by modelling shrub structure beyond a single volumetric shape (Ludwig et al., 1975; Murray and Jacobson, 1982). Instead, this study attempts to follow more accurate shrub AGB models that focus upon individual stems (Rosenschein et al., 1999). This is achieved by utilising both SfM and geographic object-based image object analysis (GEOBIA) to spatially de-construct shrubs into candidate stems. This deconstruction relies upon allometric modelling of *Tecticornia sp.* stem structure to validate the likelihood of a segmented object representing a *Tecticornia sp.* stem.

5.3 Methods

5.3.1 Study Site

Saltmarsh develops within saline riparian or coastal areas that are sheltered from high energy, scouring waves. Saltmarsh provides a buffer between land and water, accumulating sediments and organic nutrients from terrestrial runoff. Periodic tidal inundation provides a regular redistribution of these materials. Waterlogging creates anaerobic soil conditions, which limits the establishment of vegetation. Vegetation species are distributed along saline and drainage gradients, which in turn are strongly influenced by the local topography. The selected site for this study was a corridor of cold-temperate saltmarsh vegetation at Ralphs Bay in Tasmania (see Fig.5.2).

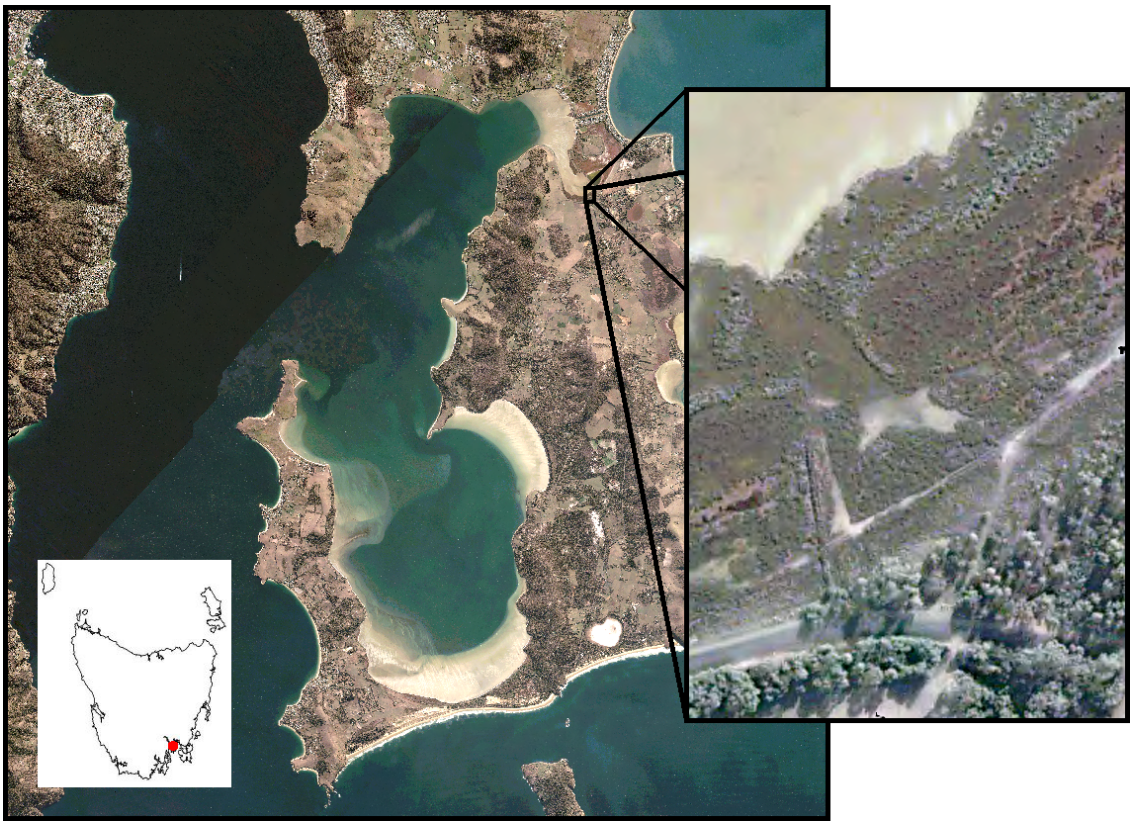

Figure 5.2: Study site - Ralphs bay, Racecourse flats saltmarsh (42 °55′43.29”S, 147 °29′24.29”E)

Saline and drainage gradients within the study site have excluded larger canopy species. Vegetation strata above groundcover was dominated by a single salt-tolerant succulent woody shrub *Tecticornia arbuscula*. The remaining species are classed as groundcover, which was dominated by four species (see Fig.5.3). *Sarcocornia blackiana* and *Sarcocornia quinqueflora* (collapsed to a single class *Sarcocornia sp.*) occupied low topographic areas of increased saltwater inundation. Salt-stress on *Sarcocornia sp.* results in strong anthocyanin pigmentation. In higher topographic areas with protection from inundation and improved drainage, *Tecticornia sp.* shrubs replace *Sarcocornia sp.*. Areas further back from the shoreline are more sheltered from salt-spray and inundation, and were occupied by sedges and grasslands. Within the corridor, this area was dominated by *Gahnia filum*. The topographically lowest areas are free of vegetation. Non-vegetation areas represent sand, exposed underlying organic mudflats, or saltpans formed by pooling saline water.

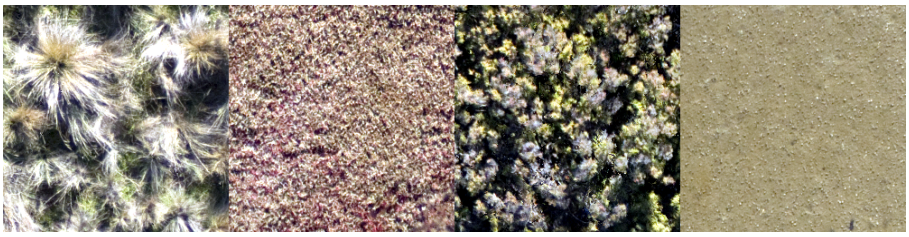

Figure 5.3: The four groundcover classes present within the saltmarsh corridor.

5.3.2 Field Data Collection

Field sampling of the study site was undertaken to collect ground control points, vegetation heights and shrub allometric parameters for AGB estimation (see Fig.5.4). Ground control points were established by using high visibility fluorescent metal disks distributed pre-flight throughout the study site. The spatial location of each ground control disk was recorded using a Leica real-time kinematic (RTK) differential GPS receiver. A transect was run along the centre of the study site corridor to record *Tecticornia sp.* shrub heights. Vegetation height for each shrub bisected by the transect was measured at its

highest point using a survey staff, and its spatial location recorded using a GPS receiver. Ultra-fine spatial resolution data (1 cm pixel size) was collected of the study site using an OktoKopter UAS platform (see Chapter 2). The UAS was flown in two parallel paths along the study site corridor. Data was captured using a Canon EOS 550D digital camera.

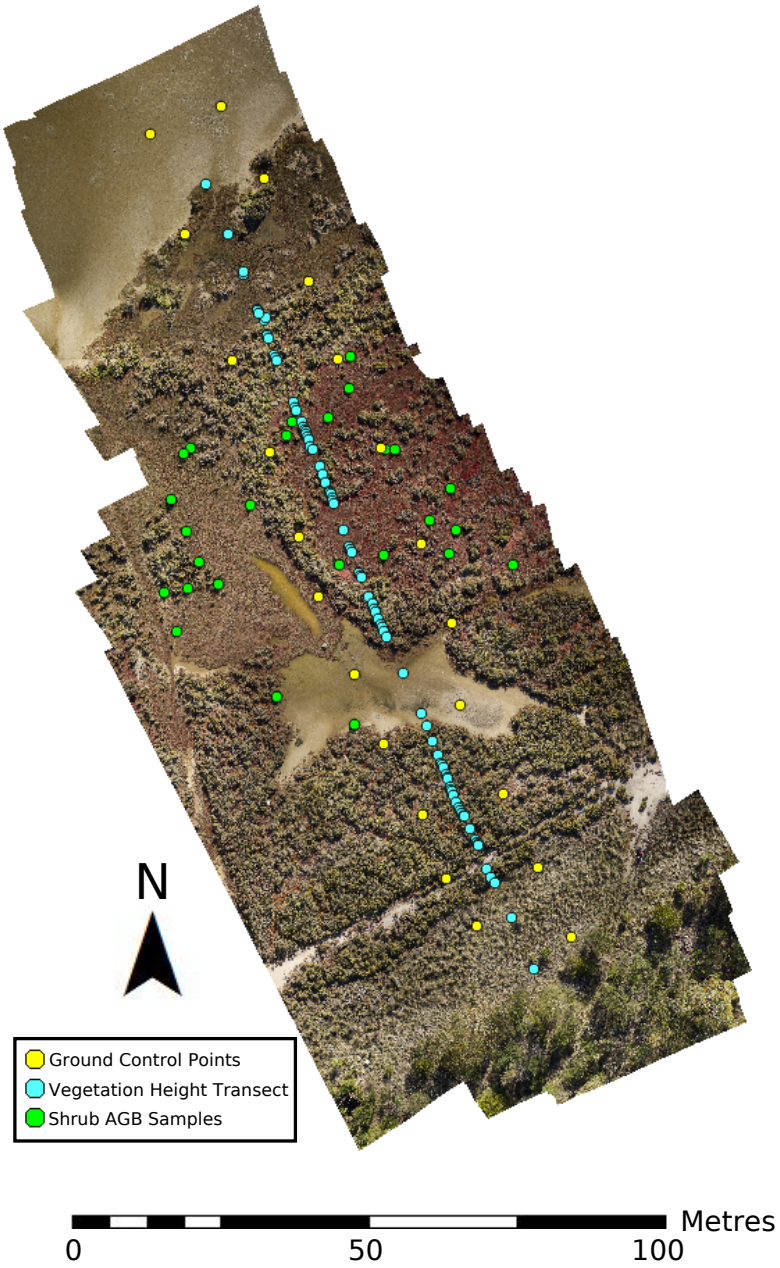

Figure 5.4: UAS orthophoto detailing field sampling collection. Data collected includes ground control .

5.3.3 Allometric Field Sampling

Destructive sampling was employed to derive allometric parameters to estimate *Tecticornia sp.* AGB. Two parallel transects were established along the study site corridor. *Tecticornia sp.* stems were collected from random shrubs along the two pathways. Only a single stem was taken from any given shrub, and a minimum estimated distance of 2 m between shrubs was set to ensure the spatial independence of samples. Stems were taken from a mixture of positions within the shrub to ensure a representation of centre and edge stems.

5.3.4 UAS 3D Point Cloud Derivation

A workflow was developed for estimating small-scale shrub AGB using UAS remote sensing (see Fig.5.5). A preliminary visual assessment of each individual UAS image was conducted to identify and discard blurred imagery. The remaining data were geotagged with an approximate position of image capture extracted from the on-board UAS GPS. The Agisoft Photoscan[1] software package utilises SfM digital image processing to generate 3D point clouds and orthophotos from overlapping data. Image data were aligned at a 'High' accuracy setting and a 3D point cloud of the study site corridor was generated. The pointcloud was georeferenced using the established ground control points. A 1 cm orthophoto and a high density point cloud were generated using Photoscan.

[1] http://www.agisoft.ru/

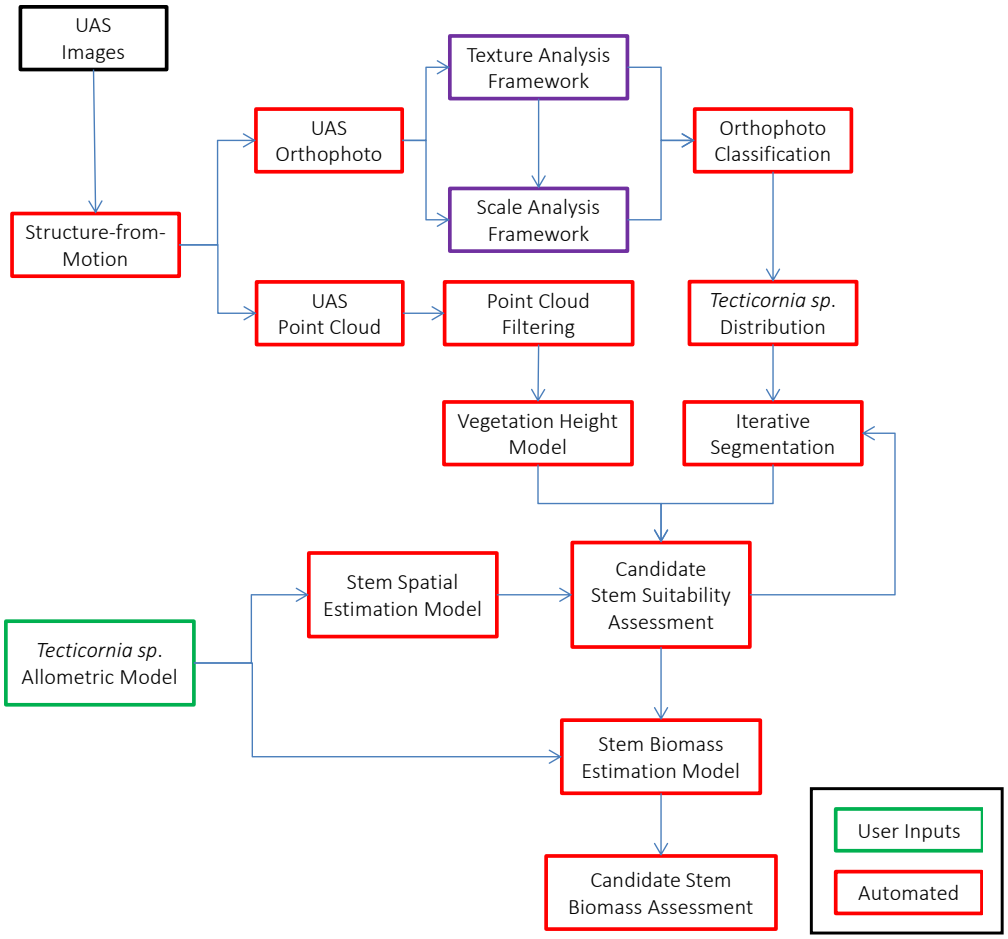

Figure 5.5: Workflow for the GEOBIA segmentation of *Tecticornia sp.* into candidate stems, and the calculation of stem AGB.

5.3.5 UAS Image Classification

The orthophoto was thematically classified into four different classes: *Tecticornia sp.*, *Sarcocornia sp.*, *Gahnia sp.* and non-vegetation. The classification of ultra-fine spatial resolution UAS data was achieved using a two-step approach encompassing a texture analysis (see Chapter 3) and a GEOBIA scale analysis framework (see Chapter 4). A texture analysis framework was implemented to compare relevant texture models and metrics. Class-specific texture metrics were identified and generated for the full image. A GEOBIA scale analysis framework incorporated the results of the texture analysis framework to identify class-specific relative scales of image segmentation. The full image

was segmented at each of the identified relative scales, and the corresponding image object's class probabilities were calculated using a Random Forest ensemble classifier. The probability layers were collapsed to provide a final thematic classification map.

5.3.6 Point Cloud Filtering & Vegetation Height Extraction

To extract vegetation heights, measurements of the bare Earth height were required. This in turn required the identification of points in the cloud that represented bare Earth measurements. Bare Earth points were extracted from the point cloud by using point cloud filtering (Vosselman and Gorte, 2004). Filtering algorithms measure discontinuities between the bare Earth and object surfaces (i.e. vegetation) (Sithole and Vosselman, 2003, 2005). This was used to classify individual points as bare Earth.

BCAL[2] is an open source LiDAR toolkit developed by the Boise Centre Aerospace Laboratory, from which it takes its name. The BCAL package was implemented through the ENVI remote sensing software package[3]. The high density point cloud was imported into BCAL for vegetation height filtering. The point cloud LAS data was first decimated to reduce the dataset to 1% of the original point count, to reduce data size and improve processing speed. A total of 11 height algorithms were tested for filtering the point cloud: inverse distance (1st, 2nd & 3rd order), inverse multiquadratic, linear, natural & nearest neighbours, cubic & thin plate splines, polynomial regression (2nd & 3rd order). For each algorithm, five canopy spacings were tested: 0.5, 1, 1.5, 2, and 2.5 m.

The height filtering algorithms were used to classify points, with identified ground points extracted as a separate LAS file. The original and ground-point LAS files were both imported into the ArcGIS software package. Kriging is a geostatistical approach to raster interpolation, and was used to generate a digital surface model (DSM) using the complete 3D point cloud. A DEM was generated for each of the algorithms from the classified bare

[2]http://bcal.boisestate.edu/tools/lidar
[3]http://www.exelisvis.com/

ground points. Vegetation heights were extracted as the spatial height difference between the DEM and the DSM, and stored as a canopy height model (CHM). The accuracy of each CHM was validated using the transect *Tecticornia sp.* heights.

5.3.7 Allometric Modelling

This study closely follows the allometric modelling framework presented in the work of Picard et al. (2012). Picard et al. (2012) provides a comprehensive approach to allometric modelling, thoroughly covering field sampling, data exploration, model construction and validation. *Tecticornia sp.* stem parameters of height and crown perimeter were selected as both are potentially measurable at the sample scale of UAS remote sensing (see Fig.5.6). Stem length was measured from the woody base to the top of the stem's photosynthetic crown. The perimeter of the stem was measured using the maximum transverse crown perimeter. Stem biomass was dried in an oven at 65 °C, and weighed to derive AGB dry weight.

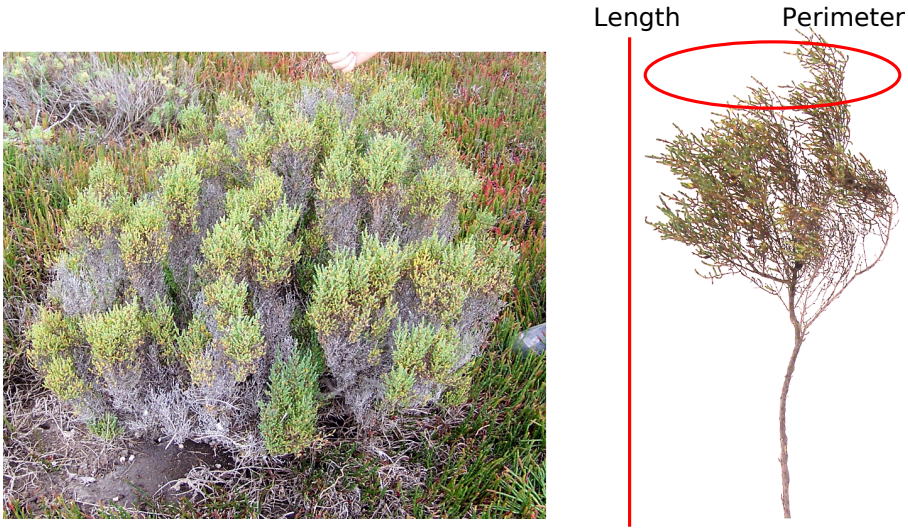

Figure 5.6: *Tecticornia sp.* exhibiting typical shrub morphology and a single shrub stem illustrating allometric parameter measurement.

Tecticornia sp. AGB estimation was implemented as a two-stage process: the first stage attempts to de-construct shrubs into candidate stems, while the second stage estimates

the AGB of candidate stems. The analysis is spatially constrained to the distribution of *Tecticornia sp.* identified within the thematic classification.

The allometric relationship between stem height and perimeter was linearly modelled using the R statistical package. The eCognition software package was used to segment classified regions of *Tecticornia sp.* into image objects. For each image object, the height was extracted from the CHM. Using the linear model, an estimated perimeter length was calculated for a stem of the extracted CHM height. The perimeter of each object was then calculated from boundary length, and compared against the perimeter estimated by the linear model. The difference in length between the objects perimeter and the models estimate is referred to in this work as the stem-residual. The larger an object's stem-residual becomes, the less likely that the object represents a stem. A residual threshold value is used to assess the likelihood of image objects representing a stem. Image objects with a stem-residual within the defined threshold are considered stems.

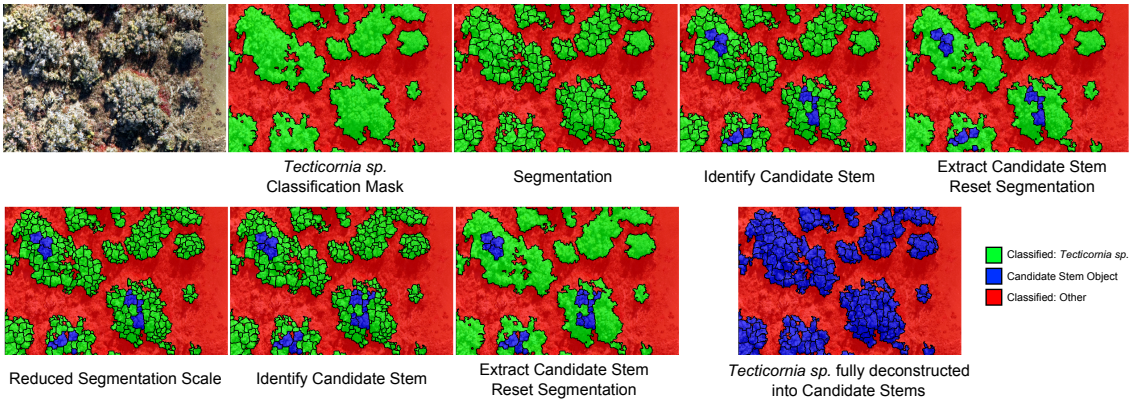

Figure 5.7: Iterative segmentation process to identify candidate stems within *Tecticornia sp.*. The process is a top-down segmentation iteration and attempts to identify candidate stems that fit a pre-constructed stem allometric model. Objects must fall within a predefined residual threshold to be accepted as a candidate stem. This process is further nested within a broader iterative residual process, which successively relaxes the residual threshold until all *Tecticornia sp.* classified areas have been segmented into candidate stems.

The residual threshold begins at zero. The process slowly iterates by gradually increasing

this threshold. At each residual threshold level, *Tecticornia sp.* is iteratively segmented from large to small image objects. At each segmentation level, image objects are assessed by calculating its stem-residual and comparing it against the residual threshold. Objects falling within the threshold are identified as candidate stems, and are excluded from further segmentation. This process continues until all the classified *Tecticornia sp.* areas have been spatially de-constructed into candidate stems (see Fig.5.7).

Biomass estimation of the candidate stems was achieved by constructing a linear allometric relationship between dry weight, stem height and perimeter using the R statistical program. The potential to transform stem height and perimeter into a single parameter was explored. Tested transformations were cone and cylinder volume. Cone and cylinder volumes were extracted by using perimeter as an estimate of circumference. Estimations of AGB dry weight were then estimated for the segmented candidate stems.

A second field trip to the study site was conducted after the allometric AGB model had been constructed. This second field trip estimated the AGB of spatially discrete shrubs to validate the remote sensing measurements. Spatially discrete validation shrubs were selected, and the length and perimeter of each stem was measured. AGB estimates were extracted for each stem using these parameters, and the total AGB of each shrub was calculated. A comparison of AGB was made between field-based and UAS-based parameter measurement.

5.4 Results

5.4.1 Data Collection

An OktoKopter UAS was flown over the study site at a height of 50 m (see Table 5.1). A total of 365 images were generated using an on-board Canon EOS 550D. A visual qualitative assessment of image quality was conducted on the initial 365 images. A total of 175 images were identified as poor quality and discarded. Factors of poor image quality

included image blur and low altitude. The remaining 190 images were geotagged using the on-board UAS GPS. Geotagged images were imported into Agisoft PhotoScan and a point cloud was generated using SfM. A high density point cloud and a 1 cm spatial resolution orthophoto were generated of the study site, capturing the structure of *Tecticornia sp.* shrubs (see Fig.5.10). The high density point cloud contained a total of 95,825,647 points at 9,126 per m^2. The spatial RMSE of the georeferenced orthophoto was measured at 0.166 cm.

Table 5.1: Data Collection Details

Date	UAS Images	Bands	GCPs	Height Samples	Stem Clippings
23 May, 2013	365	3	23	22	40

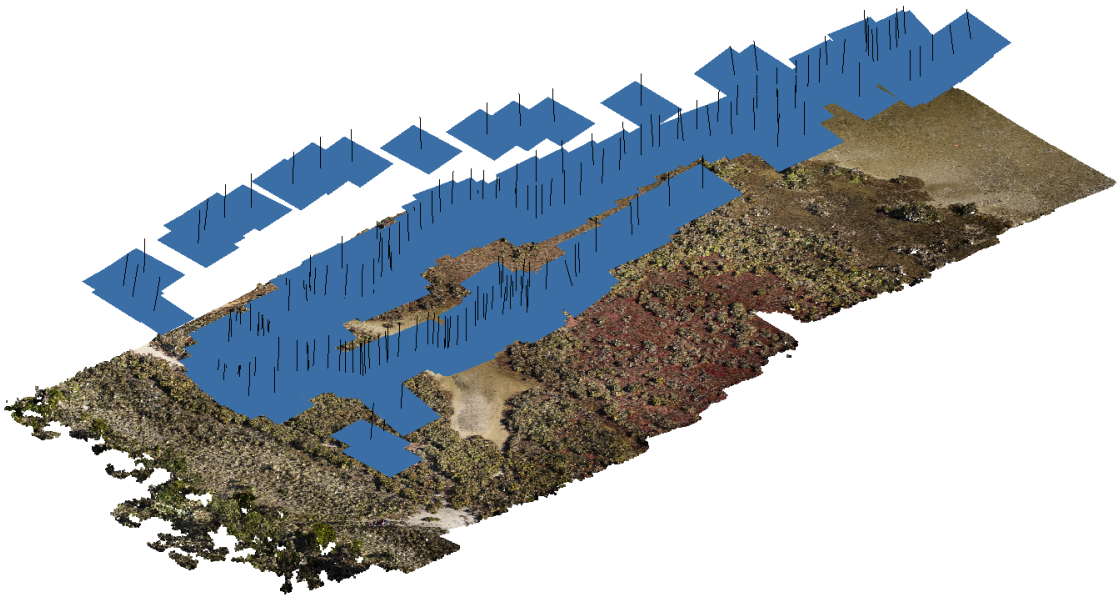

Figure 5.8: Image of PhotoScan generated high density point cloud and image capture location, providing an illustration of image number and overlap involved in data construction.

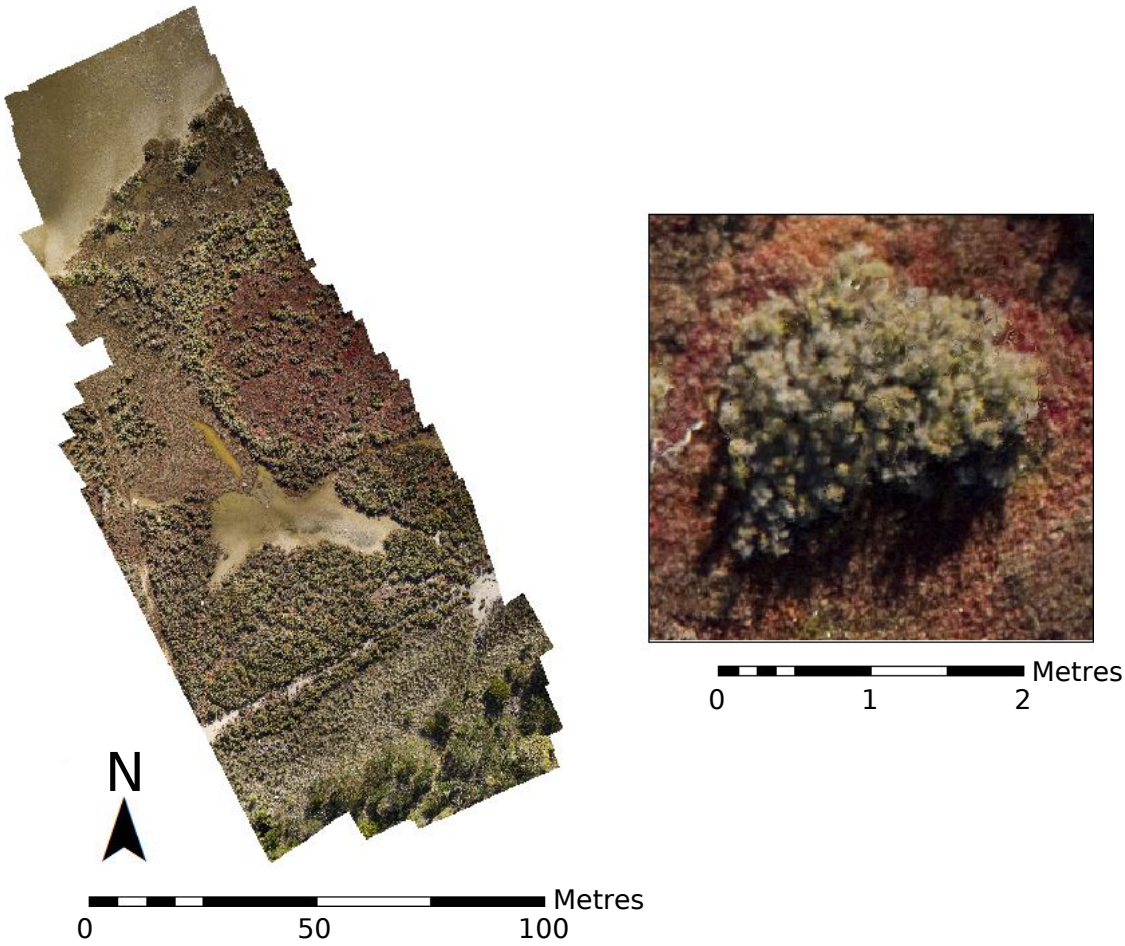

Figure 5.9: Image of coloured point cloud, orthophoto and close-up of *Tecticornia sp.* shrub.

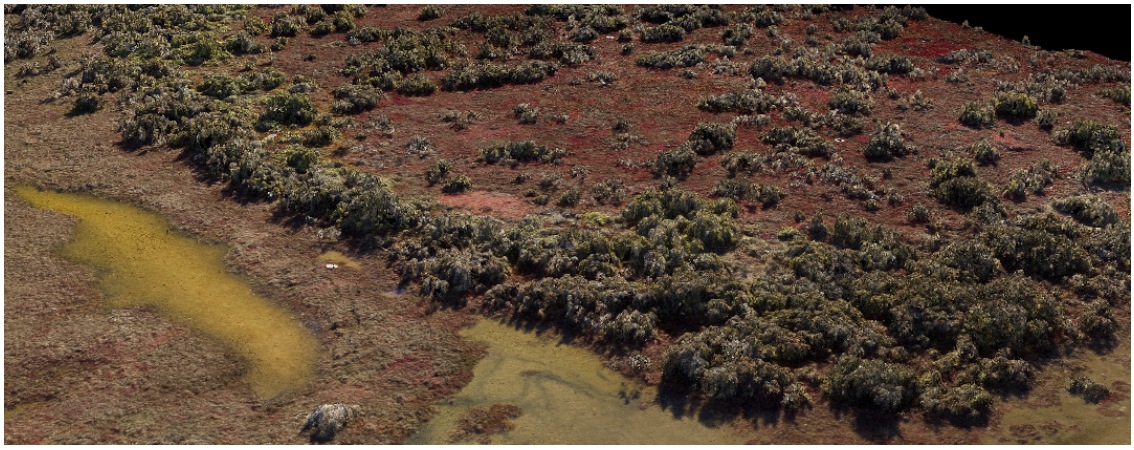

(a) Illustration of the high density pointcloud representation of *Tecticornia sp.* shrubs.

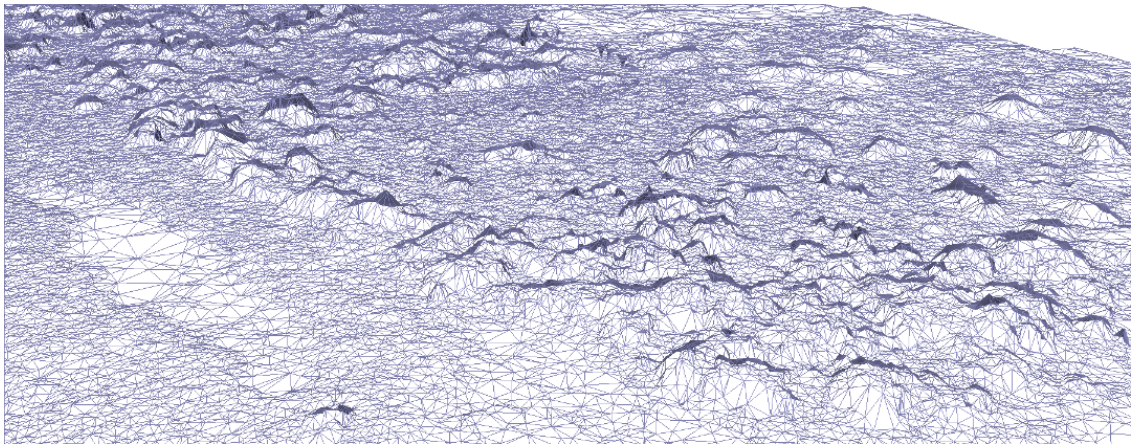

(b) Coarse wireframe illustration of *Tecticornia sp.* shrubs volumetric structure.

Figure 5.10: High density pointcloud and coarse wireframe to illustrate the 3D volumetric structure of *Tecticornia sp.* shrubs derived from UAS data using SfM.

5.4.2 Pointcloud Filtering

The high density point cloud was decimated using BCAL to 1% (958,256 points) to improve processing times for detection of ground points. Algorithms were validated based upon the RMSE between the filtering algorithms CHM and the collected field transect heights. Table 5.2 contains the RMSE results for the 11 height filtering algorithms at 5 different canopy spacing. RMSE results ranged between 10.56 cm for Cubic Spline to 5.87 cm for Natural Neighbour. The selection of filtering algorithm was more important than canopy spacing. The CHM generated using the Natural Neighbour algorithm at a

canopy spacing of 1.5 m produced the lowest RMSE (5.87 cm) and was selected for further processing (see Fig.5.11).

Table 5.2: RMSE (cm) of BCAL Vegetation Filtering Algorithms at 5 different canopy settings.

Canopy Spacing (m)	Cubic Spline	Inverse Distance 1st Order	Inverse Distance 2nd Order	Inverse Distance 3rd Order
0.5	8.67443	7.52561	7.52529	7.44068
1	10.5678	6.17369	6.12353	6.07967
1.5	7.25975	6.04879	5.85583	5.96031
2	7.06737	6.03597	6.04003	6.04177
2.5	6.38361	6.41742	6.40906	6.418

	Inverse Multiquadratic	Linear	Natural Neighbour	Nearest Neighbour
0.5	10.0335	7.39815	7.39815	7.57413
1	6.87072	6.09932	6.10375	7.16168
1.5	6.67518	6.02532	5.875	6.37192
2	6.50852	5.85169	6.04026	6.69287
2.5	6.94914	6.40704	6.40704	7.14866

	Polynomial 2nd Order	Polynomial 3rd Order	Thin Plate Spline
0.5	10.4715	8.79532	9.25942
1	9.41977	6.93369	9.80486
1.5	8.76845	6.06057	10.0465
2	8.00743	7.72037	9.27143
2.5	7.37749	8.82688	6.99142

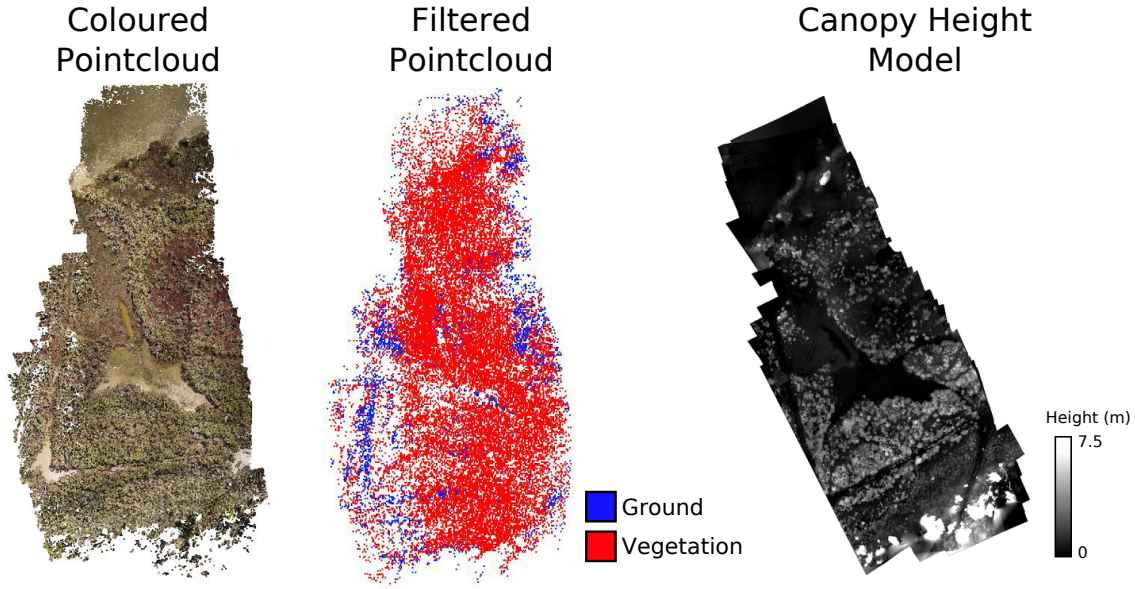

Figure 5.11: Coloured and classified point clouds, and the resulting canopy height model.

5.4.3 Image Classification Framework

Class specific texture metrics were identified by implementing a random-forest based texture selection framework (see Table 5.3). The number of texture metrics was linked with the spatial complexity of the class, with *Gahnia sp.* and *Tecticornia sp.* both requiring 4 and 3 texture metrics respectively. The remaining *Sarcocornia sp.* and non-vegetated classes, which lack the spatial complexity of the previous two classes, only required a single texture metric.

Table 5.3: List of the class-specific texture metrics identified by the texture selection framework.

Gahnia sp.	*Sarcocornia sp.*	*Tecticornia sp.*	Non-Vegetation
FO: Green Mean K19	FO: Green Var K25	GLCM: Red Cont K23	GLCM: Red Hom K19
FO : Blue Var K23		GLCM: Green Mean K17	
GLCM : Red Cont K25		GLCM: Red Corr K25	
GLCM : Blue Cont K25			

The optimal relative scale of segmentation was identified for each of the four classes by testing for both over- and under-segmentation using a GEOBIA framework (see Fig.5.12). In an assessment of the vegetation classes, the inclusion of texture metrics increased the overall classification accuracy for both *Tecticornia sp.* and *Gahnia sp.*. *Sarcocornia sp.* only benefits from texture within a segmentation window between approximate scales of 70 and 85. Class-specific probability layers were calculated from the relative scales of segmentation using random-forest and collapsed into a final thematic classification for the site (see Fig.5.13). Table 5.4 contains the class-specific optimal relative scale of segmentation and resultant spatial accuracy and Table 5.5 contains the thematic accuracy assessment. The distribution of *Tecticornia sp.* was extracted as a binary mask layer that was used to spatially restrict further analysis to the distribution of *Tecticornia sp.* vegetation.

Figure 5.12: Effect of segmentation scale and texture metric inclusion upon class subset separability.

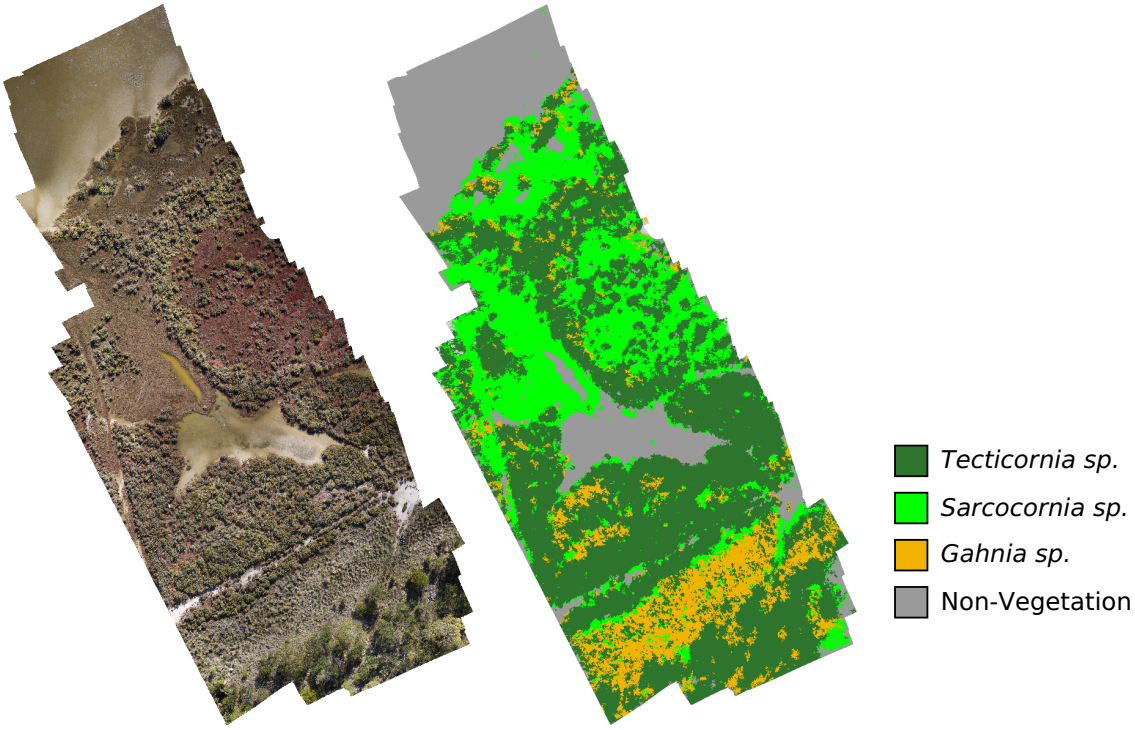

Figure 5.13: Final classified saltmarsh corridor UAS image.

Table 5.4: List of the final identified class-specific segmentation scales identified by the GEOBIA framework, and the corresponding spatial accuracy.

Class	Seg.Scale	Spatial Acc.
Gahnia sp.	88	0.897
Sarcocornia sp.	74	0.955
Tecticornia sp.	44	0.974
Non-Vegetation	42	0.979

Table 5.5: Saltmarsh classification confusion matrix (%).

Class	*Gahnia sp.*	Non-Vegetation	*Sarcocornia sp.*	*Tecticornia sp.*
Gahnia sp.	0.733	0.000	0.020	0.053
Non-Vegetation	0.000	0.960	0.013	0.000
Sarcocornia sp.	0.000	0.033	0.893	0.007
Tecticornia sp.	0.267	0.007	0.073	0.940
Overall Accuracy	0.882			

5.4.4 *Tecticornia sp.* Stem Allometric Spatial Modelling

A total of 40 *Tecticornia sp.* stems were collected from across the study site. Stem length and the maximum perimeter of the photosynthetic crown were measured. The stems were dried and their dry weight was measured. The relationship between stem length and perimeter was statistically explored. The model exhibited a heteroscedastic power relationship, with increasing residuals as stem size increases (see Fig.5.14). Both length and perimeter were log-transformed to linearise the power relationship and reduce heteroscedasticity (Ahmed et al., 2013). Table 5.6 provides a comparison of stem length and perimeter model between non-transformed and log-transformed data.

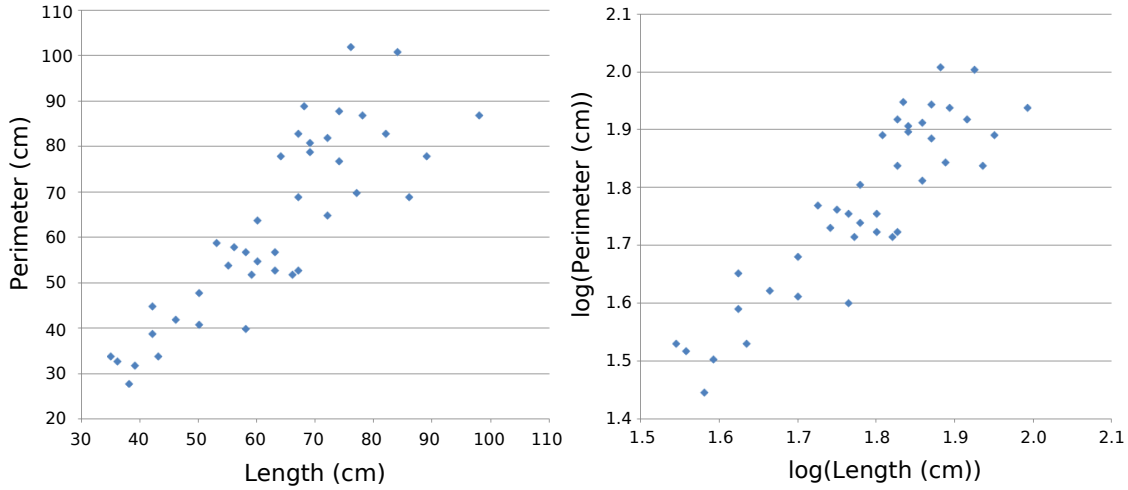

(a) Linear relationship between length and perimeter

(b) Linear relationship between log transformed length and perimeter

Figure 5.14: Scatterplots illustrating the relationship between *Tecticornia sp.* stem perimeter and length. Log transformation decreases heteroscedasticity.

Table 5.6: Comparison of the effects of untransformed and log-transformed perimeter and length upon the construction of a linear model.

Perimeter Linear Model	R2	Adjust.R2	P(yInt)	P(Ind)
$P = 1.1187 * L - 7.6087$	0.7286	0.7215	0.293	2.58e-12
$log(P) = 1.1874 * log(L) - 0.7960$	0.7984	0.7931	0.0528	8.75e-15

An initial residual threshold was set to 0, and data was iteratively segmented. The stem-residual was calculated for segmented objects and compared against the residual threshold to identify candidate stems. The segmentation process was re-iterated with increasing residual threshold until all areas of *Tecticornia sp.* were segmented into candidate stems. Candidate stems with the lowest stem-residuals commonly occurred within central areas of *Tecticornia sp.* shrubs, while the highest stem-residuals occurred in misclassified areas between shrubs.

5.4.5 *Tecticornia sp.* Stem Allometric AGB Modelling

The linear relationship between stem dry weight and its parameters were explored to identify the strongest predictor of dry weight. Explored parameters were perimeter, length, cone volume and cylinder volume. All models illustrated a power relationship with heteroscedastic residuals, and benefited from a log transformation to linearise the relationship. The strongest fitting dry weight model was the log-transformed cone volume (see Fig.5.15), while the poorest was the relationship between stem length and dry weight (see Table 5.7). The model between dry weight and perimeter maintained high heteroscedascity even after data transformation.

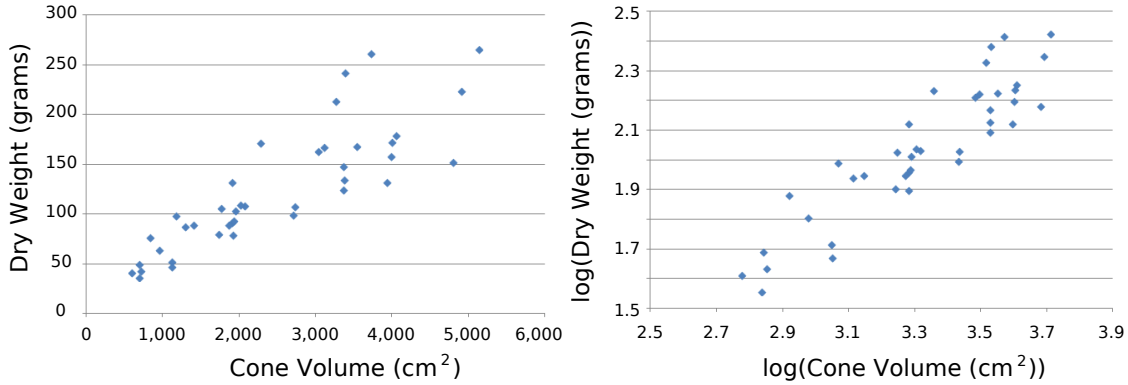

(a) Linear relationship between dry weight and cone volume

(b) Linear relationship between log transformed dry weight and cone volume

Figure 5.15: Scatterplots illustrating the relationship between *Tecticornia sp.* stem dry weight and cone volume. Log transformation decreases heteroscedasticity.

Table 5.7: Comparison of the dry weight linear model parameters: length, perimeter, cylinder volume, and cone volume.

Dry Weight Linear Model	R2	Adjust.R2	P(yInt)	P(Ind)
$log(DW) = 1.7263 * log(L)$ - 2.3926	0.7493	0.7427	0.00093	5.64e-13
$log(DW) = 1.3434 * log(P)$ - 0.7848	0.8014	0.7961	0.0852	6.58e-15
$log(DW) = 0.50504 * log(Cyl)$ - 0.22023	0.8217	0.817	0.558	8.32e-16
$log(DW) = 0.77948 * log(Cone)$ - 1.26616	0.8235	0.8189	0.00759	6.87e-16

The R statistical package was used to construct a linear model between log-transformed dry weight and conical volume. Parameters of the segmented candidate stems were extracted, and a dry weight was estimated at 95 % confidence (see Fig.5.16). The model estimates the total dry weight of classified *Tecticornia sp.* to be between 3,440.77 and 4,482.77 kg for the study area. Closer inspection of candidate stems recording the highest residuals reveals areas of misclassification, whereby the structure of *Sarcocornia sp.* groundcover is fitted with the *Tecticornia sp.* shrub allometric model.

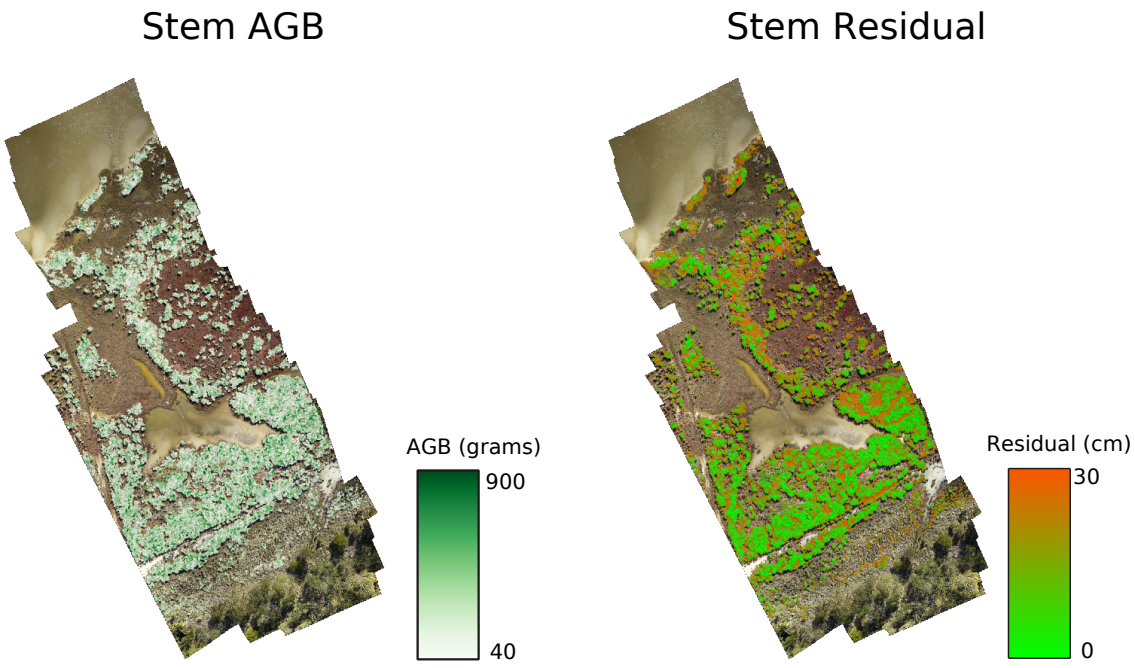

Figure 5.16: Distribution of AGB within the study site corridor, with the associated stem-residual of candidate stems.

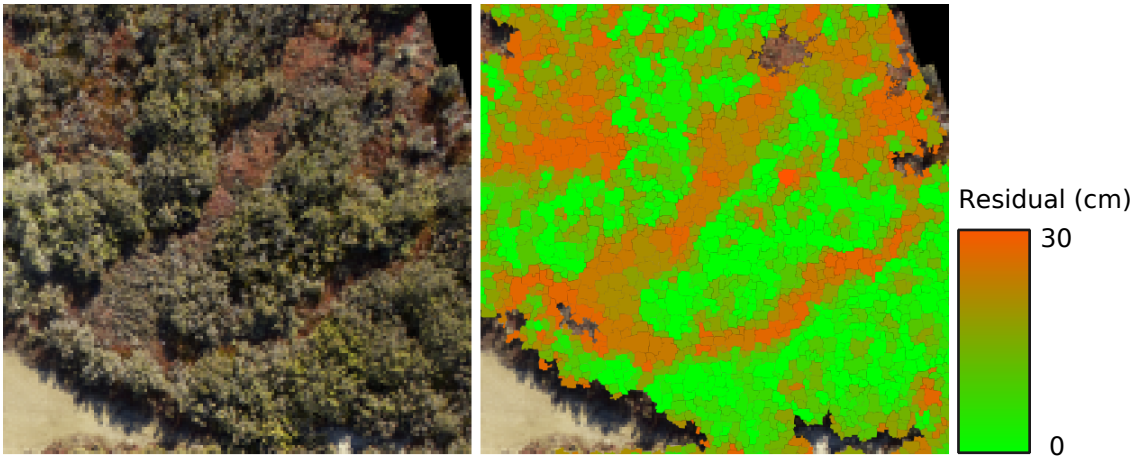

Figure 5.17: Misclassified areas of the groundcover species *Sarcocornia sp.* resulting in a poor fit to *Tecticornia sp.* allometric model.

5.4.6 Field vs. UAS AGB Allometric Parameter Measurement

The field modelled estimates of the validation shrubs were compared against the UAS modelled estimates. Figure 5.19 illustrates both the stem count for individual shrubs

utilising UAS and field measurements, and the respective estimates of AGB of individual shrubs. The largest recorded deviation in the stem count for shrubs was 13. A trend exists within the stem count, with an increasing deviation as shrub size increases. This trend is not reflected in the estimation of shrub AGB between UAS and field measurements. The furtherest deviation of AGB estimate was by 1,112.47 grams, while the closest was deviated by only 27.922 grams.

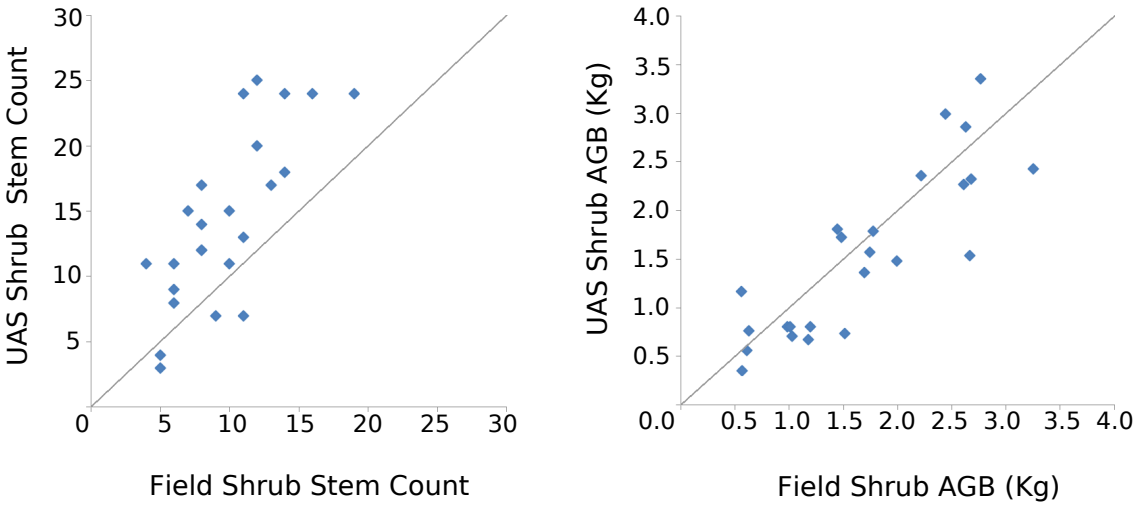

Figure 5.18: Scatterplots of validation shrubs illustrating the relationship between UAS estimate and field count of shrub stems, the the final estimate of the AGB of a shrub using UAS parameter measurements against field measurements.

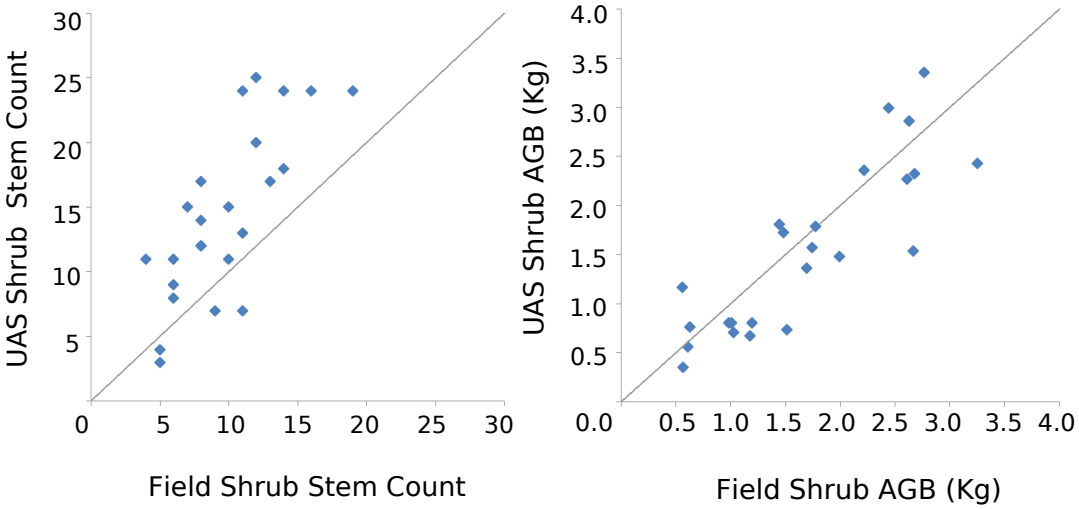

(a) Relationship between field and UAS estimates of shrub stem count

(b) Relationship between field and UAS estimates of shrub AGB

Figure 5.19: Scatterplots of validation shrubs illustrating the relationship between UAS estimate and field count of shrub stems, and the final estimate of the AGB of a shrub using UAS parameter measurements against field measurements.

5.5 Discussion

This study estimates the AGB of *Tecticornia sp.* within the study site corridor is between 3,440.77 and 4,482.77 kg. To provide a very coarse comparison, this is approximately the same amount of biomass expected from a large tree with a 70 - 90 cm DBH (Jenkins et al., 2003). While *Tecticornia sp.* is not regarded as a shrub of rapid growth, other woody shrub species that do exhibit this characteristic may make a significant contribution to carbon accumulation on a temporal scale. This illustrates the problem of AGB underestimation when focused exclusively upon the large centralised biomass storage of tree species, while excluding the potential temporal uptake of smaller plants.

AGB field measures of spatially discrete shrubs were used to validate the UAS AGB estimates. The stem count scatterplot illustrates an increasing error, with an increasing over-estimation of the number of candidate stems within larger shrubs. The stem over-

estimation trend was not evident in the variation exhibited within estimations of AGB (see Fig.5.19). Sources responsible for variation include uncertainty in the UAS data layers used for calculating allometric parameters, the generalisation of stem structure within a shrub to fit UAS measurements, and the spatial discrimination of shrubs using both the classification layer and GEOBIA

A major goal of this study was repeat the success of improved field-based shrub AGB modelling, but by using UAS remote sensing. This was achieved by utilising UAS ultra-fine spatial resolution data to shift the scale of modelling shrub structure from a generalised volumetric shape to individual stems. A linear model for stem structure using CHM height and object boundary length was used to identify candidate stems. The allometric AGB model was implemented by representing stems as lengthwise vertical cones. However the path and orientation of a stem within a shrub is dependent upon light competition and distance from the central base.

Stems centrally positioned within a shrub have a stronger fit to the vertical conical representation than stems positioned along the edge. This may explain the radial-effect exhibited by the stem-residuals within shrubs, which results in the strongest fit occurring in central areas and the weakest towards the edges. The greater the horizontal distance of the stem from its central base, the greater the horizontal curvature required by the stem. To introduce this curvature into the model requires the spatial location of the shrub central base to be known. The lack of information on the internal structure of shrubs, however, limits estimations of this spatial location. This is further compounded in areas of dense, compacted vegetation where the lack of clear shrub delineation masks the number of shrubs. Given the horizontal curvature of stems, implementing the model within this study would be expected to underestimate the length of less-central stems. This in turn would result in an overestimation of the number of stems but an underestimation of their size. This is potentially one of the main sources of variation between the field count and UAS estimation of shrub stems, as well as the lack of this trend transferred to shrub

AGB estimation (see Fig.5.19).

The lack of information on internal shrub structure is a major hurdle for stem modelling. Although SfM can extract a high density point cloud from optical data, it provides only fine-scale surface structure. One solution is to incorporate oblique imagery alongside the traditional nadir perspective to improve the 3D modelling of shrubs. Kattenborn (2014) demonstrated this oblique approach to SfM pointcloud generation using a UAS. This required flying the UAS beneath the canopy to capture oblique imagery. Using this oblique imagery, individual trees were then spatially estimated from SfM point clouds.

Another solution is UAS-based LiDAR using multi-return 3D point clouds to ensure internal measurements of shrub structure. Wallace et al. (2012) demonstrated a low-cost UAS LiDAR platform for the calculation of tree allometric parameters. These LiDAR-based UAS solutions, however, still remain focused on measuring tree parameters. Their transferability to the dense, complex structure of small shrubs is therefore uncertain. Wallace's approach, however, sets the foundation for dual optical and LiDAR sensor systems to fuse fine-scale SfM surface structure with less dense LiDAR measurements for internal vegetation structure and improved representation of the bare ground surface.

5.5.1 The role of Structure in Classification

Structural parameters of shrubs are utilised within this study for the estimation of both the structure and AGB of individual stems. Image classification excluded structural parameters (e.g. height), instead implementing an established GEOBIA approach that utilises both pixel values and texture metrics. Closer examination of the classification results reveals notable misclassification in thin strips of *Sarcocornia sp.* groundcover which separates close neighbouring *Tecticornia sp.* shrubs. The classification process has incorrectly merged these strips into the surrounding shrubbery. This has led to misclassified areas of *Sarcocornia sp.* incorporated into the candidate stem segmentation process (see Fig. 5.17). *Sarcocornia sp.* however, lacks the structural characteristics of *Tecticornia*

sp.. Its fit to the allometric stem model results in notably higher stem-residuals.

This suggests that allometric modelling may play a role in the classification of ultra-fine spatial resolution data. This role may be either the direct incorporation of structure into the classifier or the application of a residual threshold to filter classification results. The results of this study suggest that capping the residual threshold for candidate stems may exclude misclassified vegetation that structurally deviates from the *Tecticornia sp.* model. Improving classification accuracy by incorporating structure will require a methodology to identify this residual threshold cap.

The spatially consistent measurements of remotely sensed data will play a critical role in AGB estimation (Clark et al., 2011). The integration of remote sensing into AGB modelling is restricted by the sampling scale. This study demonstrates the capacity of UAS to generate ultra-fine spatial resolution data at a sample scale appropriate to measure allometric parameters of small-scale shrubs. This allows the UAS to replace time-consuming and inconsistent field-based measurements of allometric parameters. Control of the operational height of UAS allows a balance between parameter measurement and spatial coverage. This allows the UAS to engage in broader spatial scale AGB assessments, or focused plot-estimates to extrapolate to coarser spatial resolution data.

5.6 Conclusion

This study successfully demonstrates the above-ground biomass (AGB) estimation of a small scale shrub using unmanned aerial systems (UAS). Field-based allometric models were constructed to calculate AGB for the saltmarsh shrub *Tecticornia arbuscula*. Ultra-fine spatial resolution UAS data of the saltmarsh study site was classified utilising texture modelling and geospatial object-based image analysis (GEOBIA), and the distribution of *Tecticornia sp.* was mapped. The sample scale of ultra-fine spatial resolution UAS data was used to remotely measure allometric *Tecticornia sp.* model parameters. The allometric

model was used to estimate *Tecticornia sp.* AGB within the study site at between 3,440.77 and 4,482.77 kg.

This study illustrates the AGB contribution of small spatially dispersed vegetation overlooked in favour of larger centralised bodies of AGB. Traditional remote sensing manned aerial platforms collect data at a sample scale too coarse to directly apply accurate allometric models. The UAS platform fits an ideal sample scale niche due to a low operational height to target and derive allometric parameters. The extraction of parameters within this study was highly dependent upon structure-from-motion (SfM) point cloud filtering. This study explored a wide range of filtering algorithms and settings, selecting the Natural Neighbour (canopy spacing of 1.5 m) due to its high performance. However, the increased density and lack of multiple returns within SfM point clouds remains a significant challenge for traditional point cloud filtering.

This study successfully estimated the AGB stores of a small scale saltmarsh shrub utilising UAS remote sensing. This was achieved by exploiting the ultra-fine spatial resolution data generation capability of UAS. The UAS also has a strong capacity for rapid temporal observations. Small scale vegetation is recognised for it's low capacity for AGB storage, and a high capacity for rapid temporal growth and uptake of carbon. The next step for UAS AGB estimation of small scale vegetation is the expansion into this temporal frame.

Thesis Context

The sampling scale of ultra-fine spatial resolution UAS data is applicable to the direct application of allometric modelling. Chapter 5 illustrates the construction of a field-based allometric model for the saltmarsh shrub *Tecticornia arbuscula*. Through the use of SfM and GEOBIA, allometric parameters were extracted from *Tecticornia sp.* shrubs. It was demonstrated that allometric parameters of small-scale vegetation are transferable to the sample scale of UAS observations. This more broadly demonstrates the role of UAS

remote sensing for the accurate and consistent estimations of fine-scale AGB monitoring.

Chapter 6

Conclusion

This thesis outlines the development of an unmanned aircraft system (UAS) for remote sensing of saltmarsh vegetation. This thesis follows a progressive pathway from the processing and correction of raw UAS data, through to advanced techniques of UAS image analysis and finally UAS vegetation modelling. A framework was established to analyse sensor performance of a small multispectral sensor, identify sources of sensor error and apply correction techniques to improve data quality. Frameworks for both texture modelling and GEOBIA were developed to overcome the high spatial variance of UAS data. Allometric above-ground biomass (AGB) modelling was adapted for fine-scale UAS measurements, enabling UAS-based AGB estimation of saltmarsh shrubs. The results demonstrate that UAS are a valuable tool for the monitoring of fine-scale plant communities.

6.1 Preprocessing & Construction

6.1.1 Assess sensor artefacts of a 6-band multispectral UAS sensor and identify physical and electrical sources of data collection errors. Assess existing approaches to the correction of sensor error. Incorporate suitable correction methods into a rigorous framework that is transferable between sensor systems.

The TetraCam Miniature Multiple Camera Array (mini-MCA) is a lightweight, consumer grade 6-band multispectral sensor. Its low weight and low power consumption make it a suitable sensor for UAS remote sensing. Chapter 2 details the development of a sensor correction framework that transforms raw mini-MCA data into corrected digital numbers. The framework successfully analyses, identifies and implements a number of spatial techniques to correct data generation errors for each of the mini-MCA's six channels. Raw mini-MCA data exhibited a range of sensor errors, which included noise, per-pixel alternating gains, vignetting and lens distortion. An image-based dark offset subtraction reduced the effects of noise and alternating gain. Flat-field data was used to generate per-pixel look-up-tables that compensated for the radial shadowing of vignetting. Lens distortion was corrected using the Brown-Conrady model. The coefficients for the Brown-Conrady model were derived using multi-angle mini-MCA data of a planar calibration grid. The value of the correction framework was demonstrated through both data quality improvement and its capacity to explore and identify sensor errors. The framework provides automated, rapid sensor correction that is specific to the mini-MCA sensor used in this study. The framework proposed in this study has the potential for UAS developers to explore, assess and correct errors within other sensor systems.

6.2 Spatial Generalisation and Classification of UAS Ultra-Fine Spatial Resolution Data

6.2.1 Assess the performance of the UAS ultra-fine spatial resolution sample scale for image classification. Assess existing image texture modelling and GEOBIA segmentation methodologies for spatial generalisation. Develop image texture modelling and GEOBIA segmentation frameworks to spatially generalise ultra-fine UAS resolution to an optimal class-specific scale of analysis for image classification.

The capacity for image texture modelling and GEOBIA for the analysis of UAS data was explored. The ultra-fine spatial resolution of UAS data vastly increases local spatial complexity. The role of image texture modelling and GEOBIA in spatially generalising this complexity was explored. Ultra-fine spatial resolution multispectral UAS data of a saltmarsh community was acquired. The correction framework from Chapter 2 was utilised to improve data quality of the multispectral data. Image classification accuracy statistics were used to determine the performance of image texture modelling and GEOBIA. Analysis frameworks were constructed for each technique. Central to these frameworks was the goal to identify and incorporate class-specific scales of analysis.

An image texture model framework was developed in Chapter 3. The framework identifies optimal class-specific metrics generated from multiple texture models. An image mosaic with representative tiles for each class was generated from the multispectral data. Texture metrics were calculated for the mosaic using four different texture models: first order, grey-level co-occurrence matrix, local binary patterns operator, and wavelet. A random forest model was constructed based on the mosaic texture measures. The relative importance of texture measures within the model were calculated on a class-by-class basis. The selected texture measures were incorporated into an image classification and were found to improve the overall (a 17.23% increase) and class-specific classification accuracy.

The statistical properties of the random forest ensemble are highly suited to texture model analysis. The random forest ensemble is non-parametric, can process a range of statistical data types and is robust to the 'curse of dimensionality. Chapter 3 illustrates the capacity for a random forest framework to identify texture metrics from a large comparison of texture models and data types. A random forest framework is capable of identifying both optimal texture models and their respective scales of analysis.

A geospatial object-based image analysis (GEOBIA) framework was developed in Chapter 4. The framework identifies class-specific image segmentation parameters. User-digitised subsets are used to detect parameters that result in over- and under-segmentation. The class-specific validity of an image segmentation was assessed using both spatial and classification criteria. Spatial metrics are used to compare an image segmentation against user-digitised reference objects. This comparison provides a spatial accuracy assessment and detection of under-segmentation. Segmented objects of the subsets were classified using a random forest model. Classification accuracy was used to validate the spatial generalisation of segmented objects and to identify over-segmentation.

The GEOBIA framework developed in this study recognises the dual-role of image objects to provide spatial delineation and generalisation. Chapter 4 demonstrates that balancing spatial and classification accuracy improves GEOBIA segmentation. Smaller image objects generated higher spatial accuracy. This improvement was undermined, however, as smaller objects produced insufficient spatial generalisation thereby reducing classification accuracy. Through this phenomenon, a role for texture measures within GEOBIA was identified. Generated texture layers provide an independent source of spatial generalisation. This was found to improve both classification and spatial accuracy by reducing the need for segmentation to balance spatial delineation and generalisation.

6.3 UAS Saltmarsh AGB Modelling

6.3.1 Explore the UAS capacity to generate AGB estimations of fine-scale vegetation. Develop methodology to extract structural and AGB allometric parameters from fine-scale UAS data. Assess the direct substitution of field-based shrub allometric parameter measurements with UAS-derived measurements.

Techniques for field-based shrub AGB modelling were improved by introducing allometric parameters of individual stems, but are offset by the increase in time and labour. Chapter 5 assessed the measurements of field-based shrub-stem AGB modelling against UAS-based measurements. Spatial generalisation techniques established in Chapters 3 & 4 were used to define the spatial distribution of the saltmarsh shrub *Tecticornia arbuscula*. Destructive field sampling was used to allometrically model both stem structure and AGB. Allometric structural modelling was utilised to validate the segmentation of *Tecticornia sp.* into individual candidate stems. The geometry and height of an object, derived from Structure-from-Motion (SfM) 3D point clouds, was compared with an allometric model of stem structure. Object suitability for stem candidacy was assessed using a residual threshold from the model. AGB of the segmented candidate stems was estimated using the allometric model. *Tecticornia sp.* AGB at the study site was estimated between 3,440 and 4,482 kg. The results illustrates the underestimation of AGB when non-canopy species are excluded from AGB analysis. Chapter 5 demonstrates the potential application of ultra-fine spatial resolution UAS measurements for the direct application of plant allometric parameters.

6.4 Contributions to Knowledge

6.4.1 UAS Development

- The first data quality assessment of the mini-MCA 6-band multispectral sensor for UAS remote sensing.
- Development of a robust sensor correction framework for sensor-based data error, and the application of methodologies to restore data quality.

6.4.2 Image Analysis

- Development of an image texture framework with the capacity to analyse a large range of texture models and metrics, identify class-specific texture metrics at meaningful scales of analysis, and improve the classification accuracy of UAS ultra-fine spatial resolution data.
- Development of a GEOBIA framework to identify image segmentation parameters relevant to class-specific scales of analysis, and further improve the classification accuracy of UAS ultra-fine spatial resolution data.
- Integration of image texture and GEOBIA into a single framework and demonstration of the capacity for image texture metrics to shift the burden of spatial generalisation away from image segmentation, thereby further improving the classification accuracy of UAS ultra-fine spatial resolution data.

6.4.3 Saltmarsh Mapping

- Proof-of-concept for fine-scale mapping and monitoring of small-scale vegetation communities using UAS.
- Integration of a species-level scale of analysis for the classification of saltmarsh communities.

- Development of a methodology to adapt field-level allometric structural modelling for the segmentation of saltmarsh shrub structure utilising GEOBIA and SfM.
- Integration of the ultra-fine spatial measurements of UAS for the extraction of allometric model parameters, allowing the estimation of AGB of a small-scale saltmarsh shrub species.

6.5 Limitations and Future Research Directions

Key to unlocking the potential of a new remote sensing platform is an understanding of its data generation characteristics. Remote sensing platforms can be distinguished by their spectral, radiometric, spatial and temporal resolutions. The balance between these four characteristics determines the suitability of a platform for an observational task. The UAS occupies a previously unfilled niche, and is capable of generating data with very high spatial and temporal resolutions. The current limitations of UAS predominately arise from their small size, which limits payload weight and flight duration.

UAS weight and power limitations affect the selection of sensor systems. The sensor is directly responsible for spectral and radiometric data qualities. UAS limitations require considerable miniaturisation of sensor systems in order to fit weight and power constraints. Given the high cost of high quality sensor miniaturisation, recent development of low-cost commercial-off-the-shelf (COTS) systems has required the use of lower quality components. This negatively impacts upon data quality. The performance of sensor correction frameworks, while providing valuable improvements in data quality, are eventually limited by design decisions in sensor construction.

A design decision that significantly undermines the quality of mini-MCA data was the use of a progressive shutter (also known as a rolling shutter). Chapter 2 illustrates the significant contribution of the progressive shutter to sensor noise. To a greater degree however, is its impact upon dataset construction. The lightweight multirotor UAS used

within this study is vulnerable to buffeting by wind gusts. On occasion, the progressive processing of an image scene during a buffeting incident results in vertical deformation within discrete areas of data. This distorts the spatial relationship between image features, significantly undermining attempts to generate SfM pointclouds. Due to this effect, the construction of the mini-MCA dataset presented in Chapter 3 & 4 proved a significant challenge and a planned mini-MCA dataset for Chapter 5 had to be abandoned.

The current lack of commercial, low-cost, quality UAS sensors has led research groups to develop their own in-house. In-house sensor development, when coupled with a familiarity of UAS remote sensing constraints, improves sensor design decisions. However, one of the fundamental appeals of UAS remote sensing is its low-cost accessibility. Sensor development is potentially a significant expense that would undermine this accessibility. Despite this, UAS remote sensing is still relatively young. It can be expected that UAS accessibility will improve as consumer response and competitive pressures improve design decisions that increase data quality while reducing manufacturing costs.

A novel aspect of the UAS is its capacity to generate ultra-fine resolution spatial data. The increase in spatial complexity introduces both new analysis challenges and opportunities. Clear solutions for image classification using spatial generalisation are addressed in Chapters 3 & 4. Chapter 5 utilises SfM and image segmentation to derive and incorporate biophysical structure into an analysis of AGB. SfM point clouds have only recently been adopted for remote sensing, and extracting vegetation structure remains a challenge. Their high density and lack of multi-return undermine traditional LiDAR point cloud filtering. The successful vegetation filtering within Chapter 5 was aided by the lack of vertical stratification in saltmarsh communities. Incorporating SfM point clouds for remote sensing of vegetation may require alternative approaches towards UAS data collection. This may include integrating multi-sensor systems or adopting non-nadir flight patterns to capture 3D structure obliquely.

An unexplored aspect within this study is the effect of UAS sampling scale on spectral

indices. Spectral indices are calculated on a per-pixel basis from spectral measurements between different bands. Targeted spectral bands have a known response to a specific material or specific conditions. The relationship between spectral bands can be used to correlate proportional contribution from the generalised spectral response of a single pixel.

The sample scale of UAS data lacks per-pixel generalisation. Pixel specificity increases spatial variability and drives the need for broader spatial generalisation. This raises the question of the effect of pixel specificity on spectral indices, particularly those that provide a sub-pixel measure. This ties in to broader questions about the effect of analysis scale upon spectral indices. In addition to spatial resolution there is also the effect of radiometric resolution of UAS sensors. Chapter 2 illustrates the variability in monochromatic efficiency that is required by low-cost sensors to ensure broad spectral sensitivity. This raises the additional question of the effect of unequal spectral quantisation upon the calculation of indices generated using low-cost instruments.

The ultra-fine spatial resolution of UAS data was a focus of this thesis. High temporal resolutions, which are also a strong characteristic of UAS data collection, were not explored. On-going vegetation monitoring requires the quantification of spatial changes in environmental conditions. The UAS, with low operational costs and rapid deployment, can be flown on demand. This allows the generation of data within very narrow temporal windows. The UAS is therefore ideal for monitoring of fine scale-spatial and temporal changes within the environment. Together, Chapters 3, 4 & 5 outlay a general framework of analysis techniques for ultra-fine spatial resolution data for the characterisation and monitoring of vegetation communities. The next task is to transfer these techniques into a temporal framework for the detection and analysis of change.

When compared against other remote sensing platforms, UAS are typically smaller, and fly within reduced altitude and operational ranges. This fits the UAS within a spatial niche of ultra-fine resolution but low spatial extents. This spatial niche presents two broad applications for UAS vegetation monitoring.

The first application is for geographic areas within the spatial extent limitations of UAS. Small scale vegetation communities may be benefited by precision UAS measurements for mapping distribution, structure of temporal changes. This first application is demonstrated within this thesis through the utilisation of UAS for mapping and measuring fine-scale saltmarsh communities. Saltmarsh vegetation is well suited to UAS remote sensing as it lacks complex vertical stratification, while environmental zonation reduces the spatial heterogeneity of species distribution. A structurally simplified environment enabled more focus upon the development of image analysis techniques. The next step is to explore the transfer of the techniques established within this thesis into more spatially and structurally complex natural environments.

The second broad application of UAS is integration within a multiscale analysis. Aerial or satellite platforms are suited to data collection across large spatial extents. Analysis of this sample scale provides broad landscape metrics. The niche role of the UAS enters within fine-scale plot-level assessments. Chapter 5 illustrates the potential for UAS measurements in the application of fine-scale allometric modelling. Multiscale frameworks are needed to integrate spatial data from several scales of analysis. Through such integration, the fine-scale plot modelling of UAS could be linked with landscape metrics to extrapolate information accurately and consistently across broad geographic areas.

6.6 Final Remarks

Fine-scale samples are essential for monitoring small, fragmented saltmarsh communities. Only through UAS platforms can remote sensing match the sample scale required for precision saltmarsh monitoring. This thesis provides foundation techniques for the generation and analysis of ultra-fine spatial resolution UAS data for detailed mapping and monitoring of complex natural vegetation communities. These novel techniques are successfully demonstrated within the context of fine-scale mapping of saltmarsh commu-

nities. The image analysis frameworks in this thesis have broad application and provide a firm foundation to advance the UAS from a novel research tool into a practical vegetation monitoring instrument.

REFERENCES

Adam, P. (2002). Saltmarshes in a time of change. *Environmental conservation*, 29(01):39–61.

Agüera, F., Aguilar, F. J., and Aguilar, M. (2008). Using texture analysis to improve per-pixel classification of very high resolution images for mapping plastic greenhouses. *ISPRS Journal of Photogrammetry and Remote Sensing*, 63(6):635–646.

Aguilar, M., Saldaña, M., and Aguilar, F. (2013). GeoEye-1 and WorldView-2 pan-sharpened imagery for object-based classification in urban environments. *International Journal of Remote Sensing*, 34(7):2583–2606.

Ahmed, R., Siqueira, P., Hensley, S., and Bergen, K. (2013). Uncertainty of Forest Biomass Estimates in North Temperate Forests Due to Allometry: Implications for Remote Sensing. *Remote Sensing*, 5(6):3007–3036.

Al-amri, S. (2010). A Comparative Study of Removal Noise from Remote Sensing Image. *International Journal of Computer Science Issues*, 7(1):32–36.

Albrecht, F., Lang, S., and Hölbling, D. (2010). Spatial accuracy assessment of object boundaries for object-based image analysis. *The International Archives of the Photogrammetry, Remote Sensing and Spatial Information Sciences*, 38(4):C7.

Anaya, J. A., Chuvieco, E., and Palacios-Orueta, A. (2009). Aboveground biomass assessment in Colombia: A remote sensing approach. *Forest Ecology and Management*, 257(4):1237–1246.

Asner, G. (1998). Biophysical and biochemical sources of variability in canopy reflectance. *Remote sensing of environment*, 253(3):234–253.

Baskerville, G. (1972). Use of logarithmic regression in the estimation of plant biomass. *Canadian Journal of Forest Research*, 2(1):49–53.

Benz, U. C., Hofmann, P., Willhauck, G., Lingenfelder, I., and Heynen, M. (2004). Multi-resolution, object-oriented fuzzy analysis of remote sensing data for GIS-ready information. *ISPRS Journal of Photogrammetry and Remote Sensing*, 58(3-4):239–258.

Berni, J. and Zarco-Tejada, P. (2009). Thermal and narrowband multispectral remote sensing for vegetation monitoring from an unmanned aerial vehicle. *IEEE Transactions on Geoscience and Remote Sensing*, 47(3):722–738.

Bertness, M. (1991). Zonation of Spartina patens and Spartina alterniflora in New England salt marsh. *Ecology*, 72(1):138–148.

Bertness, M. and Shumway, S. (1993). Competition and facilitation in marsh plants. *American Naturalist*, 142(4):718–724.

Blaschke, T. (2010). Object based image analysis for remote sensing. *ISPRS Journal of Photogrammetry and Remote Sensing*, 65(1):2–16.

Blaschke, T., Hay, G., Kelly, M., and Lang, S. (2014). Geographic Object-Based Image AnalysisTowards a new paradigm. *ISPRS Journal of . . .*, 87:180–191.

Breiman, L. (2001). Random forests. *Machine learning*, 45(1):5–32.

Carvalho, L. M. T., Fonseca, L. M. G., Murtagh, F., and Clevers, J. G. P. W. (2001). Digital change detection with the aid of multiresolution wavelet analysis. *International Journal of Remote Sensing*, 22(18):3871–3876.

Castilla, G. and Hay, G. (2007). An Automated Delineation Tool For Assisted Interpretation of Digital Imagery. *ASPRS 2007 Annual Conference*.

Chan, J. C.-W. and Paelinckx, D. (2008). Evaluation of Random Forest and Adaboost tree-based ensemble classification and spectral band selection for ecotope mapping using airborne hyperspectral imagery. *Remote Sensing of Environment*, 112(6):2999–3011.

Chang-yanab, C. (2008). Study on methods of noise reduction in a stripped image. *The International Archives of the Photogrammetry, Remote Sensing and Spatial Information Sciences*, pages 213–216.

Chao, H., Baumann, M., Jensen, A., Chen, Y., Cao, Y., Ren, W., and McKee, M. (2008). Band-reconfigurable multi-UAV-based cooperative remote sensing for real-time water management and distributed irrigation control. *Proc. of the IFAC World Congress, Seoul, Korea*.

Chen, J., Chen, D., and Blostein, D. (2007). Wavelet-Based Classification of Remotely Sensed Images: A Comparative Study of Different Feature Sets in an Urban Environment. *Journal of Environmental Informatics*, 10(1):2–9.

Cheng, Q., Varshney, P., and Arora, M. (2006). Logistic Regression for Feature Selection and Soft Classification of Remote Sensing Data. *IEEE Geoscience and Remote Sensing Letters*, 3(4):491–494.

Chisholm, R. and Cui, J. (2013). UAV LiDAR for below-canopy forest surveys. *Journal of Unmanned Vehicle Systems*, 1(1):61–68.

Clark, M. L., Roberts, D. A., Ewel, J. J., and Clark, D. B. (2011). Estimation of tropical rain forest aboveground biomass with small-footprint lidar and hyperspectral sensors. *Remote Sensing of Environment*, 115(11):2931–2942.

Clodius, W. B., Weber, P. G., Borel, C. C., and Smith, B. W. (1998). Multi-spectral band selection for satellite-based systems. *Aerospace/Defense Sensing and Controls*, pages 11–21.

Congalton, R. (1991). A review of assessing the accuracy of classifications of remotely sensed data. *Remote sensing of environment*, 46(1):35–46.

Cooley, T., Anderson, G., Felde, G., Hoke, M., Ratkowski, A., Chetwynd, J., Gardner, J., Adler-Golden, S., Matthew, M., and Berk, A. (2002). FLAASH, a MODTRAN4-based atmospheric correction algorithm, its application and validation. *Geoscience and Remote Sensing Symposium, 2002. IGARSS'02. 2002 IEEE International*, 3:1414–1418.

Cracknell, A. P. (1998). Synergy in remote sensing - whats in a pixel? *International Journal of Remote Sensing*, 19(11):2025–2047.

Darwish, A., Leukert, K., and Reinhardt, W. (2003). Image segmentation for the purpose of object-based classification. *International Geoscience and ...*, 3:2039–2041.

de Villiers, J., Leuschner, F. W., and Geldenhuys, R. (2010). Modeling of radial asymmetry in lens distortion facilitated by modern optimization techniques. *IS&T/SPIE Electronic Imaging*.

Dorigo, W., Lucieer, A., Podobnikar, T., and Čarni, A. (2012). Mapping invasive Fallopia japonica by combined spectral, spatial, and temporal analysis of digital orthophotos. *International Journal of Applied Earth Observation and Geoinformation*, 19:185–195.

Drake, J. and Knox, R. (2003). Above-ground biomass estimation in closed canopy neotropical forests using lidar remote sensing: Factors affecting the generality of relationships. *Global Ecology and Biogeography*, 12(2):147–159.

Dubayah, R. O., Sheldon, S. L., Clark, D. B., Hofton, M. A., Blair, J. B., Hurtt, G. C., and Chazdon, R. L. (2010). Estimation of tropical forest height and biomass dynamics using lidar remote sensing at La Selva, Costa Rica. *Journal of Geophysical Research: Biogeosciences*, 115(G2).

Dunford, R., Michel, K., Gagnage, M., Piégay, H., and Trémelo, M.-L. (2009). Potential and constraints of Unmanned Aerial Vehicle technology for the characterization of Mediterranean riparian forest. *International Journal of Remote Sensing*, 30(19):4915–4935.

Dungan, J. L., Perry, J. N., Dale, M. R. T., Legendre, P., Fortin, M., Jakomulska, A., Miriti, M., Rosenberg, M. S., and Fortin, S. (2002). A balanced view of scale in spatial statistical analysis. *Ecography*, 25(February):626–640.

Duro, D. C., Franklin, S. E., and Dubé, M. G. (2012). Multi-scale object-based image analysis and feature selection of multi-sensor earth observation imagery using random forests. *International Journal of Remote Sensing*, 33(14):4502–4526.

Eckert, S. (2012). Improved Forest Biomass and Carbon Estimations Using Texture Measures from WorldView-2 Satellite Data. *Remote Sensing*, 4(12):810–829.

Ella, L. and van den Bergh, F. (2008). A comparison of texture feature algorithms for urban settlement classification. *Geoscience and Remote Sensing Symposium, 2008. IGARSS 2008. IEEE International*, 3:III–1308.

Emery, N., Ewanchuk, P., and Bertness, M. (2001). Competition and salt-marsh plant zonation: stress tolerators may be dominant competitors. *Ecology*, 82(9):2471–2485.

Feizizadeh, B. and Blaschke, T. (2013). A semi-automated object based image analysis approach for landslide delineation. *The 2013 European space agency living planet symposium*, 2013(September):9–13.

Feldpausch, T. R., Lloyd, J., Lewis, S. L., Brienen, R. J. W., Gloor, M., Monteagudo Mendoza, A., Lopez-Gonzalez, G., Banin, L., Abu Salim, K., Affum-Baffoe, K., Alexiades, M., Almeida, S., Amaral, I., Andrade, A., Aragão, L. E. O. C., Araujo Murakami, A., Arets, E. J. M. M., Arroyo, L., Aymard C., G. A., Baker, T. R., Bánki, O. S., Berry, N. J., Cardozo, N., Chave, J., Comiskey, J. A., Alvarez, E., de Oliveira, A., Di Fiore, A., Djagbletey, G., Domingues, T. F., Erwin, T. L., Fearnside, P. M., França, M. B., Freitas, M. A., Higuchi, N., Iida, Y., Jiménez, E., Kassim, A. R., Killeen, T. J., Laurance, W. F., Lovett, J. C., Malhi, Y., Marimon, B. S., Marimon-Junior, B. H., Lenza, E., Marshall, A. R., Mendoza, C., Metcalfe, D. J., Mitchard, E. T. A., Neill, D. A., Nelson, B. W., Nilus, R., Nogueira, E. M., Parada, A., Peh, K. S.-H., Pena Cruz, A., Peñuela, M. C., Pitman, N. C. A., Prieto, A., Quesada, C. A., Ramírez, F., Ramírez-Angulo, H., Reitsma, J. M., Rudas, A., Saiz, G., Salomão, R. P., Schwarz, M., Silva, N., Silva-Espejo, J. E., Silveira, M., Sonké, B., Stropp, J., Taedoumg, H. E., Tan, S., ter Steege, H., Terborgh, J., Torello-Raventos, M., van der Heijden, G. M. F., Vásquez, R., Vilanova, E., Vos, V. A., White, L., Willcock, S., Woell, H., and Phillips, O. L. (2012). Tree height integrated into pantropical forest biomass estimates. *Biogeosciences*, 9(8):3381–3403.

Fonstad, M. A., Dietrich, J. T., Courville, B. C., Jensen, J. L., and Carbonneau, P. E. (2013). Topographic structure from motion: a new development in photogrammetric measurement. *Earth Surface Processes and Landforms*, 38(4):421–430.

Friedl, M. and Brodley, C. (1997). Decision tree classification of land cover from remotely sensed data. *Remote sensing of environment*, 61(3):399–409.

Frolking, S., Palace, M. W., Clark, D. B., Chambers, J. Q., Shugart, H. H., and Hurtt, G. C. (2009). Forest disturbance and recovery: A general review in the context of spaceborne remote sensing of impacts on aboveground biomass and canopy structure. *Journal of Geophysical Research: Biogeosciences*, 114(G2).

Genuer, R., Poggi, J.-M., and Tuleau-Malot, C. (2010). Variable selection using random forests. *Pattern Recognition Letters*, 31(14):2225–2236.

Glenn, E., Huete, A., Nagler, P., and Nelson, S. (2008). Relationship between remotely-sensed vegetation indices, canopy attributes and plant physiological processes: what vegetation indices can and cannot tell us. *Sensors*, 8(4):2136–2160.

Goetz, S. (2006). Remote Sensing of Riparian Buffers: Past Progress and Future Prospects. *JAWRA Journal of the American Water Resources ...*, 42(1):133–143.

Goldman, D. B. (2010). Vignette and exposure calibration and compensation. *IEEE transactions on pattern analysis and machine intelligence*, 32(12):2276–88.

Granitto, P., Gasperi, F., Biasioli, F., Trainotti, E., and Furlanello, C. (2007). Modern data mining tools in descriptive sensory analysis: A case study with a Random forest approach. *Food Quality and Preference*, 18(4):681–689.

Guo, Z., Zhang, L., and Zhang, D. (2010). Rotation invariant texture classification using LBP variance (LBPV) with global matching. *Pattern Recognition*, 43(3):706–719.

Guyon, I. and Elisseeff, A. (2003). An introduction to variable and feature selection. *The Journal of Machine Learning Research*, 3:1157–1182.

Haralick, R. (1973). Textural features for image classification. *Systems, Man and Cybernetics, IEEE Transactions*, 6:610–621.

Hay, G., Niemann, K., and McLean, G. (1996). An object-specific image-texture analysis of H-resolution forest imagery. *Remote Sensing of Environment*, 55(2):108–122.

Herold, M., Liu, X., and Clarke, K. (2003). Spatial metrics and image texture for mapping urban land use. *Photogrammetric Engineering and Remote Sensing*, 69(9):991–1001.

Hinkley, E. A. and Zajkowski, T. (2011). USDA forest serviceNASA: unmanned aerial systems demonstrations pushing the leading edge in fire mapping. *Geocarto International*, 26(2):103–111.

Hugemann, W. (2010). Correcting lens distortions in digital photographs. *Ingenieurbüro Morawski+ Hugemann: Leverkusen, Germany*, pages 1–12.

Hunt, Jr., E. R., Hively, W. D., Fujikawa, S. J., Linden, D. S., Daughtry, C. S. T., and McCarty, G. W. (2010). Acquisition of NIR-Green-Blue Digital Photographs from Unmanned Aircraft for Crop Monitoring. *Remote Sensing*, 2(1):290–305.

Jedlička, J. and Potčková, M. (2007). Correction of radial distortion in digital images. *Proceedings Technical Computing Prague*.

Jenkins, J. C., Chojnacky, D. C., Heath, L. S., and Birdsey, R. A. (2003). National-Scale Biomass Estimators for United States Tree Species. *Forest Science*, 49(1):12–35.

Johnson, B. and Xie, Z. (2013). Classifying a high resolution image of an urban area using super-object information. *ISPRS Journal of Photogrammetry and Remote Sensing*, 83:40–49.

Johnson, P., Johnson, C., and West, N. (1988). Estimation of phytomass for ungrazed crested wheatgrass plants using allometric equations. *Journal of Range Management*, 41(5):421–425.

Jones, D., Pike, S., Thomas, M., and Murphy, D. (2011). Object-Based Image Analysis for Detection of Japanese Knotweed s.l. taxa (Polygonaceae) in Wales (UK). *Remote Sensing*, 3(12):319–342.

Kattenborn, G. (2014). Potential of Unmanned Aerial Vehicle Based Photogrammetric Point Clouds for Automatic Single Tree Detection. *Deutsche Gesellschaft für Photogrammetrie*, pages 1–6.

Kelcey, J. and Lucieer, A. (2012). Sensor Correction of a 6-Band Multispectral Imaging Sensor for UAV Remote Sensing. *Remote Sensing*, 4(12):1462–1493.

Ketterings, Q. M., Coe, R., van Noordwijk, M., Ambagau, Y., and Palm, C. A. (2001). Reducing uncertainty in the use of allometric biomass equations for predicting above-ground tree biomass in mixed secondary forests. *Forest Ecology and Management*, 146(1-3):199–209.

Kim, M., Madden, M., and Warner, T. (2009). Forest type mapping using object-specific texture measures from multispectral IKONOS imagery: Segmentation quality and image classification issues. *Photogrammetric Engineering and Remote Sensing*, 75(7):819–829.

Kim, S. J. and Pollefeys, M. (2008). Robust radiometric calibration and vignetting correction. *IEEE transactions on pattern analysis and machine intelligence*, 30(4):562–76.

Kitchen, C. (2011). Nonparametric variable selection using machine learning algorithms in high dimensional (large P, small N) biomedical applications. *Biomedical Engineering: Trends in Electronics, Communications and Software, Rijeka, Croatia: InTech*, pages 589–600.

Klemas, V. (2001). Remote sensing of landscape-level coastal environmental indicators. *Environmental Management*, 27(1):47–57.

Lacava, T., Brocca, L., Calice, G., Melone, F., Moramarco, T., Pergola, N., and Tramutoli, V. (2010). Soil moisture variations monitoring by AMSU-based soil wetness indices: A long-term inter-comparison with ground measurements. *Remote Sensing of Environment*, 114(10):2317–2325.

Laegdsgaard, P. (2006). Ecology, disturbance and restoration of coastal saltmarsh in Australia: a review. *Wetlands Ecology and Management*, 14(5):379–399.

Laliberte, A., Browning, D., and Rango, A. (2012). A comparison of three feature selection methods for object-based classification of sub-decimeter resolution UltraCam-L imagery. *International Journal of Applied Earth Observation and Geoinformation*, 15:70–78.

Laliberte, A., Rango, A., and Herrick, J. (2007). Unmanned aerial vehicles for rangeland mapping and monitoring: a comparison of two systems. *ASPRS Annual Conference Proceedings*.

Laliberte, A. S., Goforth, M. A., Steele, C. M., and Rango, A. (2011a). Multispectral Remote Sensing from Unmanned Aircraft: Image Processing Workflows and Applications for Rangeland Environments. *Remote Sensing*, 3(12):2529–2551.

Laliberte, A. S., Herrick, J. E., Rango, A., and Winters, C. (2010). Acquisition, orthorectification, and object-based classification of unmanned aerial vehicle (UAV) imagery for rangeland monitoring. *Photogrammetric Engineering and Remote Sensing*, 76(6):661–672.

Laliberte, A. S., Winters, C., and Rango, A. (2011b). UAS remote sensing missions for rangeland applications. *Geocarto International*, 26(2):141–156.

Lechner, A. (2012). Characterising Upland Swamps Using Object-based Classification Methods and Hyper-spatial Resolution Imagery Derived from an Unmanned Aerial Vehicle. *ISPRS Annals of the Photogrammetry, Remote Sensing and Spatial Information Sciences I-4*, I:101–106.

Lelong, C. C. D. (2008). Assessment of Unmanned Aerial Vehicles Imagery for Quantitative Monitoring of Wheat Crop in Small Plots. *Sensors*, 8(5):3557–3585.

Levine, J. M., Brewer, J. S., and Bertness, M. D. (1998). Nutrients, competition and plant zonation in a New England salt marsh. *Journal of Ecology*, 86(2):285–292.

Lin, Y., Hyyppa, J., and Jaakkola, A. (2011). Mini-UAV-borne LIDAR for fine-scale mapping. *Geoscience and Remote Sensing Letters, IEEE*, 8(3):426–430.

Lingua, A., Marenchino, D., and Nex, F. (2009). Performance Analysis of the SIFT Operator for Automatic Feature Extraction and Matching in Photogrammetric Applications. *Sensors*, 9(5):3745–66.

Liu, D. and Xia, F. (2010). Assessing object-based classification: advantages and limitations. *Remote Sensing Letters*, 1(4):187–194.

Loh, W. (2012). Variable selection for classification and regression in large p, small n problems. *Probability Approximations and Beyond*, 205:133–157.

Lu, D. (2006). The potential and challenge of remote sensing-based biomass estimation. *International Journal of Remote Sensing*, 27(7):1297–1328.

Lucieer, A., Robinson, S., and Turner, D. (2011). Unmanned aerial vehicle (UAV) remote sensing for hyperspatial terrain mapping of Antarctic moss beds based on structure from motion (SfM) point clouds. *Proceedings of the 34th International Symposium on Remote Sensing of Environment (ISRSE34)*, 10.

Lucieer, A., Turner, D., King, D. H., and Robinson, S. A. (2014). Using an Unmanned Aerial Vehicle (UAV) to capture micro-topography of Antarctic moss beds Using an Unmanned Aerial Vehicle (UAV) to capture micro-topography. *International Journal of Applied Earth Observation and Geoinformation*, 27:53–62.

Ludwig, J., Reynolds, J., and Whitson, P. (1975). Size-biomass relationships of several Chihuahuan desert shrubs. *American Midland Naturalist*, 94(2):451–461.

Lutz, D. a., Washington-Allen, R. A., and Shugart, H. H. (2008). Remote sensing of boreal forest biophysical and inventory parameters: a review. *Canadian Journal of Remote Sensing*, 34(S2):S286–S313.

Mahiny, A. S. and Turner, B. J. (2007). A Comparison of Four Common Atmospheric Correction Methods. *Photogrammetric Engineering & Remote Sensing*, 73(4):361–368.

Maillard, P. (2003). Comparing texture analysis methods through classification. *Photogrammetric engineering and remote sensing*, 69(April):357–367.

Mansouri, A., Marzani, F., and Gouton, P. (2005). Development of a Protocol for CCD Calibration: Application to a Multispectral Imaging System. *International Journal of Robotics and Automation*, 20(2):94–100.

Marceau, D. (1999). The scale issue in social and natural sciences. *Canadian Journal of Remote Sensing*, 25(4):347–356.

Marceau, D. and Hay, G. (1999). Remote sensing contributions to the scale issue. *Canadian journal of remote sensing*, 25(4):357–366.

Marmol, U. (2011). Use of Gabor filters for texture classification of airborne images and LIDAR data. *Archives of Photogrammetry, Cartography and Remote Sensing*, 22:325–336.

Möller, M., Lymburner, L., and Volk, M. (2007). The comparison index: A tool for assessing the accuracy of image segmentation. *International Journal of Applied Earth Observation and Geoinformation*, 9(3):311–321.

Mullikin, J., van Vliet, L., and Netten, H. (1994). Methods for CCD camera characterization. *Proc. SPIE*, 2173:73–84.

Murray, R. B. and Jacobson, M. Q. (1982). An Evaluation of Dimension Analysis for Predicting Shrub Biomass. *Journal of Range Management Archives*, 35(4):451–454.

Myint, S. W., Gober, P., Brazel, A., Grossman-Clarke, S., and Weng, Q. (2011). Per-pixel vs. object-based classification of urban land cover extraction using high spatial resolution imagery. *Remote Sensing of Environment*, 115(5):1145–1161.

Nickless, A., Scholes, R. J., and Archibald, S. (2011). A method for calculating the variance and confidence intervals for tree biomass estimates obtained from allometric equations. *South African Journal of Science*, 107(5/6):1–10.

Ohmann, L., Grigal, D., and Rogers, L. (2006). Estimating plant biomass for undergrowth species of northeastern Minnesota forest communities. *General Technical Report NC-61. St. Paul, MN: US Dept. of Agriculture, Forest Service, North Central Forest Experiment Station*, (http://www.nrs.fs.fed.us/pubs/126).

Ojala, T. and Pietikäinen, M. (1999). Unsupervised texture segmentation using feature distributions. *Pattern Recognition*, 32:477–486.

Pal, M. and Mather, P. M. (2003). An assessment of the effectiveness of decision tree methods for land cover classification. *Remote Sensing of Environment*, 86(4):554–565.

Park, J., Byun, S.-C., and Lee, B.-U. (2009). Lens distortion correction using ideal image coordinates. *IEEE Transactions on Consumer Electronics*, 55(3):987–991.

Pastor, E., Barrado, C., Royo, P., Santamaria, E., Lopez, J., and Salami, E. (2011). Architecture for a helicopter-based unmanned aerial systems wildfire surveillance system. *Geocarto International*, 26(2):113–131.

Pastor, E., Lopez, J., and Royo, P. (2007). UAV payload and mission control hardware/software architecture. *Aerospace and Electronic Systems Magazine, IEEE*, 22(6):3–8.

Pennings, S. and Callaway, R. (1992). Salt marsh plant zonation: the relative importance of competition and physical factors. *Ecology*, 73(2):681–690.

Phinn, S., Stow, D., and Mouwerik, D. V. (1999). Remotely sensed estimates of vegetation structural characteristics in restored wetlands, Southern California. *Photogrammetric engineering and remote sensing*, 65(4):485–493.

Picard, N., Saint-André, L., and Henry, M. (2012). Manual for building tree volume and biomass allometric equations: from field measurement to prediction. *Forest Ecology and management*, 146(1):199–209.

Plaza, J., Plaza, A., Perez, R., and Martinez, P. (2009). On the use of small training sets for neural network-based characterization of mixed pixels in remotely sensed hyperspectral images. *Pattern Recognition*, 42(11):3032–3045.

Powers, R. P., Hay, G. J., and Chen, G. (2012). How wetland type and area differ through scale: A GEOBIA case study in Alberta's Boreal Plains. *Remote Sensing of Environment*, 117:135–145.

Prahalad, V. (2010). *Temporal changes in South-Eastern Tasmanian saltmarshes*. PhD thesis, University of Tasmania.

Prescott, B. and McLean, G. (1997). Line-Based Correction of Radial Lens Distortion. *Graphical Models and Image Processing*, 59(1):39–47.

Priedtis, G., Šmits, I., Arhipova, I., Dais, S., and Dubrovskis, D. (2012). Tree Diameter Models from Field and Remote sensing data. *International Journal of Mathematical Models and Methods in Applied Sciences*, 6(6):707–714.

Primicerio, J., Di Gennaro, S. F., Fiorillo, E., Genesio, L., Lugato, E., Matese, A., and Vaccari, F. P. (2012). A flexible unmanned aerial vehicle for precision agriculture. *Precision Agriculture*, 13(4):517–523.

Puissant, A., Hirsch, J., and Weber, C. (2005). The utility of texture analysis to improve per-pixel classification for high to very high spatial resolution imagery. *International Journal of Remote Sensing*, 26(4):733–745.

Radoux, J., Defourny, P., and Bogaert, P. (2008). Comparison of pixel-and object-based sampling strategies for thematic accuracy assessment. *GEOBIA 2008-Pixels, Objects, Intelligence*, pages 5–8.

Robinson, C., Saatchi, S., Neumann, M., and Gillespie, T. (2013). Impacts of Spatial Variability on Aboveground Biomass Estimation from L-Band Radar in a Temperate Forest. *Remote Sensing*, 5(3):1001–1023.

Rodriguez-Galiano, V., Ghimire, B., Rogan, J., Chica-Olmo, M., and Rigol-Sanchez, J. (2012). An assessment of the effectiveness of a random forest classifier for land-cover classification. *ISPRS Journal of Photogrammetry and Remote Sensing*, 67:93–104.

Rosenschein, A., Tietema, T., and Hall, D. (1999). Biomass measurement and monitoring of trees and shrubs in a semi-arid region of central Kenya. *Journal of Arid Environments*, 42(2):97–116.

Roy, P. S. and Ravan, S. A. (1996). Biomass estimation using satellite remote sensing data - An investigation on possible approaches for natural forest. *Journal of Biosciences*, 21(4):535–561.

Rudol, P. and Doherty, P. (2008). Human body detection and geolocalization for UAV search and rescue missions using color and thermal imagery. *Aerospace Conference, 2008 IEEE*, pages 1–8.

Safavian, S. and Landgrebe, D. (1991). A survey of decision tree classifier methodology. *IEEE transactions on systems, man, and cybernetics*, 21(3):660–674.

Schimel, D. (1995). Terrestrial ecosystems and the carbon cycle. *Global change biology*, 1(1):77–91.

Shi, T. and Horvath, S. (2006). Unsupervised learning with random forest predictors. *Journal of Computational and Graphical Statistics*, 15(1):118–138.

Shinde, M. and Shrivastava, M. (2012). Using Local Binary Pattern Variance for Land Classification and Crop Identification. *International Journal of Advanced ...*, 2(2).

Shrestha, R. and Wynne, R. H. (2012). Estimating Biophysical Parameters of Individual Trees in an Urban Environment Using Small Footprint Discrete-Return Imaging Lidar. *Remote Sensing*, 4(12):484–508.

Silvestri, S., Marani, M., and Marani, A. (2003). Hyperspectral remote sensing of salt marsh vegetation, morphology and soil topography. *Physics and Chemistry of the Earth*, 28(1-3):15–25.

Sims, D. and Gamon, J. (2002). Relationships between leaf pigment content and spectral reflectance across a wide range of species, leaf structures and developmental stages. *Remote Sensing of Environment*, 81(2-3):337–354.

Sithole, G. and Vosselman, G. (2003). Comparison of filtering algorithms. *Proceedings of the ISPRS working group III/3 workshop*, pages 71–78.

Sithole, G. and Vosselman, G. (2005). Filtering of airborne laser scanner data based on segmented point clouds. *International Archives of Photogrammetry, Remote Sensing and Spatial Information Sciences*, 36(3):66–71.

Smith, G. M. and Milton, E. J. (1999). The use of the empirical line method to calibrate remotely sensed data to reflectance. *International Journal of Remote Sensing*, 20(13):2653–2662.

Stefanik, K. V., Gassaway, J. C., Kochersberger, K., and Abbott, a. L. (2011). UAV-Based Stereo Vision for Rapid Aerial Terrain Mapping. *GIScience & Remote Sensing*, 48(1):24–49.

Stephenson, N. L., Das, A. J., Condit, R., Russo, S. E., Baker, P. J., Beckman, N. G., Coomes, D. a., Lines, E. R., Morris, W. K., Rüger, N., Alvarez, E., Blundo, C., Bunyavejchewin, S., Chuyong, G., Davies, S. J., Duque, A., Ewango, C. N., Flores, O., Franklin, J. F., Grau, H. R., Hao, Z., Harmon, M. E., Hubbell, S. P., Kenfack, D., Lin, Y., Makana, J.-R., Malizia, A., Malizia, L. R., Pabst, R. J., Pongpattananurak, N., Su, S.-H., Sun, I.-F., Tan, S., Thomas, D., van Mantgem, P. J., Wang, X., Wiser, S. K., and Zavala, M. A. (2014). Rate of tree carbon accumulation increases continuously with tree size. *Nature*, 507(7490):90–3.

Strahler, A. H., Woodcock, C. E., and Smith, J. A. (1986). On the nature of models in remote sensing. *Remote Sensing of Environment*, 20(2):121–139.

Strobl, C., Boulesteix, A., and Kneib, T. (2008). Conditional variable importance for random forests. *BMC bioinformatics*, 9(1):307–319.

Strobl, C., Boulesteix, A.-L., Zeileis, A., and Hothorn, T. (2007). Bias in random forest variable importance measures: illustrations, sources and a solution. *BMC bioinformatics*, 8(1):25.

Stuckens, J., Coppin, P., and Bauer, M. (2000). Integrating contextual information with per-pixel classification for improved land cover classification. *Remote Sensing of Environment*, 71(3):282–296.

Stumpf, A. and Kerle, N. (2011). Object-oriented mapping of landslides using Random Forests. *Remote Sensing of Environment*, 115(10):2564–2577.

Suchenwirth, L., Gärtner, P., Förster, M., and Kleinschmit, B. (2012). Combining Object-based Image Analysis and Data Mining for Carbon Assessment in Floodplains. *Proceedings of the 4th GEOBIA*, pages 96–101.

Svetnik, V., Liaw, A., Tong, C., Culberson, J. C., Sheridan, R. P., and Feuston, B. P. (2003). Random forest: a classification and regression tool for compound classification and QSAR modeling. *Journal of chemical information and computer sciences*, 43(6):1947–58.

Temmerman, S., Govers, G., Wartel, S., and Meire, P. (2004). Modelling estuarine variations in tidal marsh sedimentation: response to changing sea level and suspended sediment concentrations. *Marine Geology*, 212(1-4):1–19.

Turner, D., Lucieer, A., Malenovský, Z., King, D., and Robinson, S. (2014). Spatial Co-Registration of Ultra-High Resolution Visible, Multispectral and Thermal Images Acquired with a Micro-UAV over Antarctic Moss Beds. *Remote Sensing*, 6(5):4003–4024.

Turner, D., Lucieer, A., and Watson, C. (2012). An Automated Technique for Generating Georectified Mosaics from Ultra-High Resolution Unmanned Aerial Vehicle (UAV) Imagery, Based on Structure from Motion (SfM) Point Clouds. *Remote Sensing*, 4(12):1392–1410.

Turner, M. G., Dale, V. H., and Gardner, R. H. (1989). Predicting across scales: Theory development and testing. *Landscape Ecology*, 3(3-4):245–252.

Tuttle, E. and Jensen, R. (2006). Using remote sensing image texture to study habitat use patterns: a case study using the polymorphic white-throated sparrow (Zonotrichia albicollis). *Global Ecology and Biogeography*, 15(4):349–357.

Viña, A., Gitelson, A. A., Nguy-Robertson, A. L., and Peng, Y. (2011). Comparison of different vegetation indices for the remote assessment of green leaf area index of crops. *Remote Sensing of Environment*, 115(12):3468–3478.

Vosselman, G. and Gorte, B. (2004). Recognising structure in laser scanner point clouds. *International archives of photogrammetry, remote sensing and spatial information sciences*, 46(8):33–38.

Wallace, L., Lucieer, A., Watson, C., and Turner, D. (2012). Development of a UAV-LiDAR System with Application to Forest Inventory. *Remote Sensing*, 4(12):1519–1543.

Walter, M., Niethammer, U., Rothmund, S., and Joswig, M. (2009). Joint analysis of the Super-Sauze (French Alps) mudslide by nanoseismic monitoring and UAV-based remote sensing. *First Break*, 27(August):53–60.

Wang, A., Qiu, T., and Shao, L. (2009). A Simple Method of Radial Distortion Correction with Centre ofDistortion Estimation. *Journal of Mathematical Imaging and Vision*, 35(3):165–172.

Wang, J., Shi, F., Zhang, J., and Liu, Y. (2006). A New Calibration Model and Method of Camera Lens Distortion. *2006 IEEE/RSJ International Conference on Intelligent Robots and Systems*, pages 5713–5718.

Westoby, M., Brasington, J., Glasser, N., Hambrey, M., and Reynolds, J. (2012). Structure-from-Motion photogrammetry: A low-cost, effective tool for geoscience applications. *Geomorphology*, 179:300–314.

Whiteside, T., Bartolo, R., and Staben, G. (2012a). A rule-based approach to segment and classify floodplain vegetation from WorldView-2 imagery. *Proceedings of the 16th Australasian Remote Sensing and Photogrammetry Conference*.

Whiteside, T., Maier, S., and Boggs, G. (2012b). Site-specific Area-based Validation of Classified Objects. *Proceedings of the 4th GEOBIA*, pages 153–157.

Woodcock, C. E. and Strahler, A. H. (1987). The factor of scale in remote sensing. *Remote Sensing of Environment*, 21(3):311–332.

Wu, J. and Qi, Y. (2000). Dealing with Scale in Landscape Analysis: An Overview. *Annals of GIS*, 6(1):1–5.

Wu, J., Shen, W., Sun, W., and Tueller, P. (2002). Empirical patterns of the effects of changing scale on landscape metrics. *Landscape Ecology*, 17(8):761–782.

Wu, X., Wang, K., and Zhang, D. (2005). Wavelet energy feature extraction and matching for palmprint recognition. *Journal of Computer Science and ...*, 20(3):411–418.

Wulder, M. (1998). Optical remote-sensing techniques for the assessment of forest inventory and biophysical parameters. *Progress in Physical Geography*, 22(4):449–476.

Xiang, H. and Tian, L. (2011). Development of a low-cost agricultural remote sensingsystem based on an autonomous unmanned aerial vehicle (UAV). *Biosystems Engineering*, 108(2):174–190.

Yu, W. (2004). Practical anti-vignetting methods for digital cameras. *IEEE Transactions on Consumer Electronics*, 50(4):975–983.

Yuan, F. and Bauer, M. (2006). Mapping impervious surface area using high resolution imagery: A comparison of object-based and per pixel classification. *Proceedings of ASPRS 2006 annual conference*, pages 1–5.

Zhang, C. and Kovacs, J. M. (2012). The application of small unmanned aerial systems for precision agriculture: a review. *Precision Agriculture*, 13(6):693–712.

Zhang, M. and Ustin, S. (1997). Monitoring Pacific coast salt marshes using remote sensing. *Ecological Applications*, 7(3):1039–1053.

Zhao, G. and Pietikainen, M. (2007). Dynamic texture recognition using local binary patterns with an application to facial expressions. *IEEE Transactions on Pattern Analysis and Machine Intelligence*, 29(6):915–928.

Zhao, X., Liu, J., and Tan, M. (2006). A remote aerial robot for topographic survey. *IEEE/RSJ International Conference on Intelligent Robots and Systems*, pages 3143–3148.

Zheng, Y., Lin, S., Kambhamettu, C., Yu, J., and Kang, S. B. (2009). Single-image vignetting correction. *IEEE transactions on pattern analysis and machine intelligence*, 31(12):2243–56.

Zhou, G. and Ambrosia, V. (2009). Foreword to the special issue on Unmanned Airborne Vehicle (UAV) Sensing systems for earth observations. *IEEE Transactions on Geoscience and Remote Sensing*, 47(3):687–689.

Zhu, S.-C., Shi, K., and Si, Z. (2010). Learning explicit and implicit visual manifolds by information projection. *Pattern Recognition Letters*, 31(8):667–685.